INFORMATION TO USERS

This manuscript has been reproduced from the microfilm master. UMI films the text directly from the original or copy submitted. Thus, some thesis and dissertation copies are in typewriter face, while others may be from any type of computer printer.

The quality of this reproduction is dependent upon the quality of the copy submitted. Broken or indistinct print, colored or poor quality illustrations and photographs, print bleedthrough, substandard margins, and improper alignment can adversely affect reproduction.

In the unlikely event that the author did not send UMI a complete manuscript and there are missing pages, these will be noted. Also, if unauthorized copyright material had to be removed, a note will indicate the deletion.

Oversize materials (e.g., maps, drawings, charts) are reproduced by sectioning the original, beginning at the upper left-hand corner and continuing from left to right in equal sections with small overlaps.

Photographs included in the original manuscript have been reproduced xerographically in this copy. Higher quality 6" x 9" black and white photographic prints are available for any photographs or illustrations appearing in this copy for an additional charge. Contact UMI directly to order.

ProQuest Information and Learning
300 North Zeeb Road, Ann Arbor, MI 48106-1346 USA
800-521-0600

Optical Image Reconstruction in Highly Scattering Media

by

Min Xu

A dissertation submitted to the Graduate Faculty in Physics in partial fulfillment of the requirements for the degree of Doctor of Philosophy

The City University of New York

2001

UMI Number: 3024845

Bell & Howell Information and Learning Company
300 North Zeeb Road
P.O. Box 1346
Ann Arbor, MI 48106-1346

This manuscript has been read and accepted for the Graduate Faculty in Physics in satisfaction of the dissertation requirement for the degree of Doctor of Philosophy.

9/20/2001
Date

Melvin Lax
Chair of Examining Committee
Distinguished Professor Melvin Lax

9/20/2001
Date

Executive Officer
Professor Louis S. Celenza

Distinguished Professor Melvin Lax

Distinguished Professor Robert R. Alfano

Distinguished Professor Joseph L. Birman

Dr. Swapan K. Gayen

Distinguished Professor Theodore Raphan

Supervisory Committee

The City University of New York

Abstract

Optical Image Reconstruction in Highly Scattering Media

by

Min Xu

Advisor: Professor Melvin Lax

Light propagation in turbid media is treated by the theory of radiative transfer. We show that the cumulant approximation to radiative transfer is a major improvement over the diffusion approximation and it describes correctly both the ballistic photons at early times and diffusive photons at later times. Comparisons between the second order cumulant approximation, the diffusion approximation and Monte Carlo simulations are presented. A transport forward model for optical imaging based on the second order cumulant approximation is then proposed. The weight function for image reconstruction under this new model is shown to address the deficiency of the diffusion approximation and reveals the effect of the initial ballistic motion of incident photons.

The framework for image reconstruction for weak inhomogeneities using the Born approximation and the Green's function method is presented, following a brief review of the inverse problem and regularization methods. We present several three-dimensional near real time image reconstruction algorithms which exploit the inherent

symmetry of planar geometries and transform the image reconstruction problem into reconstructions of decoupled spatial Fourier components of the optical property in the Fourier space. In particular, based on the theory of propagation of a spatial Fourier component of the scattered wave field inside a turbid medium, a new optical diffuse imaging methodology is presented which uses the two-dimensional Fourier transform of photon intensity on a plane to detect inhomogeneities in a highly scattering turbid medium when illuminated by a picosecond (near) plane wave pulse.

Finally, we provide a summary and end with a discussion about future directions of the optical tomographic imaging research.

Dedication

To My Loving Father, Mother and Wife!

Acknowledgements

Let me first present my most grateful thanks to my honorable mentor and great friend Professor Melvin Lax whose insightful intuition, critical thoughts and warm encouragement have inspired me and guided me throughout the years of graduation study. Mel's extensive knowledge, masterful understanding and unique insights of Random Process, Photonics and Scientific Computation have always been a great enjoyment and an inspiring source to work with and learn from.

I would like specially to thank Prof. Robert. R. Alfano whose numerous encouragements and challenges have motivated me throughout the years of graduation study.

I would like specially to thank Dr. Wei Cai. Our countless discussions and ardent arguments have always been an enjoyment for me.

I would like specially to thank Dr. Swapan K. Gayen who provides precious help and unique opinions as an experimental physicist.

I would like to thank Mohammad Alrubaiee and Dr. Manuel E. Zevallos for their help and great collaborations during the work of my thesis, who often work overtime to perform the experiments.

I would like to thank Dr. Alvin Katz and Dr. Bidyut Das for their kind help during my graduate years.

I would like to thank Prof. Herman Z. Cummins, Prof. Joseph L. Birman and Prof. Harold Falk for their kind help during my graduate years.

Finally I would like to thank Prof. Robert R. Alfano, Prof. Joseph L. Birman, Dr. Swapan K. Gayen and Prof. Theodore Raphan for serving in the Supervisory Committee.

Last but not the least, I would like to thank all the professors, colleagues and

students who have helped me during my graduate years.

Contents

List of Tables

List of Figures

Chapter 1

Introduction

Image reconstruction in a highly scattering medium is an attempt to extract information about a three-dimensional map of absorption and scattering properties of the turbid medium from a set of measurements of transmitted light received by detectors surrounding the medium. One of its most important applications can be found in biomedical imaging and diagnostics. Optical biomedical tomography, especially optical mammography, provides a safe, non-invasive and affordable imaging tool which has the potential to compete with other screening methodologies such as x-ray mammography, ultrasound and magnetic resonance imaging. Furthermore, its unique capability to characterize the absorption and scattering properties of the lesion at one or more wavelengths may be used to detect and distinguish between normal and malignant tissue.

The last decade has seen active research and development in optical tomography and mammography in both the time- and frequency-domains [1–9]. Back-propagation [10–12], projection imaging [13–15], model-fitting [16, 17], random-walk [18, 19], iterative tomographic image reconstruction [20–23] and perturbative tomographic imag-

ing [24–27] were developed by different groups. Since photons are highly scattered in migration through tissue, conventional tomographic methods perform poorly in optical tomography. Even now this area is still a challenging one.

1.1 Review of current research

Optical mammography is being developed as a non-invasive imaging modality that employs visible and near-infrared (NIR) light (typically in the wavelength range 700 – 1300nm) to detect breast cancer.

The basic interaction mechanism of NIR light with biological tissue is much different from the mechanism by which X rays interact with such tissue. X rays interact with tissue more at the atomic core levels and image primarily the atomic weight differences between different regions [28, 29]. NIR photons, on the other hand, interact and image the electronic level, molecular bonding, and microstructural differences by means of absorption, refraction, or scattering. This can lead to the differentiation of phenomena such as vascularization in a cancer core as well as the molecular differences in the same region, which in turn lead to the detection and assessment of cancer in a non-invasive way that can also be applied to rapid *in vivo* examinations.

Thus optical mammography possesses unique advantages over other screening methodologies such as x-ray mammography, ultrasound and magnetic resonance imaging. Both scattering and absorption properties of tumors and the surrounding tissue (any concentrations of metabolic compounds such as hemoglobin, water, lipids cytochromes, or exogenously administrated contrast agents) are accessible and may be used to detect and characterize lesions [30]. Furthermore optical properties determined at several wavelengths may track *in vivo* tissue functions such as hemoglobin

and cytochrome oxygen saturation [31] or tissue oxygen partial pressure [32].

Optical mammography was first proposed in 1929 [33], and it evolved in the so-called diaphanography [34] and light scanning [35] in the 1970s and early 1980s. The basic approach consisted of illuminating one side of the female breast with a continuous-wave light beam, while the examiner looked for the regions of lower transmitted intensity (shadows) on the opposite side. The method evolved empirically and was eventually abandoned in the early 1990s due to its inferior performance with respect to x-ray mammography [36]. The shadow of the tumor is obscured because the photons are highly scattered and travel through all parts of the breast.

Recent progress in the understanding of light propagation in breast tissue and the development of techniques in either the time- or frequency-domain in tissue spectroscopy have yielded new approaches in optical mammography [5–7]. The recent reviews by Hebden and Arridge [8,9] summarize developments in experimental techniques, modeling and reconstruction. Alfano et. al. pioneered in the research of time resolved imaging using an ultrafast laser system [1,37,38]. Alfano et. al. [2,3] also review the advances in optical imaging of biomedical media, especially for time-resolved and nonlinear optical techniques.

Among all the lines of development in optical imaging in the time- or frequency-domain, several promising techniques have emerged. In the following paragraphs, we will try to classify them according to the fundamental assumption or simplification made in different techniques.

Several groups have applied techniques from diffraction tomography [39–41] to optical mammography. Colak et. al. [10] modified the standard back-propagation approach to include the effects of diffusion of the light through the deconvolution of

the broadened image by a spatially varying point-spread function. A similar method was also used by Walker [11]. Matson [12, 42] used the back-propagation concept to probe the turbid media with the use of measurement on a single plane. The underlying concept of the back-propagation method is to regard the photon migration in turbid media as a propagation of the wavefield which relates to the inhomogeneity through a pair of transformations of Radon and inverse-Radon type [43]. The high-scattering of the photon is taken into account by deconvolution with the point-spread function [10]. Filtering is necessary to stabilize the process of back-propagation. Another diffraction tomography type method was proposed by Li et. al. [13] who obtained projection images experimentally by deconvolution of the scattered diffuse-photon density waves on a planar boundary with use of a fast Fourier transform. This method needs extra depth information of inhomogeneities inside turbid media to behave well and has other limitations [14, 15].

Model-fitting is another common choice. The tumor is assumed to take a shape (sphere or cylinder) embedded in a uniform medium for which an analytical solution to the diffusion equation is available [44, 45]. The nonlinear dependence of the photon intensity on the optical properties is automatically included. The assumption of homogeneity of the healthy tissue might be too strong. Fantini et. al. [16] and Grosenick et al. [17] used model-fitting in the frequency- and time-domain respectively.

A tomographic optical imaging procedure based on the finite-element-method solution to the diffusion equation was used by Arridge et. al. [20, 21]. Jiang et. al. [22] and others [23]. The estimated optical properties distribution is iteratively updated by a Newton-type or a conjugate gradient-type technique through inverting a so-called Hessian matrix which represents the influence on the measured photon intensity at

each detector site from each voxel inside the medium. This method models both the nonlinear dependence of the photon intensity on the optical properties and the inhomogeneous nature of the tissue and is the most powerful approach for optical mammography. However, this method becomes time-prohibitive when the number of voxels increases. Usually a 3D reconstruction is formed by a series of 2D cross sections which is imaged by placing the source and the detector on one plane at a time to reduce the computing time [46].

The tomographic image reconstruction can be sped up tremendously if the inhomogeneity can be assumed to be weak in the sense of the Born or Rytov approximation [47]. The Green's function method can then be used to solve the diffusion equation analytically in a planar geometry and yields a linearized relation between the measurement and the inhomogeneity. Such a perturbative tomographic imaging method was used by various groups [24–27]. A near real-time reconstruction can be achieved by using a Fourier type technique and exploiting the symmetry existing in the inverse problem [26, 27].

1.2 Motivation

A short pulse of light transmitted through a highly scattering medium can be broken up into *ballistic*, *snake* and *diffusive* components [Figure (1.1)] [1, 37]. Ballistic photons scatter coherently, and snake photons scatter only slightly from the forward direction. Both arrive much sooner than multiply-scattered diffusive photons. The ballistic or snake photons are used in shadowgrams [1, 48] to image thin tissue. For soft tissue with a thickness of several centimeters, adequate intensities are usually only available from diffusive photons. The optical properties of turbid media is then

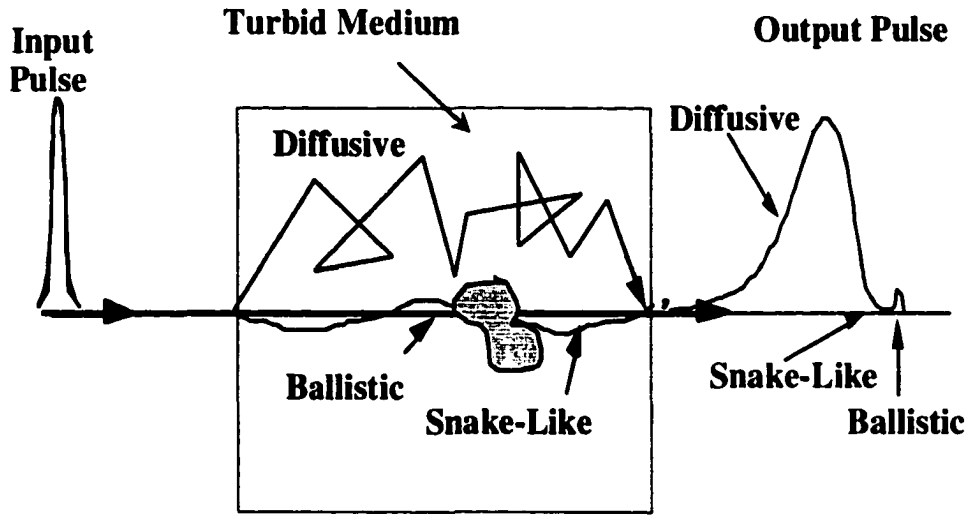

Figure 1.1: The transmitted light from a very short pulse through a highly scattering medium is broken-up into ballistic, snake and diffusive components.

reconstructed from the detected surrounding transmitted diffusive photon intensity by assuming the diffusion approximation.

Optical mammography based on the diffusion approximation is restricted to use only diffusive photons, and fails to predict correctly the contribution to light intensity from an inhomogeneity near the source or the detector [38]. This problem is much more accentuated in the backscattering case.

Our first objective is to develop a more accurate photon transport model than the diffusion approximation. The new model will be based on an approximate analytic solution to the Boltzmann radiative transfer equation and is able to describe the photon migration from the initial ballistic motion through the diffusive regime in an analytical way for the first time [49, 50]. Under the new photon transport model,

- both diffusive photons and photons traveling comparatively short trajectories (limited by the signal-to-noise ratio) can be used in reconstructing an image.

- the model error in the contribution to light intensity from inhomogeneity at regions near the source or detector, introduced by the diffusion approximation, will be overcome.

Strong light scattering is the main factor which limits the spatial resolution obtainable through optical mammography. The use of a transport model rather than the diffusion approximation in tomographic imaging will improve the contrast and resolution of optical mammography because of both a more accurate forward model and the inclusion of early light which experiences much less scattering.

Our second objective is to develop near real time three-dimensional tomographic imaging strategies by exploiting geometrical symmetry and using Fourier techniques to simplify the inverse problem. The time-resolved image reconstruction formalism, based either on the diffusion approximation or the new transport model for photon migration in a turbid medium, yields a matrix equation

$$\mathbf{y}(\lambda) = W(\lambda)\mathbf{x}(\lambda) \tag{1.1}$$

for a near infrared source with a wavelength of λ. Here $\mathbf{y}$ is an array containing the change in measured transmitted photon intensity. $\mathbf{x}$ is an array of the deviation of optical parameters (absorption and/or scattering coefficient), due to existence of a local inhomogeneity, which, in practical application, is the difference of the optical parameters between a patient's tissue and the assumed reference medium. W is the weight function, which, in the linear inversion case, is related only to the reference medium. For our tomographic reconstruction problem, the weight function W has a huge dimension and the matrix equation Eq. (1.1) is ill-posed. A direct inversion

is thus prohibitive. We address these difficulties by first transforming Eq. (1.1) into simpler equations of a smaller dimension in an appropriate Fourier space and second stabilizing the reconstruction process using a Tikhonov regularization inversion scheme.

1.3 Thesis statement

This thesis will focus on the study of light propagation in highly scattering turbid media, towards a more accurate description of photon migration in such media, especially a new transport forward model for image reconstruction.

This thesis will also focus on the inverse image reconstruction in highly scattering turbid media, towards near real time three-dimensional tomographic image reconstruction methods applicable in biomedical imaging, especially breast cancer screening in the long run.

This thesis is naturally divided into two parts–the forward and inverse problems of tomographic image reconstruction. My main contributions are the new transport forward model and three-dimensional tomographic image reconstruction methods discussed in chapters 4, 6 and 7.

The first part, chapters 2 through 4, will study light propagation in turbid media and try to establish a transport forward model for subsequent image reconstruction in turbid media.

Chapter 2 discusses the widely used diffusion approximation to radiative transfer and highlights its limitations.

Chapter 3 discusses Monte Carlo simulations of photon migration in turbid media. The Monte Carlo simulation will serve as a comparison standard in Chapter 4 to

monitor the performance of different approximations to radiative transfer. The advantage of the Monte Carlo method is that it avoids assumptions needed in analytical procedures to obtain answers.

Chapter 4, the major chapter in part 1, presents my research on a new transport forward model of photon migration in turbid media based on the second order cumulant approximation of Cai et. al. [51] The cumulant approximation is first introduced. The transport forward model is then derived with use of the first order Born approximation to the Boltzmann equation to handle the deviation in absorption or scattering coefficients from uniformity and an approximate form of photon intensity based on the second order cumulant photon density solution to radiative transfer. Comparisons with Monte Carlo simulations show this new model is a major improvement over the diffusion approximation. Furthermore, this model provides a more accurate weight function when any separation between the source, the inhomogeneity and the detector is small and reveals the effect of the initial ballistic motion of incident photons on the weight function.

The second part, chapters 5 through 7, will study three-dimensional tomographic image reconstruction algorithms using time-resolved measurements.

Chapter 5 gives a general introduction to the inverse problem which has no unique solution. The Tikhonov regularization by Tikhonov [52] and the L-curve method by Hansen [53] are introduced to stabilize the otherwise ill-posed inversion process. This chapter serves as a mathematical foundation for image reconstruction.

Chapter 6 summarizes the strategies we developed to decompose the three dimensional image reconstruction problem into reconstructions of decoupled spatial Fourier components of the optical property in the Fourier space by exploiting the inherent

symmetry of planar geometries.

Chapter 7 presents the time-resolved Fourier optical diffuse tomography by me, a novel approach for imaging of objects in a highly scattering turbid medium using an incident (near) plane wave. The theory of the propagation of spatial Fourier components of the scattered wave field is presented, with a fast algorithm for three-dimensional reconstruction in a parallel planar geometry. Examples of successful reconstructions of simulated hidden absorptive or scattering objects embedded inside a human-tissue-like semi-infinite turbid medium are provided at the end of the chapter.

The last chapter, chapter 8, gives a summary and outlines the future research direction of the tomographic image reconstruction.

Chapter 2

Photon Migration in Turbid Media Using the Diffusion Approximation

2.1 Introduction

The problem of light scattering is an old and rich theory [54, 55]. After Maxwell established the electromagnetic theory of light in the late nineteenth century, the problem of elastic, independent, and single scattering [55] by an object was extensively studied, the full solution for a homogeneous, isotropic sphere was formulated by Mie in 1908 [56].

Photon transport in a highly scattering medium when there is no simultaneous scattering (the scatterers are far apart), can be described by the linear Boltzmann equation [57–59]. The Boltzmann equation for the photon distribution function $I(\mathbf{r}, \mathbf{s}, t)$ at position $\mathbf{r}$, direction $\mathbf{s}$ and time t from a unit source at position $\mathbf{r}_0$

propagating along $\mathbf{s}_0$ at time $t_0 = 0$, is given by

$$\begin{aligned} & \frac{\partial}{\partial t} I(\mathbf{r}, \mathbf{s}, t) + c\mathbf{s} \cdot \nabla_{\mathbf{r}} I(\mathbf{r}, \mathbf{s}, t) + c[\mu_s(\mathbf{r}) + \mu_a(\mathbf{r})] I(\mathbf{r}, \mathbf{s}, t) \\ = \; & c\mu_s(\mathbf{r}) \int d\mathbf{s}' P(\mathbf{s}, \mathbf{s}', \mathbf{r}) I(\mathbf{r}, \mathbf{s}', t) d\mathbf{s}' + \delta(\mathbf{r} - \mathbf{r}_0)\delta(\mathbf{s} - \mathbf{s}_0)\delta(t) \end{aligned} \tag{2.1}$$

where c is light speed inside the medium, μ_a and μ_s denote the position-dependent absorption and scattering coefficients, and $P(\mathbf{s}, \mathbf{s}', \mathbf{r})$ is the normalized phase function of the light propagation in the medium.

We will assume that the phase function $P(\mathbf{s}, \mathbf{s}', \mathbf{r})$ is only a function of the cosine of the scattering angle $\mathbf{s} \cdot \mathbf{s}'$ and of position $\mathbf{r}$, and adopt the common terminology used in optical tomography: absorption length $l_a = \mu_a^{-1}$, scattering mean free path $l_s = \mu_s^{-1}$, anisotropy factor $g = \int d\Omega \cos\theta P(\cos\theta, \mathbf{r})$ where $d\Omega = d\cos\theta d\varphi$, reduced-scattering coefficient $\mu_s' = (1 - g)\mu_s$ and transport mean free path $l_t = (\mu_s')^{-1} > l_s$. Typical values in human breast tissue are: $\mu_s \sim 10 - 100mm^{-1}$, $\mu_s' \sim 1mm^{-1}$ and $\mu_a \sim 1/300mm^{-1}$.

The Boltzmann equation Eq. (2.1) is a non-separable equation of the first order and only has analytical solutions in restricted cases [60,61]. Different approximations have been developed for the solution of this equation. Among all these approximations, the diffusion approximation is the one employed extensively in optical tomography. Other approximations include the small angle approximation [62–64] for a highly forward-scattering medium, and the cumulant approximation [50, 51].

2.2 Diffusion approximation

To illustrate how to obtain the diffusion equation from the Boltzmann equation, we first note the solution to the Boltzmann equation Eq. (2.1) in an infinite medium can always be expressed in terms of the solution to Eq. (2.1) in which $\mu_a = 0$, say I_0, by [57]

$$I(\mathbf{r}, \mathbf{s}, t) = \exp\left[-\mu_a(\mathbf{r})ct\right] I_0(\mathbf{r}, \mathbf{s}, t). \tag{2.2}$$

The fundamental consequence of this equality is that the "proper" diffusion coefficient does not depend on absorption, contrary to some claims made in the literature [65,66]. We will see this independence a bit later and a more thorough answer is provided in Chap. 4.

Let's introduce photon density ϕ, photon flux $\mathbf{J}$, and the second moment $\mathcal{T}$ of the photon distribution in the direction space

$$\begin{aligned} \phi(\mathbf{r}, t) &= \int d\mathbf{s} I_0(\mathbf{r}, \mathbf{s}, t) \\ \mathbf{J}(\mathbf{r}, t) &= \int d\mathbf{s}\, \mathbf{s} I_0(\mathbf{r}, \mathbf{s}, t) \\ \mathcal{T}(\mathbf{r}, t) &= \int d\mathbf{s}\, \mathbf{s}\mathbf{s} I_0(\mathbf{r}, \mathbf{s}, t), \end{aligned} \tag{2.3}$$

then the integrations over direction $\mathbf{s}$ of the non-dissipative version of Eq. (2.1) in which $\mu_a = 0$ and the product of $\mathbf{s}$ and the non-dissipative version of Eq. (2.1) yield,

$$\begin{aligned} \frac{\partial}{\partial t}\phi(\mathbf{r}, t) + c\nabla_{\mathbf{r}} \cdot \mathbf{J}(\mathbf{r}, t) &= 0 \\ \frac{\partial}{\partial t}\mathbf{J}(\mathbf{r}, t) + c\nabla_{\mathbf{r}} \cdot \mathcal{T}(\mathbf{r}, t) + c(1-g)\mu_s(\mathbf{r})\mathbf{J}(\mathbf{r}, t) &= 0 \end{aligned} \tag{2.4}$$

where $g = \int ds\, \mathbf{s} \cdot \mathbf{s}_0 P(\mathbf{s} \cdot \mathbf{s}_0, \mathbf{r}) = \int d\Omega \cos\theta P(\cos\theta, \mathbf{r})$.

The essential step of the diffusion approximation is to assume that

$$\begin{aligned} &\text{(i)} \quad \mathcal{T} \simeq 3^{-1}\phi(\mathbf{r},t)\mathcal{I} \\ &\text{(ii)} \quad \left|\frac{\partial}{\partial t}\mathbf{J}(\mathbf{r},t)\right| \ll |c(1-g)\mu_s(\mathbf{r})\mathbf{J}(\mathbf{r},t)| \end{aligned} \tag{2.5}$$

where $\mathcal{I}$ is the unit 3×3 tensor.

Under the conditions specified by Eq. (2.5), Eq. (2.4) yields the non-dissipative diffusion equation:

$$\begin{aligned} \mathbf{J}(\mathbf{r},t) = -\frac{1}{3(1-g)\mu_s}\nabla_{\mathbf{r}}\phi(\mathbf{r},t) &= -D(\mathbf{r})\nabla_{\mathbf{r}}\phi(\mathbf{r},t) \\ \frac{\partial}{\partial t}\phi(\mathbf{r},t) - c\nabla_{\mathbf{r}} \cdot D(\mathbf{r})\nabla_{\mathbf{r}}\phi(\mathbf{r},t) &= 0 \end{aligned} \tag{2.6}$$

where the diffusion coefficient $D(\mathbf{r}) = \frac{1}{3(1-g)\mu_s} = \frac{1}{3}(\mu_s')^{-1} = \frac{1}{3}l_t$. The dissipative version of the diffusion equation

$$\frac{\partial}{\partial t}\phi(\mathbf{r},t) + c\mu_a\phi(\mathbf{r},t) - c\nabla_{\mathbf{r}} \cdot D(\mathbf{r})\nabla_{\mathbf{r}}\phi(\mathbf{r},t) = 0 \tag{2.7}$$

carries the same diffusion coefficient, $D(\mathbf{r})$, independent of absorption.

The first condition in Eq. (2.5) means the scattering of photons can be regarded as uniform in all directions due to the randomized photon propagation direction prior to scattering. Take a typical case of a point pulse at the origin and time zero in an infinite homogeneous medium, the solution to the non-dissipative diffusion equation is

$$\phi(\mathbf{r},t) = \frac{1}{(4\pi Dct)^{3/2}} \exp\left(-\frac{r^2}{4Dct}\right) \tag{2.8}$$

with $\mathbf{J}(\mathbf{r},t) = -\mathbf{r}\phi(\mathbf{r},t)/(2Dct)$. The second condition is equivalent to

$$\left|\frac{3}{4}\left(\frac{r}{ct}\right)^2 - \frac{5}{2}\frac{l_t}{ct}\right| \ll 1, \tag{2.9}$$

which means a later time requirement, i.e., much later than the ballistic time ($ct \gg r, l_t$). The diffusion approximation is hence an asymptotic behavior of photon migration after a sufficient large number of scattering have taken place such that the photon distribution is almost isotropic (uniformly scattering in all directions) and at a later time in the sense of Eq. (2.9).

The diffusion approximation belongs to a family of approximations based on the spherical harmonics expansion of the photon intensity and it corresponds to the truncation in the spherical harmonics expansion at the second order. This approximation is good for scattering-dominated propagation, but will perform poorly in the ballistic regime. The full family of approximations based on the spherical harmonics expansion is insufficient in describing transport in the case of a strongly peaked phase function [67].

2.3 Green's function

The diffusion equation in a turbid medium:

$$\frac{\partial}{\partial t}\phi(\mathbf{r},t) + c\mu_a\phi(\mathbf{r},t) - c\nabla_{\mathbf{r}}\cdot D(\mathbf{r})\nabla_{\mathbf{r}}\phi(\mathbf{r},t) = S(\mathbf{r},t) \tag{2.10}$$

is readily solved by the Green's function method when there are only small perturbations of the uniform background whose absorption coefficient is μ_a and diffusion

coefficient is D. The Green's function $G(\mathbf{r}, t)$ of Eq. (2.10) in a uniform medium is defined as the solution of:

$$(Dc\nabla^2 - \frac{\partial}{\partial t} - \mu_a c)G(\mathbf{r}, \mathbf{r}_0, t) = -\delta(\mathbf{r} - \mathbf{r}_0)\delta(t) \tag{2.11}$$

and has units of inverse length cubic.

The Green's function for a uniform infinite medium with Dirichlet boundary condition at infinity is given by

$$G(\mathbf{r}, \mathbf{r}_0, t) = \frac{1}{(4\pi Dct)^{3/2}} \exp(-\frac{(\mathbf{r} - \mathbf{r}_0)^2}{4Dct} - \mu_a ct)\, \mathrm{H}(t) \tag{2.12}$$

where $\mathrm{H}(t)$ is the Heaviside step function.

$$\mathrm{H}(t) = \begin{cases} 1 & t \geq 0 \\ 0 & t < 0 \end{cases} \tag{2.13}$$

In a planar geometry, $G(\mathbf{r}, \mathbf{r}_0, t)$ is naturally separated into an xy (2D) component and a z component. For the Green's function of the infinite uniform medium, we have the separation of the form

$$G_{2D}(x, y, x_0, y_0, t) = \frac{1}{4\pi Dct} \exp(-\frac{(x - x_0)^2 + (y - y_0)^2}{4Dct}) \tag{2.14}$$

$$G_z(z, z_0, t) = \frac{1}{\sqrt{4\pi Dct}} \exp(-\frac{(z - z_0)^2}{4Dct}) \tag{2.15}$$

$$G(\mathbf{r}, \mathbf{r}_0, t) = G_{2D}(x, y, x_0, y_0, t)G_z(z, z_0, t) \exp(-\mu_a ct)\, \mathrm{H}(t) \tag{2.16}$$

Two other important examples of planar geometry are a semi-infinite space and a slab with homogeneous Dirichlet boundary conditions. The only modification of the

solution is made to the z-component Eq. (2.15). It is modified to:

$$G_{z,\text{slab}}(z, z_0, t) = \frac{1}{\sqrt{4\pi Dct}} \sum_{n=-\infty}^{+\infty} (-1)^n \exp(-\frac{(z - z_n)^2}{4Dct}) \tag{2.17}$$

where z_n are the virtual images of z_0 due to the slab geometry [21]

$$z_n = \begin{cases} nd + z & \text{for } n \text{ even} \\ (n+1)d - z & \text{for } n \text{ odd} \end{cases} \tag{2.18}$$

for the slab geometry with boundaries at 0 and d, and

$$G_{z,\text{semi}}(z, z_0, t) = \frac{1}{\sqrt{4\pi Dct}}(\exp(-\frac{(z - z_0)^2}{4Dct}) - \exp(-\frac{(z + z_0)^2}{4Dct})) \tag{2.19}$$

for a semi-infinite space with its interface at $z = 0$, respectively. The latter is chosen to vanish at $z = 0$ and the former is chosen to vanish at $z = 0$ and $z = d$.

Another commonly encountered quantity is the Green's function associated with source S [See Appendix (B)], i.e., the incident wave field for a uniform background from a photon source $S(\mathbf{r}, t)$,

$$G^{\text{S}}(\mathbf{r}, t) = \int d^3\mathbf{r}_0 dt_0 S(\mathbf{r}_0, t_0) G(\mathbf{r}, \mathbf{r}_0, t - t_0). \tag{2.20}$$

For a symmetrical plane source centered at $(x = 0, y = 0)$ on plane $z = z_0$, $S(\mathbf{r}, t) = f(\rho)\delta(z - z_0)\delta(t)$, it is easy to verify that G^{S} can also be separated into 2D and z-components,

$$G^{\text{S}}(\rho, z, z_0, t) = G^{S}_{2D}(\rho, t) G_z(z, z_0, t) \exp(-\mu_a ct)\, \text{H}(t) \tag{2.21}$$

with its 2D component:

$$G_{2D}^{S}(\rho,t)=\frac{1}{2Dct}\int \rho_s f(\rho_s)\exp(-\frac{\rho^2+\rho_s^2}{4Dct})\mathrm{I}_0(\frac{\rho\rho_s}{2Dct})d\rho_s. \tag{2.22}$$

2.4 Born approximation

Using the Green's function, the solution for the diffusion equation Eq. (2.10) for a uniform infinite medium can be expressed as:

$$\phi(\mathbf{r},t)=\int d^3\mathbf{r}_0 dt_0 S(\mathbf{r}_0,t_0)G(\mathbf{r},\mathbf{r}_0,t-t_0) \tag{2.23}$$

If some weak inhomogeneity (object) is present in the medium, write $D_{\text{obj}} = D+\delta D$, $\mu_{a,\text{obj}} = \mu_a+\delta\mu_a$, and $\phi(\mathbf{r},t) = \phi_i(\mathbf{r},t)+\phi_s(\mathbf{r},t)$, and ϕ_i as the incident beam Eq. (2.23), then under the first order Born approximation:

$$(Dc\nabla^2-\frac{\partial}{\partial t}-\mu_a c)\phi_s(\mathbf{r},t)=(\delta\mu_a c-\nabla\cdot\delta Dc\nabla)\phi_i(\mathbf{r},t) \tag{2.24}$$

Its solution with the Dirichlet boundary condition becomes:

$$\phi_s(\mathbf{r},t)=\int d^3\mathbf{r}'dt' G(\mathbf{r},\mathbf{r}',t-t')(-\delta\mu_a(\mathbf{r}')c+\nabla\cdot\delta D(\mathbf{r}')c\nabla)\phi_i(\mathbf{r}',t') \tag{2.25}$$

from Eq. (2.23). After partial integration, we have:

$$\begin{aligned}\phi_s(\mathbf{r},t) &= -\int d^3\mathbf{r}'dt' G(\mathbf{r},\mathbf{r}',t-t')\delta\mu_a(\mathbf{r}')c\phi_i(\mathbf{r}',t') \\ &- \int d^3\mathbf{r}'dt'\delta D(\mathbf{r}')c\nabla_{\mathbf{r}'}G(\mathbf{r}-\mathbf{r}',t-t')\cdot\nabla_{\mathbf{r}'}\phi_i(\mathbf{r}',t')\end{aligned} \tag{2.26}$$

which is the main result of the Born approximation.

Born approximation is only valid for weak inhomogeneities. To account for strong inhomogeneities, iterative procedures or model fitting procedures must be employed.

Chapter 3

Monte Carlo Simulation of Light Propagation

3.1 Introduction

Monte Carlo simulations of photon propagation offer a flexible yet rigorous approach toward photon transport in turbid media. The method describes local rules of photon propagation that are expressed, in the simplest case, as probability distributions that describe the step size of photon movement between sites of photon-media interaction, and the angles of deflection in a photon's trajectory when a scattering event occurs. The simulation can score multiple physical quantities simultaneously. However, the method is statistical in nature and relies on calculating the propagation of a large number of photons by the computer. As a result, this method requires a large amount of computation time. The number of photons required in simulation depends largely on the question being asked, the precision needed, and the spatial resolution desired.

3.2 Rules for photon propagation

Photons are traced in the Monte Carlo simulation. Each individual photon will be regarded as a packet which can take a fractional weight to reduce the variance of the Monte Carlo simulation. The initial weight of a photon packet launched is equal to unity ($w = 1$). The position of the photon packet is denoted by (x, y, z) and its direction cosines (μ_x, μ_y, μ_z). The propagation of the photon is simulated by a series of photon movements of random step size s:

$$\begin{aligned} x &\leftarrow x + \mu_x s \\ y &\leftarrow y + \mu_y s \\ z &\leftarrow z + \mu_z s \end{aligned} \tag{3.1}$$

where absorption occurs during each step of movement (weight update) and scattering occurs at the end of each step of movement (direction cosines update). The photon packet is terminated when it is reflected or transmits outside of the medium, or outside of the time frame of interest. The roulette technique [see Sec. (3.2.6)] is used to ensure conservation of energy (number of photons) without skewing the distribution of photon deposition at photon termination.

3.2.1 Choice of step size

The step size of the photon packet is calculated based on a sampling of the probability distribution for photon's free path $s \in [0, \infty)$. Inside a homogeneous medium, the distribution of free path between consecutive scattering or absorption events is

$\mu_T^{-1} \exp(-\mu_T s)$ and can be sampled from:

$$s = \frac{-\ln(\xi)}{\mu_T} \tag{3.2}$$

where ξ is a uniform random number on $(0, 1)$ and $\mu_T = \mu_a + \mu_s$ is the total interaction coefficient. If the medium is inhomogeneous instead, the distribution of free paths obeys:

$$\sum_i \mu_{Ti} s_i = -\ln(\xi) \tag{3.3}$$

Fig. (3.1) shows a schematic diagram for a photon to interact with such an inhomogeneous medium - an otherwise uniform medium (μ_{T1}) embedded with an object (μ_{T2}). To simulate such an event, the relevant part of the algorithm is shown below. A uniform refractive index is assumed.

```
global vector cur_position
global boolean inside
d <- -ln ξ where ξ is a uniform random number over (0.1)
move(d):
    if ( cross_boundary() )
        A <- cur_position
         C <- crossing point
        d' <- d - μ_T(inside) × AC
        inside <- not inside;
        move(d')
    else
        cur_position <- cur_position + d/μ_T(inside)
```

```
return
```

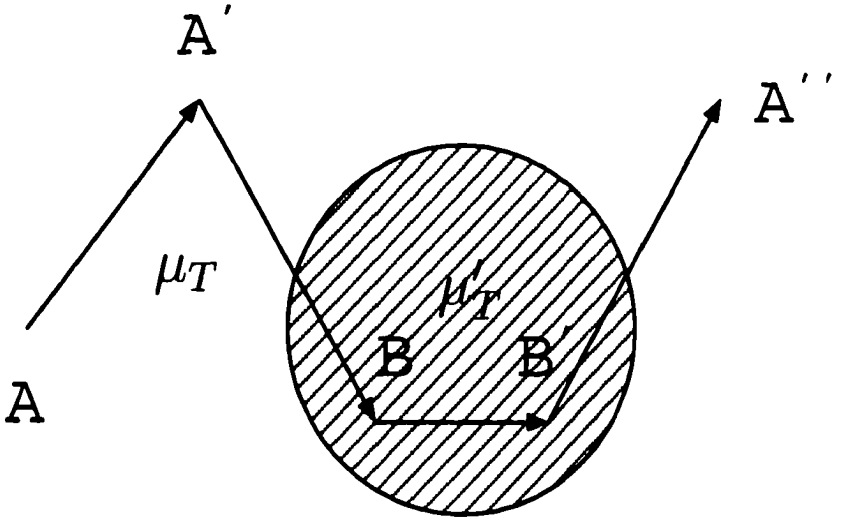

Figure 3.1: A schematic diagram for a photon scattering inside an inhomogeneous medium.

3.2.2 Absorption

Once the photon has taken a step, a fraction of its weight is absorbed, whose value is equal to

$$\Delta w = w\frac{\mu_a}{\mu_t} \tag{3.4}$$

and the weight of the photon packet is updated as:

$$w \leftarrow w - \Delta w = w\frac{\mu_s}{\mu_t} \tag{3.5}$$

3.2.3 Scattering

The scattering event has a simple form in the coordinate system $(\frac{\mathbf{m}-(\mathbf{n}\cdot\mathbf{m})\mathbf{n}}{|\mathbf{n}\times\mathbf{m}|}, \frac{\mathbf{n}\times\mathbf{m}}{|\mathbf{n}\times\mathbf{m}|}, \mathbf{n})$ attached to the moving photon where $\mathbf{n} = (\mu_x, \mu_y, \mu_z)$ is the propagation direction of the photon prior to scattering and $\mathbf{m}$ is an arbitrary unit vector. The deflection angle $\theta \in [0, \pi]$ is distributed according to the phase function $P(\cos\theta)$, and the azimuthal angle ϕ is a uniform random variable over $[0, 2\pi]$. For one specific scattering angle (θ, ϕ), the outgoing direction of the photon will be:

$$\mathbf{n}' = \frac{\mathbf{m}-(\mathbf{n}\cdot\mathbf{m})\mathbf{n}}{|\mathbf{n}\times\mathbf{m}|}\sin\theta\cos\phi + \frac{\mathbf{n}\times\mathbf{m}}{|\mathbf{n}\times\mathbf{m}|}\sin\theta\sin\phi + \mathbf{n}\cos\theta. \tag{3.6}$$

Any choice of the unit vector $\mathbf{m}$ is permissible. Take $\mathbf{m} = (0, 0, 1)$.

$$\begin{aligned}
\mu_x' &= -\frac{\sin\theta}{\sqrt{1-\mu_z^2}}(\mu_x\mu_z\cos\phi - \mu_y\sin\phi) + \mu_x\cos\theta \\
\mu_y' &= -\frac{\sin\theta}{\sqrt{1-\mu_z^2}}(\mu_y\mu_z\cos\phi + \mu_x\sin\phi) + \mu_y\cos\theta \\
\mu_z' &= \sqrt{1-\mu_z^2}\sin\theta\cos\phi + \mu_z\cos\theta
\end{aligned} \tag{3.7}$$

If $|\mu_z|$ is close to 1, then we can choose an alternative $\mathbf{m} = (0, 1, 0)$ and obtain:

$$\begin{aligned}
\mu_x' &= -\frac{\sin\theta}{\sqrt{1-\mu_y^2}}(\mu_x\mu_y\cos\phi + \mu_z\sin\phi) + \mu_x\cos\theta \\
\mu_y' &= \sqrt{1-\mu_y^2}\sin\theta\cos\phi + \mu_y\cos\theta \\
\mu_z' &= -\frac{\sin\theta}{\sqrt{1-\mu_y^2}}(\mu_y\mu_z\cos\phi - \mu_x\sin\phi) + \mu_z\cos\theta.
\end{aligned} \tag{3.8}$$

In the simulation, we will assume the phase function takes the form of the Henyey-

Greenstein phase function: [68]

$$p(\cos\theta) = \frac{1-g^2}{(1+g^2-2g\cos\theta)^{3/2}} \tag{3.9}$$

where $\int_{-1}^{1} d\mu p(\mu) = 2$, and the only variate is the anisotropy of the medium $g = \langle\cos\theta\rangle$. Using the inversion technique [69], the random variable $\cos\theta$ can be generated easily in simulations from:

$$\cos\theta = \frac{1}{2g}\left\{1+g^2-\left[\frac{1-g^2}{1-g+2g\xi}\right]^2\right\} \tag{3.10}$$

where ξ is a uniform random variable on $(0, 1)$. Furthermore, the Henyey-Greenstein phase function has a simple expansion in Legendre polynomials

$$p(\cos\theta) = \sum_{n=0}^{\infty}(2n+1)g^n P_n(\cos\theta). \tag{3.11}$$

The Henyey-Greenstein phase function is widely adopted as an approximate phase function for the atmosphere and tissue due to its nice properties stated above.

3.2.4 Specular reflection

When the photon is launched, if there is a mismatched boundary at the tissue surface, then some specular reflection will occur. If the refractive indices of the outside medium and tissue are n_1 and n_2, respectively, then the specular reflectance, R_{sp}, at normal incidence, is specified as [70]:

$$R_{sp} = \frac{(n_1-n_2)^2}{(n_1+n_2)^2} \tag{3.12}$$

If the first layer is glass, which is on top of a layer of medium whose refractive

index is n_3, multiple reflections and transmissions on the two boundaries of the glass layer are considered. The specular reflectance is then computed by:

$$R_{sp} = r_1 + \frac{(1 - r_1)^2 r_2}{1 - r_1 r_2} \tag{3.13}$$

at normal incidence where r_1 and r_2 are the Fresnel reflectance on the two boundaries of the layer:

$$\begin{aligned} r_1 &= \frac{(n_1 - n_2)^2}{(n_1 + n_2)^2} \\ r_2 &= \frac{(n_2 - n_3)^2}{(n_2 + n_3)^2} \end{aligned} \tag{3.14}$$

3.2.5 Internal reflection

Internal reflection may occur when the photon is propagated across a boundary into a region with a different index of refraction. The probability that the photon will be internally reflected is determined by the Fresnel reflection coefficient [70]

$$R(\theta_i) = \frac{1}{2}\left[\frac{\sin^2(\theta_i - \theta_t)}{\sin^2(\theta_i + \theta_t)} + \frac{\tan^2(\theta_i - \theta_t)}{\tan^2(\theta_i + \theta_t)}\right] \tag{3.15}$$

which is an average of the reflectance for the two orthogonal polarization directions, where $\theta_i = \cos^{-1}\mu_z$ is the angle of incidence on the boundary and the angle of transmission θ_t is given by Snell's law

$$n_i \sin\theta_i = n_t \sin\theta_t \tag{3.16}$$

where n_i and n_t are the refractive indices of the medium from which the photon is incident and transmitted, respectively.

Light will be totally reflected ($R(\theta_i) = 1$) if its incident angle θ_i is larger than the critical angle $\arcsin(n_t/n_i)$ when light transmits from a medium with a higher refractive index to a medium with a lower one, i.e., $n_i > n_t$.

3.2.6 Photon termination

A photon packet is terminated naturally by reflection or transmission out of the medium, or through roulette [69] when its weight falls below a threshold w_{th}. The roulette gives the photon packet one chance in m (e.g., $m = 10$) of surviving with a weight of mw when $w \leq w_{\text{th}}$. If the photon packet does not survive the roulette, the photon weight is reduced to zero and terminated, i.e.,

$$w \leftarrow \begin{cases} mw & \text{if } \xi \leq 1/m \\ 0 & \text{if } \xi > 1/m \end{cases} \tag{3.17}$$

where ξ is a uniform random number on $[0, 1]$. This method conserves energy yet terminates photons in an unbiased manner.

3.3 Results

Monte Carlo calculations can be used to compute physical quantities such as irradiance, flux and photon density. It is a nice tool to justify the common approximations made in photon migration calculations. These results are provided in Chapter. 4 with comparisons to the diffusion and cumulant approximations.

In this section, consider the case of light propagation in a turbid medium with a Henyey-Greenstein phase function and anisotropy $g = 0.9$. Fig. (3.2) shows how many scatterings are required to deflect a forward going photon to move backward (cumulative deflection angle $\theta > \pi/2$). The mean number of scattering required is 18.65, and the maximum of the probability occurs at 8.46 with probability 4.0%. The probability to turn the photon with only one scattering is 2.25%.

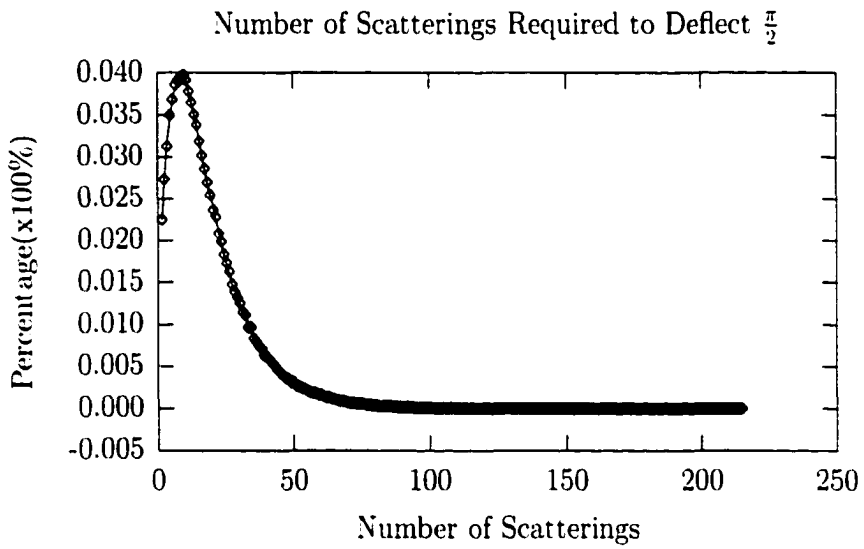

Figure 3.2: Number of scattering required to deflect a forward going photon to move backward (cumulative deflection angle $\theta > \pi/2$) in a uniform medium with a Henyey-Greenstein phase function and anisotropy $g = 0.9$.

The angular distribution of scattered photons vs time in an infinite uniform medium is shown in Fig. (3.3) for the above medium. Fig. (3.4) shows the agreement between Monte Carlo calculations and theoretical predictions ($p = \exp(-\mu_s ct)$) for number of unscattered photons is very good.

The parallel Monte Carlo code to calculate the photon density and photon distribution at any position in a uniform medium (infinite or semi-infinite) is provided

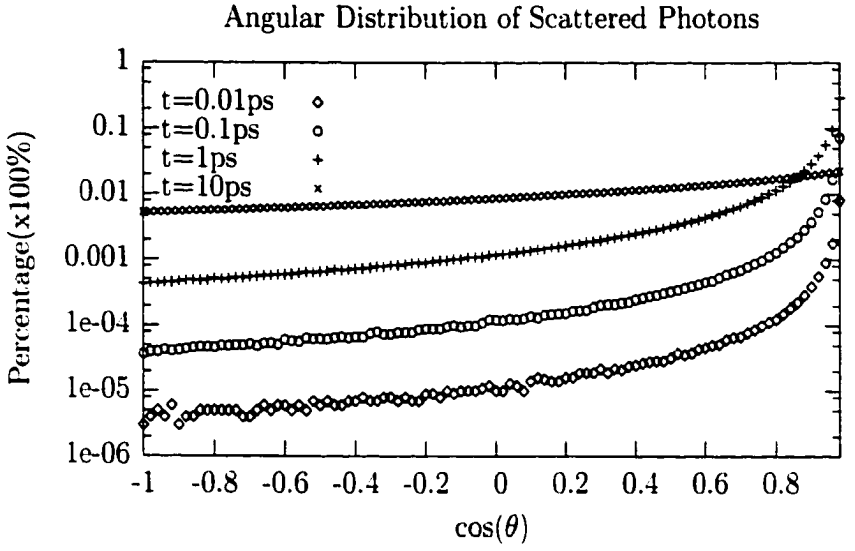

Figure 3.3: Angular distribution of scattered photons vs time in a uniform medium with a Henyey-Greenstein phase function and anisotropy $g = 0.9$.

in Appendix (C). This program uses the Multiplicative Lagged Fibonacci Generator from the Scalable Parallel Random Number Generator libraries (SPRNG) to generate random numbers and Message Passing Interface (MPI) to parallelize the simulation. It supports resuming from previous finished Monte Carlo calculation. A version which handles an heterogeneous medium is also available at request. A correct choice of random number generator is extremely important here. Coddington [71] has done a thorough review on the qualities of different random number generators.

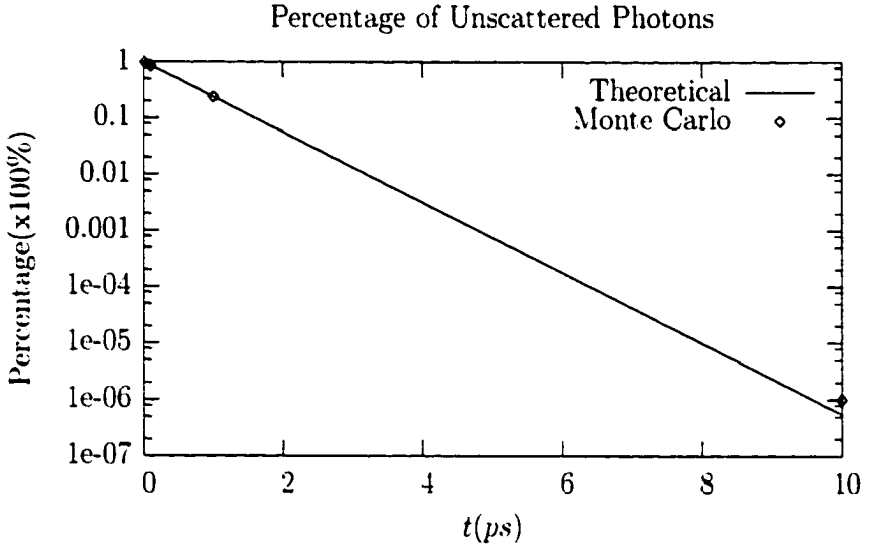

Figure 3.4: Percentage of unscattered photons vs time. The impulses are from Monte Carlo calculations and lies close to the line $p = \exp(-\mu_s ct)$

Chapter 4

Photon Migration in Turbid Media Using a Cumulant Approximation to Radiative Transfer

4.1 Introduction

Photon migration in turbid media is a random walk in which rays or photons traverse a medium of scatterers and absorbers, and undergo multiple scattering and absorption events before escaping. A natural framework to deal with this type of problem is provided by the theory of radiative transfer in Chandrasekhar's classic text [72]. The linear Boltzmann equation governs the radiation field in a medium that absorbs, emits, and scatters radiation [73]. Because the Boltzmann equation is a non-separable, integro-differential equation of first order for which an exact closed form solution is not known except for a few special cases, various approximation have

been devised [60, 72, 74]. The most common approximation is the diffusion approximation, which corresponds to the lowest-order truncation in the spherical harmonic expansion of the photon distribution function. It follows from the Boltzmann equation under the assumption that the photon distribution is almost isotropic after a sufficient large number of scattering events, and thus provides an asymptotic approximation applicable to later times [61]. The diffusion approximation is invalid when the incident photon still retains its directionality preference. Moreover, approximations using higher-order truncation in the spherical harmonics expansion of the photon distribution function are still inefficient in describing the ballistic movement of photons at early times [67]. Yoo et. al. [38] reported that the diffusion approximation fails for small and intermediate scattering ranges. The range of failure is proportional to the transport mean free path $l_t = l_s/(1-g)$ where l_s is the scattering mean free path and g the scattering anisotropy (the average cosine of the scattering angle). For one important class of applications of photon migration in a turbid medium–the medical applications, the medium has a strongly peaked phase function in the forward direction and a typical transport mean free path $l_t \sim 1$mm for human breast tissue. The diffusion approximation is thus incorrect for a substantial scattering range. In optical tomography [5–9, 24] where the distribution of inhomogeneities inside a highly scattering medium is reconstructed from measurements of the transmitted light surrounding the medium, the diffusion approximation yields a much underestimated weight function when any separation between the source, the inhomogeneity and the detector is small. This error may distort the signal from the inhomogeneity inside the medium because the weight function near surface is usually much larger than that inside.

Recently, an analytical solution to the Boltzmann equation was derived by Cai et.

al. [49,51] in an infinite uniform medium using a cumulant expansion. An exact but formal solution to the Boltzmann equation yields the photon distribution function $I(\mathbf{r}, \mathbf{s}, t)$ at position $\mathbf{r}$, direction $\mathbf{s}$ and time t,

$$I(\mathbf{r}, \mathbf{s}, t) = \left\langle \delta(\mathbf{r} - c\int_0^t \mathbf{s}(t')dt')\delta(\mathbf{s}(t) - \mathbf{s}) \right\rangle, \tag{4.1}$$

for a source $\delta(\mathbf{r} - \mathbf{r}_0)\delta(\mathbf{s} - \mathbf{s}_0)\delta(t)$ where $\langle\rangle$ means an ensemble average in photon direction space. Eq. (4.1) is evaluated in Fourier space with use of the well-known cumulant expansion theorem [75,76]. An algebraic closed-form of expression is obtained from Eq. (4.1) for an arbitrary nth order cumulant. This expansion is inherently different from the spherical harmonics expansion of the photon distribution. The first order cumulant calculation determines the *exact* center position of the photon distribution; the second order cumulant calculation determines the *exact* half width of the photon distribution; and higher order cumulant calculations provide progressively more details of the shape of the photon distribution but do not modify the cumulants of lower order. This is a major advantage of the cumulant expansion. The photon distribution approaches a Gaussian distribution as the number of scattering events increases according to the central limit theorem [75, 76]. So it is not surprising that the second order cumulant solution with a correct center position and half width has already provided a clear picture of the time evolution of photon migration from the initial ballistic to the final diffusive regime–that photons migrate with a center that advances in time, and with an ellipsoidal contour that grows and changes shape [49].

The cumulant solution depends explicitly on the phase function of the medium and involves a complicated numerical integration over angular parameters to build a forward model. Hence it is inconvenient for direct use in image reconstruction. An

approximate form of the second order cumulant solution relating the scattered wave field directly to the weak inhomogeneities in an infinite space was later proposed by me and others [50], which retains the main features of photon propagation at both early and later times and reduces to the conventional diffusion approximation at later times. The result is a new transport forward model which provides a better description of photon migration at early times and includes the diffusion approximation as its asymptotic behavior at later times.

In this chapter, we will first extend the second order cumulant solution to planar geometries (semi-infinite and slab media) after a brief review of the main results of the cumulant solution to the Boltzmann equation in an infinite space. The result of the Monte Carlo simulation is then presented for both infinite and semi-infinite media to verify the behavior of the second order cumulant solution at both early and later times. The weight function for image reconstruction of weak inhomogeneities is calculated with use of the simplified cumulant and diffusion approximations for semi-infinite and slab media. The results from the two approximations are compared. The advantage of this new model over the diffusion approximation is then discussed.

4.2 Theory

The Boltzmann equation for photon distribution function $I(\mathbf{r}, \mathbf{s}, t)$ at position $\mathbf{r}$, direction $\mathbf{s}$ and time t from a unit source at position $\mathbf{r}_0$ propagating along $\mathbf{s}_0$ at time $t = 0$, is given by [77]

$$\frac{\partial}{\partial t} I(\mathbf{r}, \mathbf{s}, t) + c\mathbf{s} \cdot \nabla_{\mathbf{r}} I(\mathbf{r}, \mathbf{s}, t) + c[\mu_s(\mathbf{r}) + \mu_a(\mathbf{r})] I(\mathbf{r}, \mathbf{s}, t)$$

$$= c\mu_s(\mathbf{r}) \int ds' P(\mathbf{s}, \mathbf{s}') I(\mathbf{r}, \mathbf{s}', t) ds' + \delta(\mathbf{r} - \mathbf{r}_0)\delta(\mathbf{s} - \mathbf{s}_0)\delta(t) \tag{4.2}$$

where c is the light speed inside the medium, μ_a and μ_s denote the position-dependent absorption and scattering coefficients with a unit of inverse length, and $P(\mathbf{s}, \mathbf{s}')$ is the normalized phase function of the light propagation in the medium. The known phase function is assumed to depend only on the scattering angle $\mathbf{s}\cdot\mathbf{s}'$, and is then expandable in Legendre polynomials,

$$P(\mathbf{s}, \mathbf{s}') = (4\pi)^{-1} \sum_l a_l \, \mathrm{P}_l(\mathbf{s} \cdot \mathbf{s}'). \tag{4.3}$$

Eq. (4.2) is non-separable. However the evolution in direction space, $F(\mathbf{s}, t|\mathbf{s}_0) = \int d^3\mathbf{r} I(\mathbf{r}, \mathbf{s}, t|\mathbf{r}_0, \mathbf{s}_0)$, obeys a separable equation with our solution [49]

$$F(\mathbf{s}, t|\mathbf{s}_0) = (4\pi)^{-1} \sum_l (2l + 1) \exp(-g_l t) \, \mathrm{P}_l(\mathbf{s} \cdot \mathbf{s}_0) \tag{4.4}$$

for an arbitrary phase function specified by Eq. (4.3). Here $g_l = c\mu_s[1 - a_l/(2l + 1)]$, especially $g_0 = 0$ and $g_1 = c\mu_s'$ where μ_s' is the reduced scattering coefficient. The formal solution to the Boltzmann equation, Eq. (4.1), is then evaluated by: expressing its first δ-function of position $\mathbf{r}$ as an integral of $\exp[i\mathbf{k} \cdot (\mathbf{r} - c\int_0^t \mathbf{s}(t')dt']$ over $\mathbf{k}$ in the Fourier space, making a cumulant expansion of the latter, and calculating the cumulants in the direction space with use of the exact Green's function $F(\mathbf{s}, t|\mathbf{s}_0)$ [51].

An arbitrary order of cumulant solution can be calculated [51] with higher order cumulants providing progressively more details about the photon distribution [See Table 4.1]. Because the photon distribution approaches a Gaussian distribution when the number of the scattering events increases regardless of the details of the scattering,

a second order cumulant solution is sufficient at later times. At early times, the photons' spread is narrow compared to the resolution of the detector, hence the detailed shape is less important than the correct position and half-width of the beam. We emphasize the center of the position and half width obtained from the second order cumulant solution is *exact* and will not be altered by higher order cumulant solutions.

Cumulant	What It Describes	For a Gaussian Distribution
$\langle x \rangle_c$	center position	center position
$\langle x^2 \rangle_c$	half spread	deviation σ^2
$\langle x^3 \rangle_c$	skewness	0
$\langle x^4 \rangle_c$	kurtosis	0

Table 4.1: Cumulants describe the shape of a probability distribution.

The second order cumulant solution of the photon density $N^{(0)}(\mathbf{r}, t|\mathbf{r}_0, \mathbf{s}_0) = \int ds I^{(0)}(\mathbf{r}, \mathbf{s}, t|\mathbf{r}_0, \mathbf{s}_0)$ for an incident source propagating along the positive z-axis ($\mathbf{s}_0 = \hat{z}$) in a uniform medium, is given by [49]

$$\begin{aligned} N^{(0)}(\mathbf{r}, t|\mathbf{r}_0, \mathbf{s}_0) &= \frac{1}{(4\pi D_{zz} ct)^{1/2}} \frac{1}{4\pi D_{xx} ct} \exp\{-\frac{(z - z_0 - R_z)^2}{4D_{zz} ct}\} \\ &\quad \times \exp\{-\frac{(x - x_0)^2 + (y - y_0)^2}{4D_{xx} ct}\} \exp(-\mu_a ct) \end{aligned} \tag{4.5}$$

with a moving center located at

$$R_z = l_t[1 - \exp(-ct/l_t)] \tag{4.6}$$

and the diffusion coefficients

$$D_{xx} = D_{yy} = \frac{c}{3t}\left\{\frac{t}{g_1} + \frac{g_2(1 - \exp(-g_1 t))}{g_1^2(g_1 - g_2)} - \frac{1 - \exp(-g_2 t)}{g_2(g_1 - g_2)}\right\} \tag{4.7}$$

$$D_{zz} = \frac{c}{3t}\left\{\frac{t}{g_1} - \frac{(3g_1 - g_2)[1-\exp(-g_1 t)]}{g_1^2(g_1 - g_2)} + \frac{2[1-\exp(-g_2 t)]}{g_2(g_1 - g_2)} - \frac{3[1-\exp(-g_1 t)]^2}{2g_1^2}\right\}$$

A forward model adding inhomogeneity to the analytical expression of $I^{(0)}(\mathbf{r}, \mathbf{s}, t)$, involves a complicated numerical integration over angular parameters. To avoid this difficulty, we use the following approximation to the second order cumulant solution as the background photon distribution, $I^{(0)}(\mathbf{r}, \mathbf{s}, t)$, in an infinite uniform medium [50],

$$I^{(0)}(\mathbf{r}, \mathbf{s}, t|\mathbf{r}_0, \mathbf{s}_0) = N^{(0)}(\mathbf{r}, t|\mathbf{r}_0, \mathbf{s}_0)F(\mathbf{s}, t|\mathbf{s}_0) - \frac{3}{4\pi}D(t)\mathbf{s}\cdot\nabla_{\mathbf{r}}N^{(0)}(\mathbf{r}, t|\mathbf{r}_0, \mathbf{s}_0), \quad (4.8)$$

in building the photon transport model for image reconstruction where the time-dependent diffusion coefficient $D(t)$ is taken to be an average $D(t) = (D_{xx} + D_{yy} + D_{zz})/3$ of the diffusion coefficient ellipsoid. At early times $t \to 0$, the first term of Eq. (4.8) dominates, and $F(\mathbf{s}, t|\mathbf{s}_0) \to \delta(\mathbf{s}-\mathbf{s}_0)$, $D(t) \to c^2t^2\mu_s'/9 \to 0$, $N^{(0)}(\mathbf{r}, \mathbf{t}|\mathbf{r}_0, \mathbf{s}_0) \to \delta(\mathbf{r} - \mathbf{r}_0 - c(t-t_0)\mathbf{s}_0)$, thus $I^{(0)}(\mathbf{r}, \mathbf{s}, t|\mathbf{r}_0, \mathbf{s}_0)$ provides a correct picture of ballistic motion of photons with speed c along the incident direction $\mathbf{s}_0$. At later times, $F(\mathbf{s}, t|\mathbf{s}_0) \to (4\pi)^{-1}$, $D(t) \to (3\mu_s')^{-1}$, Eq. (4.8) reduces to the photon distribution of the center-moved diffusion approximation [24].

A perturbative method is then used to obtain the forward model when weak inhomogeneities are introduced in the otherwise uniform medium. Making a perturbation expansion of the radiative transfer equation Eq. (4.2) to the first order Born approximation, the change in photon distribution from, $I^{(0)}(\mathbf{r}, \mathbf{s}, t)$ (that of the uniform

background), is derived as:

$$\begin{aligned}\delta I(\mathbf{r},\mathbf{s},t|\mathbf{r}_0,\mathbf{s}_0,t_0) &= \int dt' \int d\mathbf{r}' \int d\mathbf{s}' I^{(0)}(\mathbf{r}',-\mathbf{s}',t-t'|\mathbf{r},-\mathbf{s}) \\ &\times \Big\{ \int d\mathbf{s}'' c\delta[\mu_s P](\mathbf{s}',\mathbf{s}'',\mathbf{r}') I^{(0)}(\mathbf{r}',\mathbf{s}'',t-t_0|\mathbf{r}_0,\mathbf{s}_0) \\ &-c[\delta\mu_s(\mathbf{r}')+\delta\mu_a(\mathbf{r}')] I^{(0)}(\mathbf{r}',\mathbf{s}',t'-t_0|\mathbf{r}_0,\mathbf{s}_0)\Big\} \qquad (4.9)\end{aligned}$$

where $\delta\mu_a$, $\delta\mu_s$ and $\delta[\mu_s P]$ are changes of the absorption coefficient, the scattering coefficient and the angular dependent differential scattering coefficient, from the background to the inhomogeneity, respectively. The optical reciprocity theorem $I^{(0)}(\mathbf{r},\mathbf{s},t-t'|\mathbf{r}',\mathbf{s}') = I^{(0)}(\mathbf{r}',-\mathbf{s}',t-t'|\mathbf{r},-\mathbf{s})$ is used in obtaining Eq. (4.9).

Expanding $\delta[\mu_s P]$ in Legendre polynomials and substituting Eq. (4.8) into Eq. (4.9), the integrations over angular variables in Eq. (4.9) can be analytically performed and yield [50],

$$\begin{aligned}\delta I(\mathbf{r},\mathbf{s},t|\mathbf{r}_0,\mathbf{s}_0) &= -\frac{1}{4\pi}\int dt' \int d\mathbf{r}' c\delta\mu_a(\mathbf{r}') N^{(0)}(\mathbf{r}',t-t'|\mathbf{r},-\mathbf{s}) N^{(0)}(\mathbf{r}',t'|\mathbf{r}_0,\mathbf{s}_0) \\ &+\frac{3c}{4\pi}\int dt' \int d\mathbf{r}' D(t-t')D(t')(\delta\mu_a(\mathbf{r}')+\delta\mu_s'(\mathbf{r}')) \\ &\times\nabla_{\mathbf{r}'} N^{(0)}(\mathbf{r}',t-t'|\mathbf{r},-\mathbf{s})\cdot\nabla_{\mathbf{r}'} N^{(0)}(\mathbf{r}',t'|\mathbf{r}_0,\mathbf{s}_0) \\ &+\frac{3c}{4\pi}\int dt' \int d\mathbf{r}' D(t-t')(\delta\mu_a(\mathbf{r}')+\delta\mu_s'(\mathbf{r}'))\exp(-c\mu_s' t') \\ &\times\Big\{N^{(0)}(\mathbf{r}',t'|\mathbf{r},-\mathbf{s})\mathbf{s}\cdot\nabla_{\mathbf{r}'} N^{(0)}(\mathbf{r}',t-t'|\mathbf{r}_0,\mathbf{s}_0) \\ &-\mathbf{s}_0\cdot\nabla_{\mathbf{r}'} N^{(0)}(\mathbf{r}',t-t'|\mathbf{r},-\mathbf{s}) N^{(0)}(\mathbf{r}',t'|\mathbf{r}_0,\mathbf{s}_0)\Big\} \qquad (4.10)\end{aligned}$$

after neglecting fast decaying terms involving $\exp(-2g_l t)$ for $l \geq 1$. We should point out the optical reciprocity relation is satisfied by both the photon density Eq. (4.5) and the photon distribution Eqs. (4.8) and (4.10). At later times, the term in Eq. (4.10)

containing the exponential decay factor $\exp(-c\mu_s' t')$ can be neglected, the change in photon density, $4\pi\delta I(\mathbf{r}, \mathbf{s}, t)$, in the diffusive limit, is reduced to that in the diffusion approximation (Eq. (14) in Ref. 21).

The restriction of $D(t)$ by taking an average of D_{xx}, D_{yy} and D_{zz} can be relaxed. The diffusion coefficients $D_{xx} = D_{yy}$ and D_{zz} can be used instead. The only change is to replace all the occurrences of the form of $D(t)\nabla_{\mathbf{r}'} N^{(0)}(\mathbf{r}, t|\mathbf{r}_0, \mathbf{s}_0)$ to $D_{xx}(t)(\hat{x}\partial/\partial x + \hat{y}\partial/\partial y)N^{(0)}(\mathbf{r}, t|\mathbf{r}_0, \mathbf{s}_0) + D_{zz}(t)\hat{z}\partial/\partial z' N^{(0)}(\mathbf{r}, t|\mathbf{r}_0, \mathbf{s}_0)$ in both Eqs. (4.8) and (4.10).

4.2.1 Extension to planar geometries

When the scattering medium is bounded, special conditions are needed to set the photon density at the interfaces. The reflection at the interface re-injects the light into the medium. Using a partial current technique, Zhu et. al. [78] showed that the boundary condition for a semi-infinite medium can be written as

$$\left[N^{(0)} - z_e \frac{\partial N^{(0)}}{\partial z}\right]_{z=0} = 0 \tag{4.11}$$

at the interface $z = 0$ where

$$z_e = \frac{2l_t}{3}\frac{1 - R_{\text{eff}}}{1 + R_{\text{eff}}} \tag{4.12}$$

is the so-called extrapolation length. Here R_{eff} is the effective reflectivity at the interface determined by the Fresnel reflection coefficients. The extrapolation length z_e measures the distance outside the medium where the extrapolated energy density from the diffusion approximation vanishes linearly. The exact energy density vanishes at the real surface. A recent study by Popescu et. al. [79] has also shown the dependence of the extrapolation length on the scattering anisotropy.

The extrapolated-boundary condition has been successfully employed for planar geometries such as a slab or a semi-infinite medium in diffuse imaging, in which the photon density is set equal to zero at an extrapolated boundary located a distance z_e outside the turbid medium [24, 80, 81]. The method of images is used to obtain the Green's function in such bounded media. The same technique can be applied here to the Green's function $N^{(0)}(\mathbf{r}, t|\mathbf{r}_0, \mathbf{s}_0)$.

Keeping in mind that the source approaches gradually and stops finally at $\mathbf{r}_0 + \mathbf{s}_0 l_t$ on average with the increase of time, the image of the incident point source at $(x_0, y_0, z_0 \geq 0)$ propagating along the positive z-axis inside a semi-infinite medium with its interface at $z = 0$ is a negative one at $(x_0, y_0, -z_0 - 2z_e - 2l_t)$ propagating along the same direction [Fig. (4.1)]. At early times, both the source and its image have not arrived at the extrapolated boundary and their contributions at the extrapolated boundary can be neglected. As time increases, the contributions at the extrapolated boundary from both the source and image tend to cancel each other as both approach their final stops [empty spots in Fig. (4.1)]. The empty spots just represent the positions of the source and its image in the center-moved diffusion approximation. The Green's function of a semi-infinite medium given by

$$N^{(0)}_{\text{semi}}(\mathbf{r}, t|\mathbf{r}_0, \mathbf{s}_0) = N^{(0)}(\mathbf{r}, t|x_0, y_0, z_0, \mathbf{s}_0) - N^{(0)}(\mathbf{r}, t|x_0, y_0, -z_0 - 2z_e - 2l_t, \mathbf{s}_0). \quad (4.13)$$

thus approximately satisfies the extrapolated-boundary condition.

The same procedure can be easily applied to a slab with its extrapolated boundaries at $z = 0$ and $z = L$. The images of an incident source at (x_0, y_0, z_0) with $0 \leq z_0 \leq L$ propagating along positive or negative z-axis ($s_z = \pm 1$) are a set of positives images at $(x_0, y_0, z_0 + 2nL)$ and a set of negative ones at $(x_0, y_0, -z - 2nL - 2s_z l_t)$,

all propagating along the same direction as the source ($-\infty < n < \infty$ is integer).

4.2.2 Comparison with the Monte Carlo simulation

We will compare the photon densities computed by the diffusion approximation (DA), the cumulant approximation Eqs. (4.5) and (4.8) (CA) and the Monte Carlo method (MC) for an incident collimated pulse first in an infinite space and then in a semi-infinite space. In DA, the incident photons are assumed initially scattered isotropically at a depth of one transport mean free path into the medium as used by Patterson et. al [24]. No such adjustments are performed in CA. The Monte Carlo code is adapted from Prahl et. al. [82] and Wang et. al [83]. Photons are launched one by one into the medium. Each photon (regarded as a packet) starts from the origin of the coordinate system and the first scattering event takes place along the positive z-axis. The step-size (distance between consecutive scattering events) is sampled from an exponential distribution characterized by the total attenuation $\mu_T = \mu_s + \mu_a$, following Beer's law. After each propagation step, the photon packet is split into two parts–a fraction (μ_a/μ_T) is absorbed and the rest scattered. The new propagation direction after scattering (three directional cosines) is sampled by assuming a Henyey-Greenstein phase function [68]. The effect of internal reflection is included in this code. Roulette [84] is used to terminate a photon packet to improve the efficiency of the calculation without introducing a bias. The results in the following paragraphs have been scaled to use the transport mean free path l_t as the unit of the length and the flight time for one transport mean free path in the medium l_t/c as the unit of the time. The source is incident along the positive z-axis at the origin in space and time. Five million photons are used in one run of the Monte Carlo simulation.

The first and second order cumulants (the center position and the half width of the "photon cloud") of the cumulant solution Eq. (4.5) is

$$\langle x(t)\rangle = \langle y(t)\rangle = 0, \qquad \langle z(t)\rangle = l_t[1-\exp(-ct/l_t)]$$
$$\sqrt{\langle \Delta x(t)^2\rangle} = \sqrt{\langle \Delta y(t)^2\rangle} = \sqrt{2D_{xx}(t)ct}, \qquad \sqrt{\langle \Delta z(t)^2\rangle} = \sqrt{2D_{zz}(t)ct} \quad (4.14)$$

where $\langle\rangle$ means an ensemble average of photon positions at a specified time. This theoretical prediction can be easily verified by a Monte Carlo simulation. Fig. (4.2) shows the first two cumulants of photons for an incident pulse along the z-axis at time zero into an infinite medium with anisotropy 0.9. An excellent agreement on the center position (the first order cumulant) and the half width (the second order cumulant) of the photon distribution between our theoretical result and the Monte Carlo simulation is obtained. The half width along xyz directions are very close: the value along z direction is a bit larger than that along the xy direction as predicted by Eq. (4.14).

Fig. (4.3a-c) shows the photon density at positions $(0, 0, 3l_t)$, $(0, 0, 6l_t)$ and $(0, 0, 10l_t)$ computed by all the three different methods for the same infinite medium. At a distance of $3l_t$, the time profile of photon density from the cumulant approximation agrees much better to the Monte Carlo result than DA by providing a correct peak position of photon density. Some fraction of photons arrive faster than the speed of light in this second order cumulant calculation. However, the CA is already a big improvement compared to DA. The result from CA can be further improved when higher order cumulants are used. At a larger distance, all the three methods begin to agree with each other pretty well and the cumulant approximation is better than the diffusion approximation. The difference between results from DA, CA and MC is

negligible when the distance is $10l_t$ or larger.

The calculations using DA, CA and MC are performed again for a semi-infinite medium with its boundary at $z = 0$, whose optical parameters are taken to be the same as the above infinite medium. The source is incident at the origin of the coordinate system and along the positive z-axis (normal to the surface) at time zero. The effective reflectivity is taken to be zero for an absorbing surface and an extrapolation length $z_e = 0.7l_t$ [61] is used in both DA and CA calculations. Fig. (4.4a-c) shows the corresponding results for this example. Again CA shows a much better agreement to the MC than DA. Compared with Fig. (4.3) for the infinite case, the tail of the profiles in Fig. (4.4a-c) for the semi-infinite medium is lower due to the presence of an extra negative image source coming from the boundary condition.

As another example, the backscattered photon intensity $I^{(0)}(\mathbf{r}, -\hat{z}, t)$ at positions $(0, l_t, 0)$ and $(0, 2l_t, 0)$ on the boundary of the above semi-infinite medium is calculated with use of the three different methods [Fig. (4.5)]. In DA, photons diffuse from the adjusted source position $(0, 0, l_t)$ with the constant diffusion coefficient $D = l_t/3$. In CA, back-scattered photons arrive later because the center of photons moves forward along the positive z-direction and diffuse from the moving center with a gradually increasing diffusion coefficient from 0 to $l_t/3$. CA agrees well with the Monte Carlo simulation. The late arrival is close to the causality requirement.

We should point out cumulants higher than second order are required to describe photon migration when only a few scatterings have taken place. Fig. (4.6) shows the photon density at positions $(0, 0, 3l_t)$ and $(0, 0, 6l_t)$ inside an infinite uniform medium with an anisotropy factor $g = 0$. The light is incident along the positive z-axis at the origin of space and time. A separation of $3l_t$ or $6l_t$ is only a few scattering

mean free paths apart. Both the second cumulant approximation and the diffusion approximation agree poorly with the result from a Monte Carlo simulation at early times. However the second order cumulant approximation is still more close to the Monte Carlo result than the diffusion approximation. Higher order cumulants are required to get a better fit of the cumulant approximation to the Monte Carlo result.

4.2.3 Weight function for image reconstruction

The response (the change of the scattered wave field) to a unit absorption or scattering inhomogeneity is usually called the weight function or the Jacobian in medical tomography literature. This quantity plays a central role in image reconstruction regardless of which method is used to obtain the inhomogeneity distribution in a medium. Let's rewrite Eq. (4.10) in the following form,

$$\begin{aligned} 4\pi\delta I(\mathbf{r},\mathbf{s},t|z_0,\mathbf{s}_0) &= -c\int d\mathbf{r}'\delta\mu_a(\mathbf{r}')w_a(\mathbf{r},\mathbf{s},\mathbf{r}_0,\mathbf{s}_0,t;\mathbf{r}') \\ &\quad +\frac{c}{3\mu_s'^2}\int d\mathbf{r}'\delta\mu_s'(\mathbf{r}')w_s(\mathbf{r},\mathbf{s},\mathbf{r}_0,\mathbf{s}_0,t;\mathbf{r}') \end{aligned} \tag{4.15}$$

with the absorption and scattering weight functions defined as

$$\begin{aligned} w_a(\mathbf{r},\mathbf{s},\mathbf{r}_0,\mathbf{s}_0,t;\mathbf{r}') &= \int_0^t dt' N^{(0)}(\mathbf{r}',t-t'|\mathbf{r},-\mathbf{s})N^{(0)}(\mathbf{r}',t'|\mathbf{r}_0,\mathbf{s}_0) \\ &\quad -w_s(\mathbf{r},\mathbf{s},\mathbf{r}_0,\mathbf{s}_0,t;\mathbf{r}')/(3\mu_s'^2) \\ \frac{w_s(\mathbf{r},\mathbf{s},\mathbf{r}_0,\mathbf{s}_0,t;\mathbf{r}')}{9\mu_s'^2} &= \int_0^t dt' D(t-t')D(t')\nabla_{\mathbf{r}'}N^{(0)}(\mathbf{r}',t-t'|\mathbf{r},-\mathbf{s}) \\ &\quad \cdot\nabla_{\mathbf{r}'}N^{(0)}(\mathbf{r}',t'|\mathbf{r}_0,\mathbf{s}_0) \\ &\quad +\int_0^t dt' D(t')\exp[-c\mu_s'(t-t')]N^{(0)}(\mathbf{r}',t-t'|\mathbf{r},-\mathbf{s}) \\ &\quad \times\mathbf{s}\cdot\nabla_{\mathbf{r}'}N^{(0)}(\mathbf{r}',t'|\mathbf{r}_0,\mathbf{s}_0) \end{aligned}$$

$$-\int_0^t dt' D(t-t')\exp(-c\mu_s' t')\mathbf{s}_0\cdot\nabla_{\mathbf{r}'}N^{(0)}(\mathbf{r}', t-t'|\mathbf{r}, -\mathbf{s})$$
$$N^{(0)}(\mathbf{r}', t'|\mathbf{r}_0, \mathbf{s}_0) \tag{4.16}$$

respectively.

Because the Green's function approaches a delta function, i.e., $N^{(0)}(\mathbf{r}, t|\mathbf{r}_0, \mathbf{s}_0) \rightarrow \delta(\mathbf{r}-\mathbf{r}_0-ct\mathbf{s}_0)$ when $t \rightarrow 0$, special attentions must be paid when a numerical integration is carried out for Eq. (4.16). Therefore the range of integration is divided into three areas: $(0, \Delta)$, $(\Delta, t-\Delta)$ and $(t-\Delta, t)$ where $t \gg \Delta > 0$. The end corrections from the integration over $(0, \Delta)$ and $(t-\Delta, t)$ to the weight functions integrated over $(\Delta, t-\Delta)$ range are approximately given by

$$\begin{aligned}
e_a(\mathbf{r}, \mathbf{s}, \mathbf{r}_0, \mathbf{s}_0, t; \mathbf{r}') &= \frac{1}{c}N(\mathbf{r}', t|\mathbf{r}, -\mathbf{s})\delta(x'-x_0)\delta(y'-y_0)\,\mathrm{H}(\Delta-\xi)\,\mathrm{H}(\xi) \\
&\quad +\frac{1}{c}N(\mathbf{r}', t|\mathbf{r}_0, \mathbf{s}_0)\delta(x'-x)\delta(y'-y)\,\mathrm{H}(\Delta-\eta)\,\mathrm{H}(\eta) \\
&\quad -e_s(\mathbf{r}, \mathbf{s}, \mathbf{r}_0, \mathbf{s}_0, t; \mathbf{r}')/(3\mu_s'^2) \\
\frac{e_s(\mathbf{r}, \mathbf{s}, \mathbf{r}_0, \mathbf{s}_0, t; \mathbf{r}')}{9\mu_s'^2} &= -\frac{D(t)}{c}\left(1-\frac{\partial D(t)}{c\partial t}\bigg|_{t=\xi}\right)\mathbf{s}_0\cdot\nabla_{\mathbf{r}'}N(\mathbf{r}', t|\mathbf{r}, -\mathbf{s})\delta(x'-x_0)\delta(y'-y_0) \\
&\quad \times \mathrm{H}(\Delta-\xi)\,\mathrm{H}(\xi) \\
&\quad +\frac{D(t)}{c}\left(1-\frac{\partial D(t)}{c\partial t}\bigg|_{t=\eta}\right)\mathbf{s}\cdot\nabla_{\mathbf{r}'}N(\mathbf{r}', t|\mathbf{r}_0, \mathbf{s}_0)\delta(x'-x)\delta(y'-y) \\
&\quad \times \mathrm{H}(\Delta-\eta)\,\mathrm{H}(\eta)
\end{aligned} \tag{4.17}$$

where $\mathbf{r}' = \mathbf{r}_0 + c\xi\mathbf{s}_0 = \mathbf{r} - \eta c\mathbf{s}$, $\mathbf{s}$ and $\mathbf{s}_0$ are assumed to be along the positive or negative z-axis, and H is the Heaviside function. In the following calculations, the refractive index of the medium is assumed to be 1.33; the absorption and scattering coefficients of the medium are assumed to be $0.003\mathrm{mm}^{-1}$ and $10\mathrm{mm}^{-1}$ respectively, and the the scattering anisotropy 0.9, providing a transport mean free path $l_t = 1\mathrm{mm}$. The offset

Δ is taken to be 0.1ps when more than 99% of the photon packet still concentrates within a cubic of volume $(0.01l_t)^3$. The weight function from a cubic volume $(0.01l_t)^3$ is calculated using the ACM algorithm 698–DCUHRE [85].

The weight functions for a semi-infinite medium are shown in Figs. (4.7) and (4.8) for absorption and scattering inhomogeneities. The back-scattered photons (propagating along negative z-axis) are detected by a detector placed at a position $(0, 2l_t, 0)$, off two transport mean free paths from the source. Figs. (4.7a) and (4.8a) show the response to an inhomogeneity at $(0, 0, z)$ positions which is in the propagation direction of the source at delay 50ps and 500ps. The cumulant approximation (CA) shows a much stronger response from the inhomogeneity in the propagation direction of and close to the source than the diffusion approximation. Both absorption and scattering weight functions from CA reveal a peak at about $0.03l_t$. This peak originates from the initial ballistic motion of the incident photon. In a short time after the photon is launched ($t \to 0$), the photon packet will be positioned at $z^* = ct$ with a spread of half-width approximately $\sqrt{4D(t)ct} = 2ct\sqrt{ct/(3l_t)}$, hence the presence of an absorption or scattering inhomogeneity at position $(0, 0, z < z^*)$, sitting in the ballistic path of the photon, will significantly reduce the number of back-scattered photons received by the detector ($w_a > 0$ and $w_s < 0$ in Eq. (4.15)). In Figs. (4.7b) and (4.8b) where the inhomogeneity is placed at $(0, l_t, z)$mm positions, not sitting in the ballistic path of the photon, this peak is gone.

The diffusion approximation is invalid when the inhomogeneity is too close to the source or the detector. Nevertheless, the weight function from DA is plotted over the full z-range for comparison. A peak is found in the absorption weight function [Fig. (4.7a)] and a crossing of zero in the scattering weight function [Fig. (4.8a)] at $z =$

l_t, because of the artificial adjustment of the source position to one transport mean free path into the medium performed in the center-moved diffusion approximation [24] and the singularity of the Green's function in DA when the inhomogeneity and the source overlap.

A larger disagreement between CA and DA is observed in the scattering weight function than in the absorption weight function. The absorption weight functions from CA and DA agree with each other relatively well except for a region of depth of l_t near the surface when the inhomogeneity is in the propagation direction of the source, or in the field of view of the detector. The scattering weight functions from CA and DA disagree significantly within the region of depth of at least $2l_t$ close to the surface. The detector can not see the region of depth beyond $ct/2$ at time t. This condition is better observed by CA because CA shows a faster decay rate of both the absorption and scattering weight functions with the increase of the depth [Figs. (4.7) and (4.8)].

The absorption and scattering weight functions for a slab is shown in Figs. (4.9) and (4.10). The slab has the same optical parameter as the semi-infinite medium. The thickness of the slab is $d = 30l_t$. The source is at the origin $(0.0.0)$. The detector is placed on the opposite side of the slab, $(0.0.30l_t)$, in the propagation direction of the source. The weight function by the cumulant approximation and the diffusion approximation are strictly symmetric about the plane $z = d/2$. The agreement between CA and DA for the absorption weight function is better than for the scattering weight function. Both CA and DA produce close results for the inhomogeneity not located near the boundary. When the inhomogeneity is placed along the line $(0.0.z)$, in the propagation direction of the source and in the field of

view of the detector, two peaks at about $0.03l_t$ and $d - 0.03l_t$ appear in CA; two peaks in the absorption weight function [Fig. (4.9a)] and two crossings of zero in the scattering weight function [Fig. (4.10a)] appear in DA at l_t and $d - l_t$.

4.3 Discussion

We attribute the formation of a peak very close to the surface but not on the surface (about $0.03l_t$ into the medium) of the absorption and scattering weight function in the cumulant approximation to the initial ballistic motion of the incident photon. The photon penetrates into the medium with an initial speed of c and with its center approaching and stopping at one transport mean free path into the medium. Hence the effect is only significant when the inhomogeneity is in the propagation direction of the source or in the field of view of the detector, and the peak response shifts away from the surface of the medium.

It seems that there is confusion in the optical tomography literature on the way chosen to position the source and the detector to compensate for the initial ballistic motion of the photon [24, 86, 87]. From our more accurate result Eq. (4.10), the source and the detector terms appear in a form of $N^{(0)}(\mathbf{r}', \tau|\mathbf{r}, -\mathbf{s})$ and $N^{(0)}(\mathbf{r}', \tau|\mathbf{r}_0, \mathbf{s}_0)$ respectively. The source and the detector approach gradually and stop at $\mathbf{r}_0 + l_t\mathbf{s}_0$ and $\mathbf{r} - l_t\mathbf{s}$, respectively, with increase of time where $\mathbf{s}_0$ and $\mathbf{s}$ are the propagating direction of the incident and outgoing photon. The positioning of both the source and the detector for one transport mean free path into the medium is hence mandatory if the diffusion approximation is used. The curves for DA in Figs. (4.8) and (4.10) are calculated with use of this adjustment. The DA will deviate from the CA significantly over the full range of depth if the adjustment on the position of the source or the

detector is not performed.

The diffusion approximation for image reconstruction substantially underestimates the contribution to the emission measurement from the inhomogeneity in the propagation direction of and close to the source, or in the field of view and close to the detector. This error may distort the signal from the inhomogeneity inside the medium because the weight function near surface is usually much larger than that inside, and may lead to a failure in image reconstruction. The high response from the region near surface is not desirable when the inhomogeneity inside the medium is to be detected in the transmission or backscattering measurements. The cancellation between multiple measurements using nearby wavelengths may help reduce this effect.

In conclusion, we have presented a cumulant approximation to radiative transfer which provides an analytical tool to describe photon migration at both early and later times-from the initial ballistic motion till the final diffuse regime. To a second order cumulant, the solution agrees with the Monte Carlo simulation at later times and provides a correct peak position in time for photon arrivals at early times, in both an infinite medium and a bounded medium with a planar geometry. The initial ballistic motion of photon produces a strong peak in the response from absorption and/or scattering inhomogeneities which are in the propagation direction of and close to the source, or in the field of view of and close to the detector, at both early and later times.

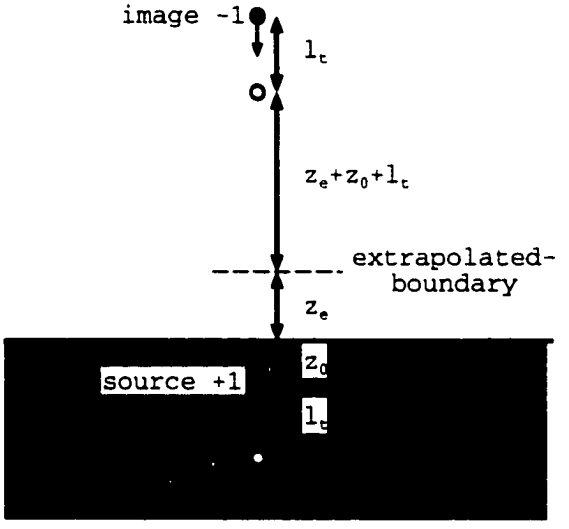

Figure 4.1: The incident source at position $(x_0, y_0, z_0 \geq 0)$ and its image source at $(x_0, y_0, -z_0-2z_e-2l_t)$ propagating along the positive z-axis in a semi-infinite medium $(z \geq 0)$ with its interface at $z = 0$. The source and its image move from their original positions (dark spots) to their final stops (empty spots) at later times.
The positive z direction is downward on the paper.

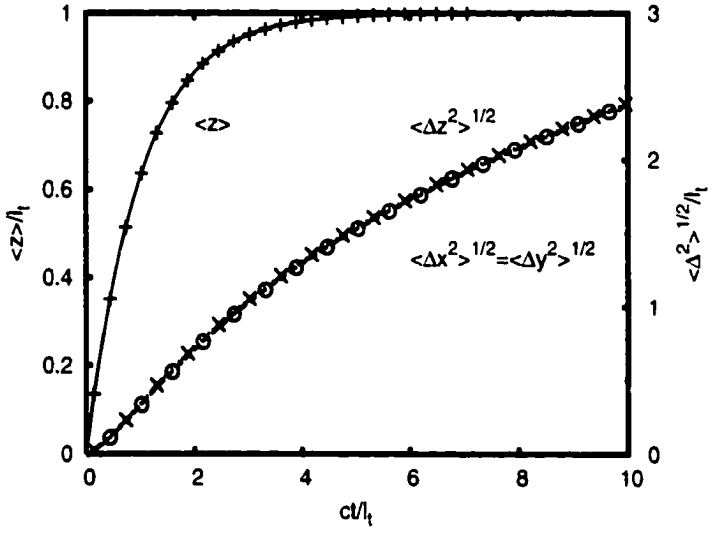

Figure 4.2: The center position and the half width of a photon cloud inside a uniform infinite medium with anisotropy equal to 0.9. The plus, cross and circular signs represent the central z coordinate, the half spread in the z direction, and the half spread in the xy directions of the photon cloud from a Monte Carlo simulation, respectively.

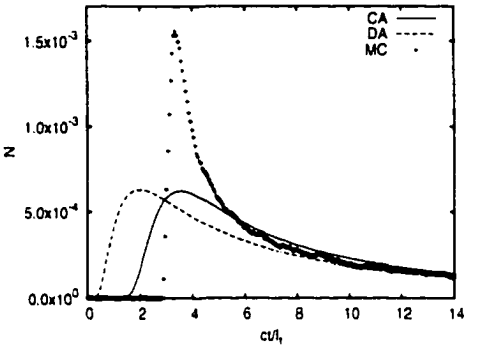

(a)

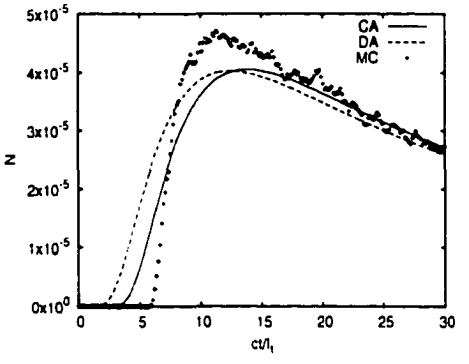

(b)

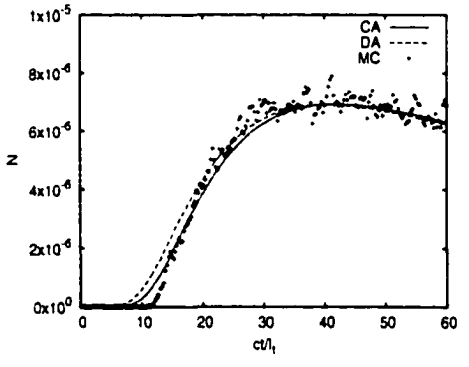

(c)

Figure 4.3: Photon density at positions (a) $(0, 0, 3l_t)$, (b) $(0, 0, 6l_t)$, and (c) $(0, 0, 10l_t)$ vs time normalized to a unit source in an infinite medium. The source is incident along the positive z-axis at the origin of the coordinate system and at time zero. The three curves are computed by the diffusion approximation (DA), the cumulant approximation (CA) and the Monte Carlo method (MC) respectively. Note the CA arrival time is much close to the correct MC arrival time than the DA.

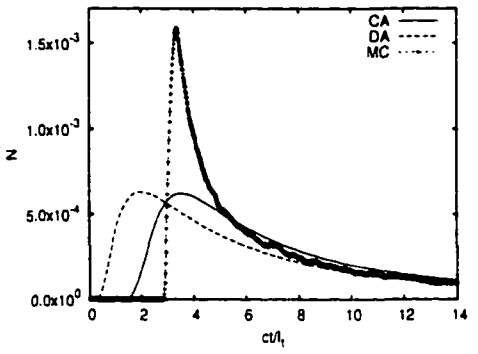

(a)

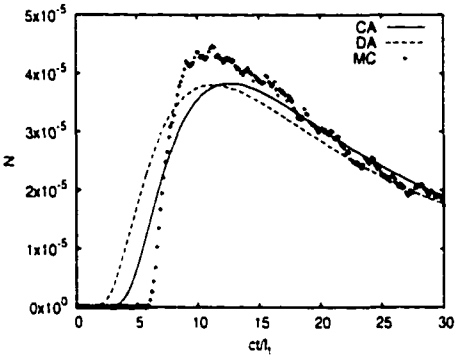

(b)

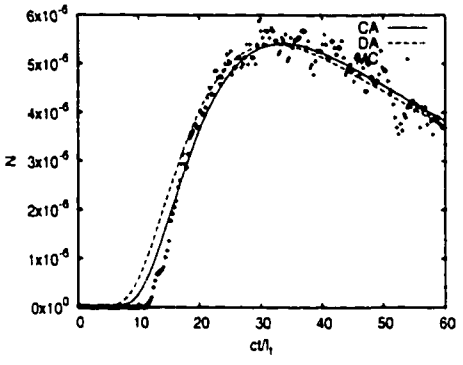

(c)

Figure 4.4: Photon density at positions (a) $(0, 0, 3l_t)$, (b) $(0.0.6l_t)$. (c) $(0.0.10l_t)$ vs time normalized to a unit source in a semi-infinite medium. The source is incident normal to the surface of the medium and along the positive z-axis at the origin of the coordinate system and at time zero.

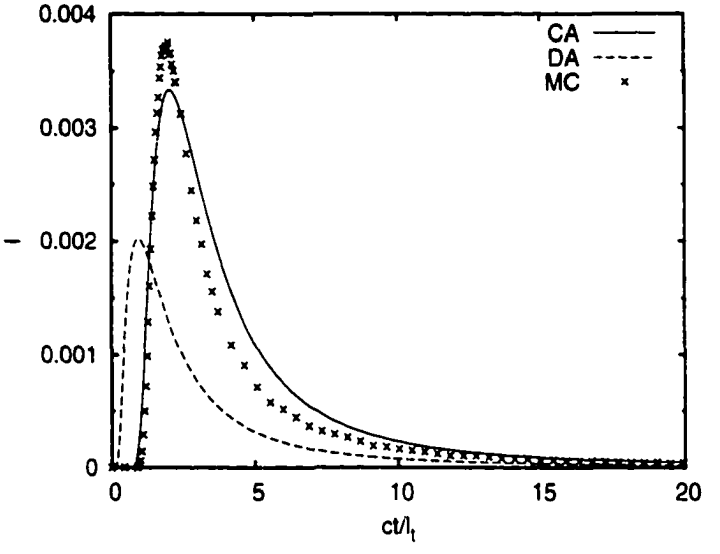

(a)

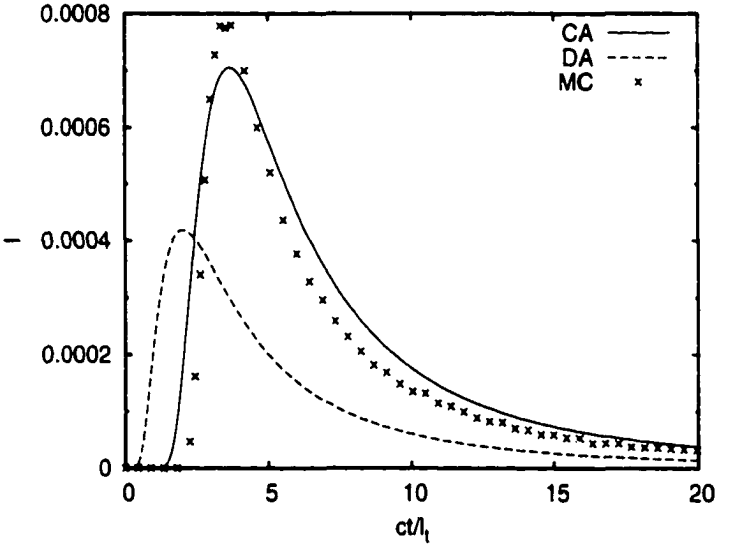

(b)

Figure 4.5: The backscattered photon intensity $I(\mathbf{r}, -\hat{z}, t)$ at positions (a) $(0, l_t, 0)$ and (b) $(0, 2l_t, 0)$ on the boundary of a semi-infinite medium vs time normalized to a unit source in a semi-infinite medium. The source is incident normal to the surface of the medium and along the positive z-axis at the origin of the coordinate system and at time zero.

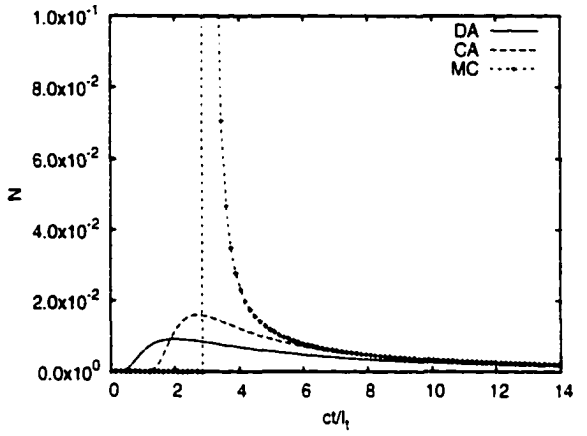

(a)

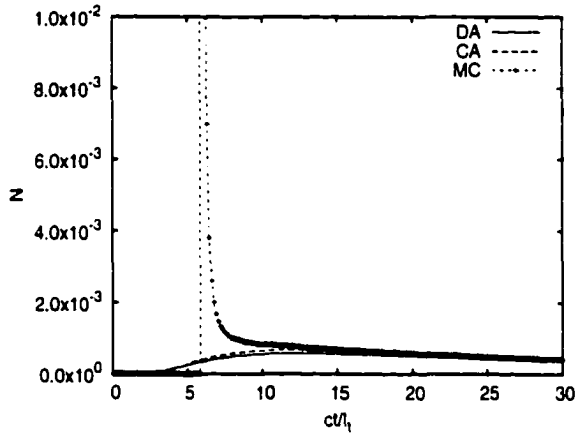

(b)

Figure 4.6: Photon density at positions (a) $(0, 0, 3l_t)$ and (b) $(0, 0, 6l_t)$ vs time normalized to a unit source in an infinite medium with $g = 0$. The source is incident along the positive z-axis at the origin of the coordinate system and at time zero. The peak of MC goes beyond the scale of the y axis and is not shown in either (a) or (b).

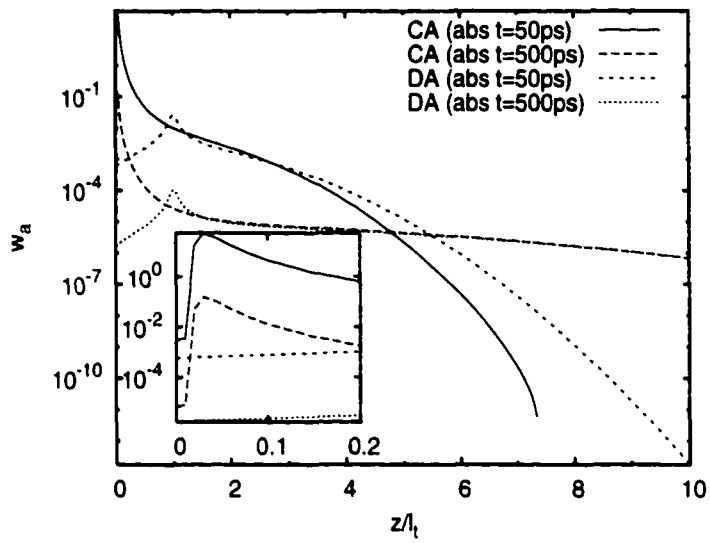

(a)

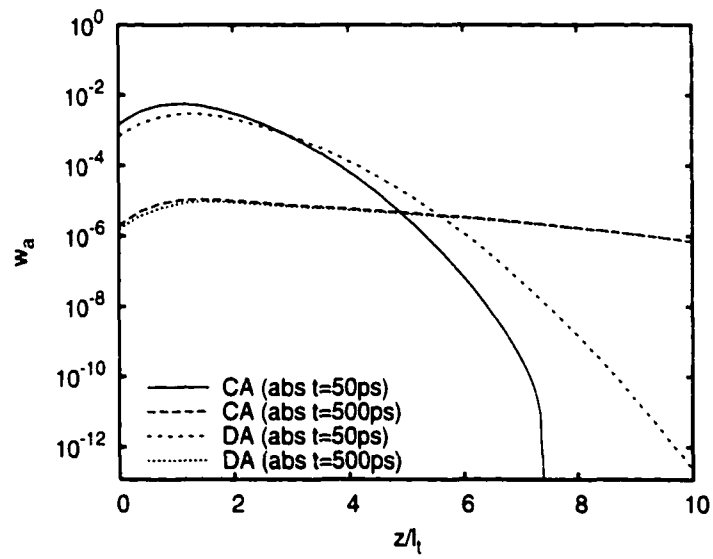

(b)

Figure 4.7: Weight functions for a semi-infinite medium where the absorption inhomogeneity is at (a) $(0, 0, z)$, in the propagation direction of the source; (b) $(0, l_t, z)$, off by one transport mean free path. Profiles at two delay times $t = 50$ps and $t = 500$ps are plotted for both the cumulant approximation (CA) and the diffusion approximation (DA). The insets re-plot the weight functions in a logarithm scale.

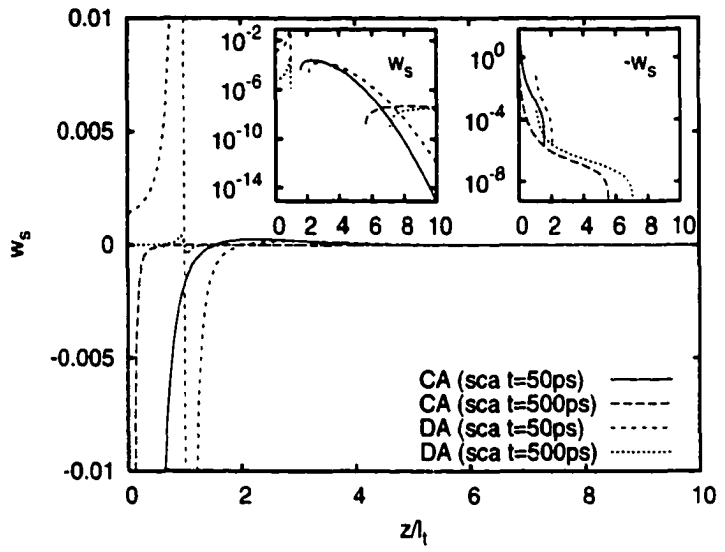

(a)

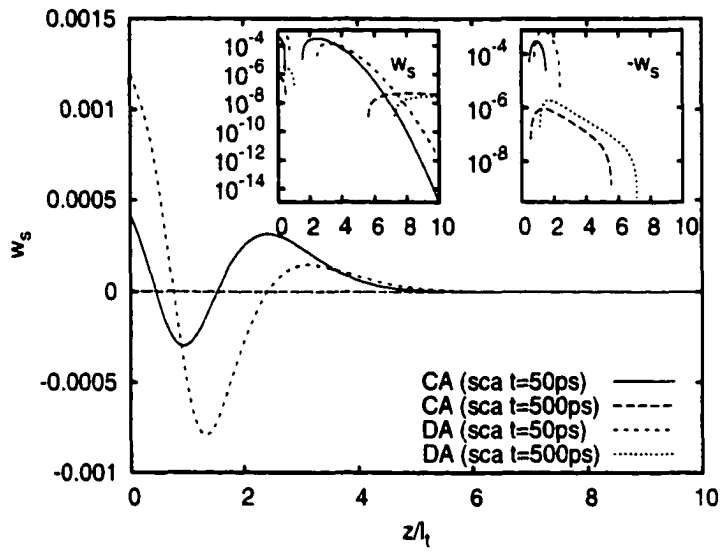

(b)

Figure 4.8: Weight functions for a semi-infinite medium where the scattering inhomogeneity is at (a) $(0, 0, z)$, in the propagation direction of the source; (b) $(0, l_t, z)$, off by one transport mean free path. Profiles at two delay times $t = 50$ps and $t = 500$ps are plotted for both the cumulant approximation (CA) and the diffusion approximation (DA). The insets re-plot the weight functions in a logarithm scale.

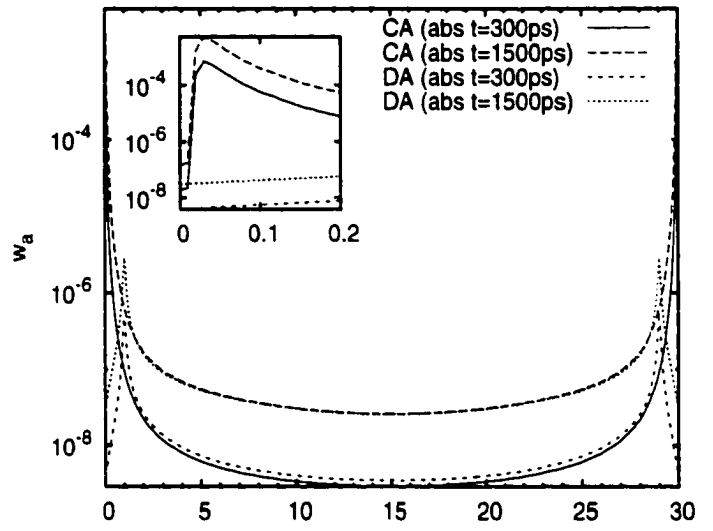

(a)

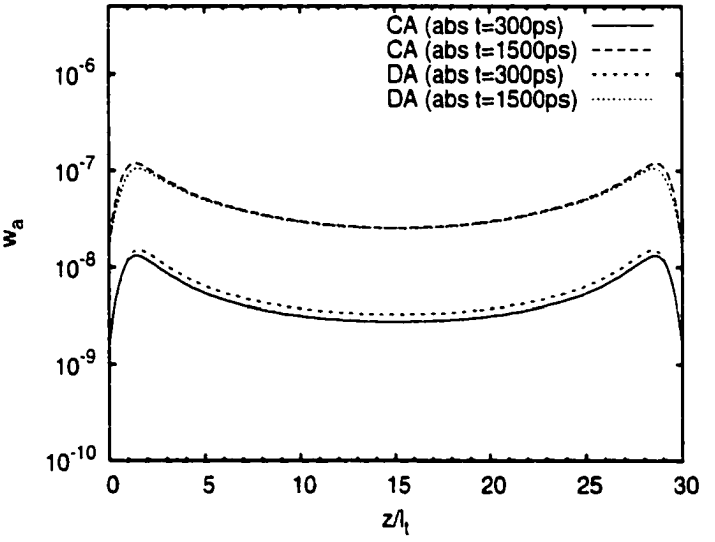

(b)

Figure 4.9: Weight function for a slab where the absorption inhomogeneity is at: (a) $(0, 0, z)$, in the propagation direction of the source, (b) $(0, l_t, z)$, off by one transport mean free path. Weight functions calculated from the cumulant (CA) and diffusion (DA) approximations are plotted for time delays of $t = 300$ps and $t = 1500$ps. The insets re-plot the weight functions in a logarithm scale.

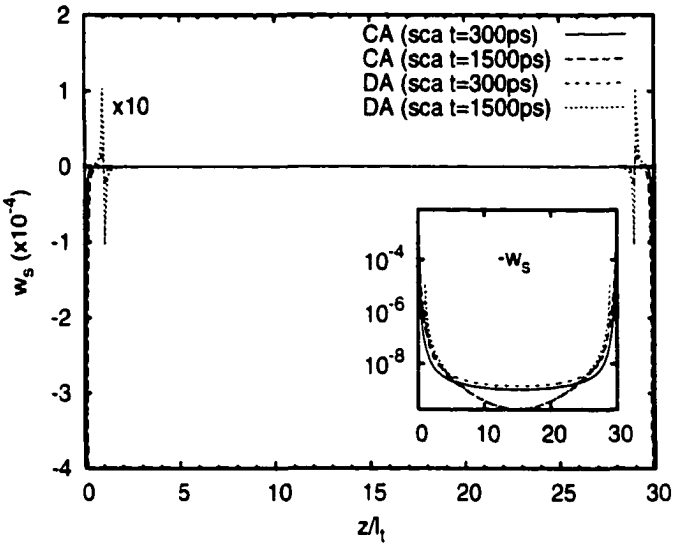

(a)

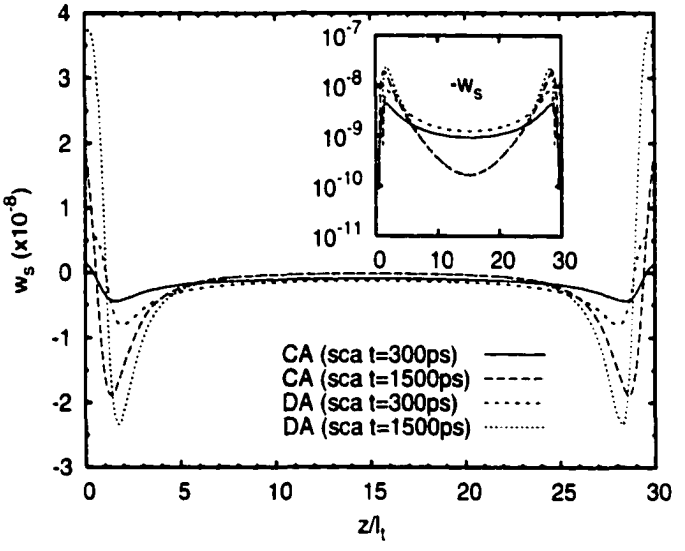

(b)

Figure 4.10: Weight function for a slab where the scattering inhomogeneity is at: (a) $(0, 0, z)$, in the propagation direction of the source, (b) $(0, l_t, z)$, off by one transport mean free path. Weight functions calculated from the cumulant (CA) and diffusion (DA) approximations are plotted for time delays of $t = 300$ps and $t = 1500$ps. The insets re-plot the weight functions in a logarithm scale.

Chapter 5

Regularized Inversion

5.1 Introduction to inverse problem and regularization methods

The inverse problem is *ill-posed*, i.e., it has no unique solution. An example is the measurement using an apparatus

$$y(\xi) = \int A(\xi, \eta)x(\eta)d\eta + \epsilon(\eta) \tag{5.1}$$

where $y(\xi)$ is the measurement, $x(\eta)$ is the signal, $K(\xi, \eta)$ is the response function of the apparatus, $\epsilon(\xi)$ is the noise, or its discrete form

$$y = Ax + \epsilon \tag{5.2}$$

where $A \in \mathbf{R}^{m \times n}$ is a $m \times n$ matrix, $x \in \mathbf{R}^n$, $y \in \mathbf{R}^m$ and $\epsilon \in \mathbf{R}^m$ are vectors. A will be called the kernel of measurement hereafter.

The direct inversion of Eq. (5.1) or (5.2) will unfortunately fail due to the fact that the smoothing operator A may map apparently different x into a very similar y even without noise. It is found that the oscillations in the solutions must be suitably suppressed to get the "best possible" approximate solution, or be *regularized*. Tikhonov first introduced regularization methods in 1963 [52]. Since then, the regularization methods are actively developed and widely applied in all kinds of ill-posed problems [88–92]. Prior information on the signal x is included in one form or another to recover some of the information lost by the filtering effects of the forward operator, discretization of the observation, and noise contamination. A regularized solution is a solution that utilizes the prior information and strikes a balance between the goodness of fit and closeness to the prior information.

Two main problems when applying regularization method to an inverse problem are:

1. Which regularization to use in a particular problem
2. To what extent can noisy fluctuations be suppressed without damaging real oscillations. This leads to a choice of the regularization parameters or a stopping rule in the regularization methods

In this chapter, we will concentrate on the most commonly used regularization method – the Tikhonov regularization method. It forms the basis for image reconstruction in the following chapters.

5.2 Tikhonov regularization

The discrete ill-posed problem Eq. (5.2) can be regarded as a particular class of discrete least squares problems (see, for example, Hansen [93]):

$$\min_{\mathbf{x}} ||A\mathbf{x} - \mathbf{b}||, \; A \in \mathbf{R}^{m \times n}, \; m \geq n \tag{5.3}$$

where the singular values of the matrix A decay gradually to zero in such a fashion that A is very ill-conditioned.

Most numerical methods for treating this kind of problem seek to replace the problem whose kernel A has a large condition number with a *nearby* well-conditioned problem whose solution approximates the required solution and, in addition, is a more satisfactory solution than the ordinary (least squares) solution. The latter goal is achieved by incorporating additional information about the sought solution, often that the computed solution should be smooth. Such methods are called *regularization methods*, and they always include a so-called regularization parameter λ which controls the degree of smoothing or regularization applied to the problem.

One of the best known regularization methods is Tikhonov regularization [52] whose solution x_λ is defined as the solution to the following least squares problem:

$$\min_{\mathbf{x}} \left\{ ||A\mathbf{x} - \mathbf{b}||^2 + \lambda^2 ||L\mathbf{x}||^2 \right\} \tag{5.4}$$

where $A \in \mathbf{R}^{m \times n}$, $L \in \mathbf{R}^{p \times n}$ and $m \geq n \geq p$. The central idea is to seek a balance between the goodness of fit $||A\mathbf{x} - \mathbf{b}||^2$ and the reliability (closeness to the prior information) of the solution $||L\mathbf{x}||^2$.

The formal solution to the Tikhonov regularized least square problem can be easily

found

$$\mathbf{x}_\lambda = (A^T A + \lambda^2 L^T L)^{-1} A^T b$$

whose property can best be analyzed through the generalized singular value decomposition (GSVD) of the matrix pair (A, L).

The GSVD of the matrix pair (A, L) has the form

$$A = U\Sigma X^{-1}, \quad L = VMX^{-1}. \tag{5.5}$$

Here, $U \in R^{m\times n}$, and $V \in R^{p\times p}$ are orthonormal such that $U^T U = I_n$ and $V^T V = I_p$; $X \in R^{n\times n}$ is a non-singular matrix, and Σ and M are of the form

$$\Sigma = \begin{pmatrix} \Sigma_p & 0 \\ 0 & I_{n-p} \end{pmatrix}, \quad M = \begin{pmatrix} M_p & 0 \end{pmatrix}. \tag{5.6}$$

The matrix $\Sigma_p = \mathrm{diag}(\sigma_i)$ and $M_p = \mathrm{diag}(\mu_i)$ are both $p \times p$ diagonal matrices whose diagonal elements satisfy $\sigma_i^2 + \mu_i^2 = 1$ and are ordered such that

$$0 \le \sigma_1 \le \ldots \le \sigma_p, \quad 1 \ge \mu_1 \ge \ldots \ge \mu_p \ge 0. \tag{5.7}$$

The generalized singular values γ_i of (A, L) are then defined as the positive numbers

$$\gamma_i = \frac{\sigma_i}{\mu_i}, \quad i = 1, \ldots, p. \tag{5.8}$$

Write $X = (\xi_1, \ldots, \xi_n)$, $U = (\mathbf{u}_1, \ldots, \mathbf{u}_n)$, the solution to (5.4) is given by [94]:

$$\mathbf{x}_\lambda = \sum_{i=1}^{p} \frac{\gamma_i^2}{\gamma_i^2 + \lambda^2} \frac{\mathbf{u}_i^T \mathbf{b}}{\sigma_i} \xi_i + \sum_{i=p+1}^{n} (\mathbf{u}_i^T \mathbf{b}) \xi_i. \tag{5.9}$$

The condition for the existence of a regularized solution is that the Fourier coefficients $|\mathbf{u}_i^T \mathbf{b}|$ decay to zero faster than the generalized singular values γ_i, the so-called Picard condition [93]. The smoother the kernel A, the faster the generalized singular values decay to zero; and the smaller the singular values, the more oscillations in the corresponding singular functions. Furthermore, the existence of vanishing values $\gamma_i = 0$ indicates non-uniqueness of the solution.

The standard form of Tikhonov regularization has $L = I$. If the exact $\mathbf{x}$ is smooth, a form of a differential operator may be a better choice for L [90]. The standard form of Tikhonov regularization can be proved to be the optimal regularization method for an inverse problem with the exact $\mathbf{x}$ which is bounded and close to zero nearly everywhere [91].

5.3 Determination of the regularization parameter

5.3.1 L-curve method

For the regularized solution (5.9), its residual norm and side constraint norm can easily be calculated,

$$\begin{aligned} \rho(\lambda) &= ||A\mathbf{x}_\lambda - \mathbf{b}|| \\ &= \left\{ \sum_{i=1}^{p} \left[\frac{\lambda^2}{\gamma_i^2 + \lambda^2} \mathbf{u}_i^T \mathbf{b} \right]^2 + \sum_{i=p+1}^{n} (\mathbf{u}_i^T \mathbf{b})^2 \right\}^{1/2} \end{aligned} \tag{5.10}$$

$$\begin{aligned}\eta(\lambda) &= ||L\mathbf{x}_\lambda|| \\ &= \left\{\sum_{i=1}^{p}\left[\frac{\gamma_i^2}{\gamma_i^2+\lambda^2}\frac{\mathbf{u}_i^T\mathbf{b}}{\gamma_i}\right]^2\right\}^{1/2}.\end{aligned}$$

The L-curve is a double logarithmic plot of the norm of residuals $\log\rho(\lambda)$ versus the norm of the solution seminorm $\log\eta(\lambda)$, typically with an L-shaped corner. The optimal λ is the L-corner, or the point with the maximum curvature in the plot which can be located iteratively [53]. The method of the L-curve is popularized by Hansen [53, 94]. A good regularization parameter λ is one that corresponds to a regularized solution near the corner of the L-curve because in this region there is a good compromise between achieving a small residual norm $||A\mathbf{x}_\lambda - \mathbf{b}||$ and keeping the solution seminorm $||L\mathbf{x}_\lambda||$ reasonably small. A typical L-curve is shown in Fig. (5.1).

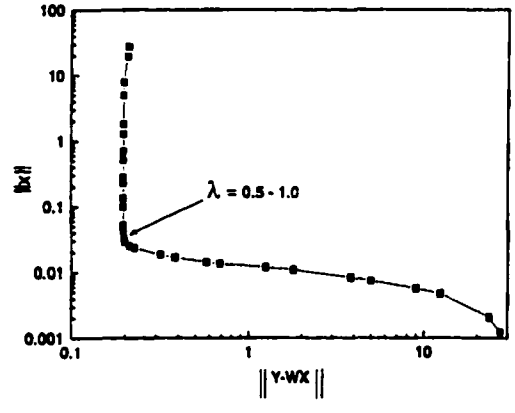

Figure 5.1: A typical L-curve.

5.3.2 Generalized cross validation

In the model (5.2), when the noise ϵ has the form of a normal distribution $\mathbf{N}(0, \sigma^2 I)$, Wahba et. al. [95] proves the best regularization parameter λ is the minimizer of $V(\lambda)$ given by:

$$V(\lambda) = \frac{1}{m}||(I - A(\lambda))y||^2 / \left[\frac{1}{m}Trace(I - A(\lambda))\right]^2 \tag{5.11}$$

where

$$A(\lambda) = A(A^*A + \lambda I)^{-1}A^* \tag{5.12}$$

Use the singular value decomposition of A, namely, $A = U\Sigma V^*$, where U is an $m \times m$ orthogonal matrix, V is an $n \times n$ orthogonal matrix, and $\Sigma = \begin{pmatrix} \mathrm{diag}(\sigma_\nu) \\ 0 \end{pmatrix}$ is an $m \times n$ matrix whose entries are the square roots of A^*A. It is easy to prove:

$$\begin{aligned} V(\lambda) &= \frac{1}{m}\sum_{\nu=1}^{m}\left(\frac{\lambda}{\sigma_\nu^2 + \lambda}\right)^2 (U_\nu^* y)^2 / \left[\frac{1}{m}\left(\sum_{\nu=1}^{n}\frac{\lambda}{\sigma_\nu^2 + \lambda} + m - n\right)\right]^2 \qquad (5.13) \\ &= \frac{1}{m}\left[\sum_{\nu=1}^{n}\left(\frac{\lambda}{\sigma_\nu^2 + \lambda}\right)^2 (U_\nu^* y)^2 + \sum_{\nu=n+1}^{m}(U_\nu^* y)^2\right] / \left[\frac{1}{m}\left(\sum_{\nu=1}^{n}\frac{\lambda}{\sigma_\nu^2 + \lambda} + m - n\right)\right]^2 \end{aligned}$$

5.4 Transfer matrix, error and resolution

Formally, the solution (5.9) can be expressed in terms of a matrix equation $\mathbf{x}_\lambda = A_\lambda^+ \mathbf{b}$ where

$$A_\lambda^+ = XF\Sigma^+ U^T, \quad F = \begin{pmatrix} \mathrm{diag}(\varphi_i) & 0 \\ 0 & I_{n-p} \end{pmatrix}, \quad \varphi_i = \frac{\gamma_i^2}{\gamma_i^2 + \lambda^2}. \tag{5.14}$$

Σ^+ is the generalized inverse (Moore-Penrose pseudo-inverse) of the matrix Σ.

$$\Sigma^+ = \begin{pmatrix} \Sigma_p^+ & 0 \\ 0 & I_{n-p} \end{pmatrix}, \quad \Sigma_p^+ = \mathrm{diag}(\sigma_i^{-1}) \tag{5.15}$$

where σ_i^{-1} is taken as 0 if $\sigma_i = 0$, and I_{n-p} is a unit matrix of dimension $(n-p)$.

Given a set of K observations $\mathbf{b}^{(k)} = \mathbf{b} + \Delta\mathbf{b}^{(k)}$ where $\Delta\mathbf{b}^{(k)}$ is the noise in the kth measurement, the covariance matrix of the measurement is defined by

$$\mathrm{cov}(\mathbf{b}) = \sum_{k=1}^{K} \Delta\mathbf{b}^{(k)} \left(\Delta\mathbf{b}^{(k)}\right)^T / (K-1). \tag{5.16}$$

The covariance matrix of the regularized solution is defined in a similar way. Using $\Delta\mathbf{x} = A_\lambda^+ \Delta\mathbf{b}$, gives

$$\mathrm{cov}(\mathbf{x}) = A_\lambda^+ \,\mathrm{cov}(\mathbf{b}) A_\lambda^{+T}. \tag{5.17}$$

If the error $\Delta\mathbf{b}$ is assumed to be uncorrelated and uniform, that is, $\mathrm{cov}(\mathbf{b}) = s_0^2 I$, we have

$$\mathrm{cov}(\mathbf{x}) = s_0^2 XGX^T, \quad G = \begin{pmatrix} \mathrm{diag}(g_i) & 0 \\ 0 & I_{n-p} \end{pmatrix}, \quad g_i = \left(\frac{\sigma_i^{-1}\gamma_i^2}{\gamma_i^2 + \lambda^2}\right)^2. \tag{5.18}$$

The above equation estimates the error of the solution. An optimal choice of λ can to some extent compensate the measurement noise s_0 .

The difference between $\mathbf{x}_\lambda$ and the "true" solution in the observed data, $\mathbf{b} = A\mathbf{x}_{\mathrm{true}}$, then

$$\mathbf{x}_\lambda - \mathbf{x}_{\mathrm{true}} = (A_\lambda^+ A - I)\mathbf{x}_{\mathrm{true}} = (XFX^{-1} - I)\mathbf{x}_{\mathrm{true}}. \tag{5.19}$$

The rows (or columns) of $A_\lambda^+ A$ are peaked at or near the diagonal and have non-negligible sidelobes. The width of the averaging kernel $A_\lambda^+ A$ characterizes the smoothing of the measurement process, i.e., the resolution.

Chapter 6

3D Tomographic Image Reconstruction

6.1 Introduction

Optical tomographic imaging is being developed as a non-invasive and safe imaging modality that employs near-infrared light (typically in the wavelength range 700-1300 nm) to detect breast cancer. It possesses unique advantages over other screening methodologies such as x-ray mammography, ultrasound and magnetic resonance imaging. Both scattering and absorption properties of tumors and the surrounding tissue are accessible and may be used to detect and characterize lesions [30].

In the near-infrared wave-length range, light transport in biological tissues is scattering-dominated. This limits the usability of methods such as back-propagation [10–12] in which a linear model of light attenuation is essential. The iterative tomographic image reconstruction updates its estimation of the optical properties distribution by a Newton-type or a conjugate gradient-type technique through inverting

a so-called Hessian matrix [96]. This method becomes time-prohibitive when the number of voxels increases and is unfit for *in vivo* imaging.

To achieve a 3D tomographic imaging, we have developed several approaches for 3D time-resolved imaging [26, 27]. With use of a point source or a flat expanded source, near real time 3D tomographic image reconstructions using the diffusion approximation have been successfully obtained using simulation and preliminary experiment, for both transmission and backscattering cases. The strategy developed here using the diffusion approximation can be easily extended to use our new cumulant approximation because the replacement does not break the symmetry in the problem.

A general introduction and brief review of algorithms developed for image reconstruction is given in this chapter. The following chapter will discuss in detail the time-resolved Fourier image reconstruction.

6.2 Forward model

The forward model of tomographic image reconstruction for photon migration in a turbid medium can always be written as

$$\mathbf{y}(\lambda) = W(\lambda)\mathbf{x}(\lambda) \tag{6.1}$$

for a NIR source with a wavelength of λ in a linearized image reconstruction framework. Here $\mathbf{y}$ is an array containing the change in measured transmitted photon intensity. $\mathbf{x}$ is an array of the deviation of optical parameters (absorption and/or scattering coefficient), due to existence of the inhomogeneity, which, in practical application, is the difference of the optical parameters between a patient's tissue and

the assumed reference medium. W is the weight function, which, in the linear inversion case, is related only to the reference medium. Characteristic features of the spectrum of the absorption and scattering parameters of different concentrations of metabolic compounds may help to choose an optimal single wavelength to perform the tomographic reconstruction where the inhomogeneity is manifested [97].

For a common slab setup, an ultrafast point light pulse $S(\mathbf{r}_s)\delta(t)$ flashes onto the slab from one side and the detector records the signals on the other side. A good description of the model is the diffusion equation Eq. (2.10), and the main equation governing the inversion procedure up to a first order Born approximation is Eq. (2.26)

$$\begin{aligned}\phi_s(\mathbf{r},t) &= -\int d^3\mathbf{r}'dt'G(\mathbf{r},\mathbf{r}',t-t')\delta\mu_a(\mathbf{r}')c\phi_i(\mathbf{r}',t') \\ &- \int d^3\mathbf{r}'dt'\delta D(\mathbf{r}')c\nabla_{\mathbf{r}'}G(\mathbf{r}-\mathbf{r}',t-t')\cdot\nabla_{\mathbf{r}'}\phi_i(\mathbf{r}',t') \qquad (6.2)\end{aligned}$$

where $\phi_s = \delta I = I - I_0$ is the scattered wave field, and $D = (3\mu_s')^{-1}$. μ_a are the diffusion coefficient and the absorption coefficient, respectively. Here μ_s' is the reduced scattering coefficient of the medium.

To make the discussion simpler, consider the absorption only case with homogeneous D, and regard the hidden object as the perturbation $\Delta\mu_a$ to a uniform background μ_a, then one can solve the diffusion equation and get

$$\begin{aligned}-\frac{\Delta I(\mathbf{r}_d,t)}{I_0(\mathbf{r}_d,t)} &= \int_0^t d\tau\int d^2\mathbf{r}_s\int d^3\mathbf{r}\Delta\mu_a(\mathbf{r})cG(\mathbf{r}_d,\mathbf{r},t-\tau)G(\mathbf{r},\mathrm{r}_s,\tau)S(\mathrm{r}_s) \\ &\quad / \int d^2\mathbf{r}_s G(\mathbf{r}_d,\mathbf{r}_s,t)S(\mathbf{r}_s) \qquad (6.3)\end{aligned}$$

where $\mathbf{r}_d = (x_d, y_d, z_d)$ is the coordinate of a pixel on the detector frame. $\mathbf{r} = (x, y, z)$

is the coordinate in the volume of interest, and $\mathbf{r}_s = (x_s, y_s, z_s)$ is the source location. Assume one has T frames of time-sliced measurement and M pixels on detector screen, and the volume of interest is divided into $N_x \times N_y \times N_z$ voxels. Eq. (6.3) can be transformed into a discrete form

$$Y = WX$$

where the dimension of the weight matrix W is $MT \times N_x N_y N_z$. Hence the inversion involves a matrix of dimension $N_x N_y N_z \times N_x N_y N_z$, which is prohibitive in practice for any reasonable running time and resolution.

6.2.1 ϕ-Fourier transform

Consider an absorption only case with source $S(\mathbf{r}, t) = S\delta(\mathbf{r} - \mathbf{r}_0)\delta(t)$ and $\Delta D = 0$, the relative change in signal from Eq. (6.3) is

$$Y(\mathbf{r}, t) = \frac{-\delta I(\mathbf{r}, t)}{I_0(\mathbf{r}, t)} = \int_0^t d\tau \int d^3\mathbf{r}' \delta\mu_a(\mathbf{r}') cG(\mathbf{r}, \mathbf{r}', t - \tau) G(\mathbf{r}', \mathbf{r}_0, \tau - t_0) / G(\mathbf{r}, \mathbf{r}_0, t) \tag{6.4}$$

Basically, the reconstruction of the absorption coefficients can be solved by matrix inversion using discretization of the above equation. But such a simplistic method is very expensive and prohibitive in practice. We will utilize the cylindrical symmetry of this system and use a ϕ-Fourier transform to speed up this process where ϕ is the azimuthal angle.

Now suppose $\mathbf{r}_0 = 0$, i.e., the source is put at the origin of the cylindrical coordi-

nate system, then Eq (6.4) becomes

$$\begin{aligned} Y(\rho,\phi,z,t) &= \int_0^t d\tau \int \rho' d\rho' d\phi' dz' \delta\mu_a(\rho',\phi',z') c \frac{t}{4\pi Dc(t-\tau)\tau} \\ &\quad \times \exp\left\{ -\frac{\rho^2+\rho'^2-2\rho\rho'\cos(\phi-\phi')}{4Dc(t-\tau)} - \frac{\rho'^2}{4Dc\tau} + \frac{\rho^2}{4Dct} \right\} \\ &\quad \times G_z(z,z',t-\tau) G_z(z',0,\tau)/G_z(z,0,t) \\ &= \int \rho' d\rho' d\phi' dz' \delta\mu_a(\rho',\phi',z') c \int_0^t d\tau w(\rho,\rho',z,z',\phi-\phi',t,\tau) \quad (6.5) \end{aligned}$$

where G_z is a one-dimensional diffusion Green's function. If we let $W(\rho,\rho',z,z',\phi-\phi',t) = \int_0^t d\tau w(\rho,\rho',z,z',\phi-\phi',t,\tau)$, and apply Fourier transform over ϕ, then the above convolution over ϕ becomes:

$$Y_n(\rho,z,t) = \int \rho' d\rho' dz' \delta\mu_{an}(\rho',z') c W_n(\rho,\rho',z,z',t) \quad (6.6)$$

where $-\infty < n < \infty$ is integer and $Y_n(\rho,z,t)$, $\delta\mu_{an}(\rho',z')$ and $W_n(\rho,\rho',z,z',t)$ are the Fourier transforms of $Y(\rho,\phi,z,t)$, $\delta\mu_a(\rho',\phi,z')$ and $W(\rho,\rho',z,z',\phi,t)$ respectively.

Using the equality [98]:

$$\int_0^\pi \exp(x\cos\phi)\cos n\phi d\phi = i^n \pi J_n(-ix) = \pi(-i)^n J_n(ix) = \pi I_n(x). \quad (6.7)$$

we find

$$\begin{aligned} W_n(\rho,\rho',z,z',t) &= \int_0^t d\tau \frac{1}{2\pi} \int_{-\pi}^{\pi} d\phi w(\rho,\rho',z,z',\phi,t,\tau) \exp(-in\phi) \\ &= \int_0^t d\tau \frac{t}{4\pi Dc(t-\tau)\tau} I_n\left(\frac{\rho\rho'}{2Dc(t-\tau)}\right) \\ &\quad \times \exp\left\{ -\frac{\rho^2+\rho'^2}{4Dc(t-\tau)} - \frac{\rho'^2}{4Dc\tau} + \frac{\rho^2}{4Dct} \right\} \end{aligned}$$

$$\times G_z(z,z',t-\tau)G_z(z',0,\tau)/G_z(z,0,t) \tag{6.8}$$

Eq. (6.6) enables us to perform inversion in (ρ, z) space for each n separately. For a full description of this algorithm, please consult Ref. 99.

6.2.2 2D Fourier transform in xy plane

Let us consider the same absorption-only problem as in section (6.2.1) in a Cartesian coordinate system, then Eq (6.2) becomes:

$$\begin{aligned} -\delta I(x,y,z,t) &= \int_0^t d\tau \int dx'dy'dz'\delta\mu_a(x',y',z')cG_{2D}(x-x',y-y',t-\tau) \\ &\quad \times G_{2D}(x',y',\tau)G_z(z,z',t-\tau)G_z(z',0,\tau)S\exp(-\mu_a ct) \end{aligned} \tag{6.9}$$

Applying a Fourier transform over the xy plane, we get:

$$\begin{aligned} -\delta\tilde{I}(k_x,k_y,z,t) &= \int_0^t d\tau \int dk_x'dk_y'dz'\delta\mu_a(k_x',k_y',z')c\tilde{G}_{2D}(k_x,k_y,t-\tau) \\ &\quad \times \tilde{G}_{2D}(k_x-k_x',k_y-k_y',\tau)G_z(z,z',t-\tau)G_z(z',0,\tau)S\exp(-\mu_a ct) \end{aligned} \tag{6.10}$$

where $\tilde{G}_{2D}(k_x,k_y,t) = \exp\left[-4\pi^2 Dct(k_x^2+k_y^2)\right]$.

A useful technique here is to switch from (k_x,k_y) to (k,ϕ) and (k_x',k_y') to (k',ϕ') where (k,ϕ) and (k',ϕ') are polar coordinates, we get:

$$\begin{aligned} -\delta\tilde{I}(k,\phi,z,t) &= \int_0^t d\tau \int k'dk'd\phi'dz'\delta\mu(k',\phi',z')c \\ &\quad \times \exp\left\{-4\pi^2 Dc\left[tk^2+\tau k'^2-2\tau kk'\cos(\phi-\phi')\right]\right\} \\ &\quad \times G_z(z,z',t-\tau)G_z(z',0,\tau)S\exp\left(-\mu_a ct\right) \end{aligned} \tag{6.11}$$

Applying the Fourier transform over ϕ, we have

$$\begin{aligned} -\delta\hat{I}_n(k,z,t) &= \int_0^t d\tau \int k'dk'dz'\delta\mu_n(k',z')c\exp\left[-4\pi^2 Dc(tk^2+\tau k'^2)\right] I_n(8\pi^2 Dc\tau kk') \\ &\quad \times G_z(z,z',t-\tau)G_z(z',0,\tau)S\exp\left(-\mu_a ct\right) \end{aligned} \tag{6.12}$$

The benefit of this formula is that for a measurement with noise level e, the meaningful (n,k) are limited to a few values and hence the reconstruction is simplified. For any function $f(x,y) = f(\rho,\phi)$, its transformed form $\hat{f}$ is found to be

$$\begin{aligned} \hat{f}_n(k) &= \int_0^{+\infty} \rho d\rho \int_{-\pi}^{\pi} d\phi f(\rho,\phi)e^{-in(\phi+\pi/2)}J_n(2\pi k\rho) \\ f(\rho,\phi) &= 2\pi \sum_{n=-\infty}^{+\infty} e^{in(\phi+\pi/2)} \int_0^{+\infty} kdk\hat{f}_n(k)J_n(2\pi k\rho) \end{aligned} \tag{6.13}$$

which is an extension of the famous Fourier-Bessel Transform where $f(\rho,\phi) = f(\rho)$.

Now let's return to the point pulse case. Eqs. (6.10), (6.11) and (6.12) will be approximated by omitting all the spatial frequencies higher than the cutoff frequency K_{cutoff}. Then the matrix involved in the inversion process will be of size $N_z(K_{\text{cutoff}}+1)(2K_{\text{cutoff}}+1)$ instead of $N_xN_yN_z$. The K_{cutoff} can be chosen to be the frequency where $\Delta I(k_x,k_y,z,t)$ levels off.

6.2.3 Fourier time-resolved tomography for plane wave

If the pulse is a distribution $S(x_0,y_0)\delta(t)$ on the $z=0$ plane, then:

$$\begin{aligned} -\delta\tilde{I}(k_x,k_y,z,t) &= \int_0^t d\tau \int dk'_x dk'_y dz' \delta\mu(k'_x,k'_y,z')c\tilde{G}_{2D}(k_x,k_y,t-\tau) \\ &\quad \times \tilde{G}_{2D}(k_x-k'_x,k_y-k'_y,\tau) \end{aligned} \tag{6.14}$$

$$\times \tilde{S}(k_x - k'_x, k_y - k'_y) G_z(z, z', t - \tau) G_z(z', 0, \tau) \exp(-\mu_a c t)$$

where $\tilde{S}(k_x, k_y)$ is the Fourier transform of $S(x_0, y_0)$.

The above results are remarkable since if $\tilde{S}(k_x, k_y) = \tilde{S}\delta(k_x)\delta(k_y)$, i.e., the source is flat on the plane, the equations can be simplified dramatically and yield

$$\begin{aligned} -\delta\tilde{I}(k_x, k_y, z, t) &= \int_0^t d\tau \int dz' \delta\mu(k_x, k_y, z') c\tilde{G}_{2D}(k_x, k_y, t - \tau)\tilde{S} \\ &\quad \times G_z(z, z', t - \tau) G_z(z', 0, \tau) \exp(-\mu_a c t) \end{aligned} \tag{6.15}$$

Note the inversion will be reduced to a series of 1D matrix inversion for each (k_x, k_y) pair. Different (k_x, k_y) components are dis-entangled from each other and the Eq. (6.15) can be solved for $\Delta\mu_{k_x k_y}(z)$ by $N_x N_y$ independent 1D matrix inversion of z direction with dimension N_z. And the object $\Delta\mu(x, y, z)$ is a inverse Fourier transform of $\Delta\mu_{k_x k_y}(z)$ which can be calculated very quickly by fast Fourier transform (FFT).

Since this method separates the 3D inversion problem into a Fourier inversion in the xy direction and a matrix inversion along the z direction, it enables one to understand the inversion process better and to improve the resolution power in the xy direction and the z direction separately. The spatial frequency domain analysis used in xy direction has a great advantage over other methods due to the following observation that the noise may distribute rather uniformly along the whole frequency range while the "real" signal is composed of mainly low frequency components. Then a suitable "cutoff"-like technique in the Fourier space will suppress noise and enhance resolution. And the "cutoff" frequency will give the information of "best possible" resolution one can expect. A starting point is to simplistically cutoff at the point where the spectrum levels off. A soft, rather than hard, cutoff may be found to be

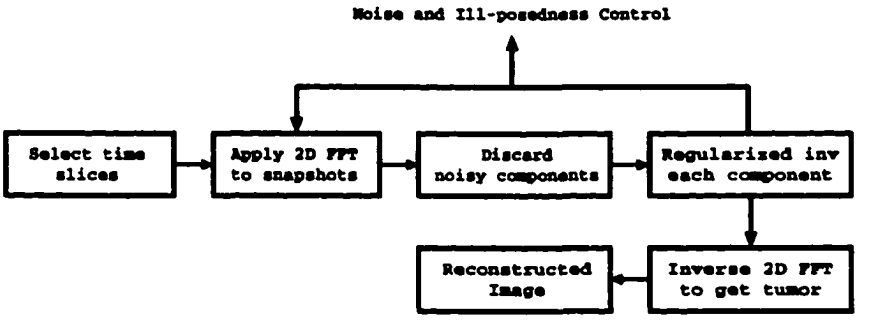

Figure 6.1: A schematic diagram of image reconstruction.

optimal. Some current developments using multiresolution wavelets may be applied here and to get further improvements in resolution and closer access to reconstruction quality. A detailed discussion is provided in Ref. 27 and in the following chapter.

6.3 Inverse problem

A schematic diagram of the image reconstruction procedure is shown in Fig. (6.1). The maximum spatial frequency (cutoff frequency) of the components used in the inversion is determined through a signal-to-noise ratio analysis in which the Fourier components whose magnitude falls below a threshold (comparable to the noise level) are discarded. The threshold is taken to be about two times the noise floor. We have implemented an automatic L-corner finder based on the robust L-curve method [94] to obtain the regularization parameter. Detailed discussions are presented in the following chapter.

6.4 Experiments

Experiments are performed by the ultrafast photonic spectroscopy and imaging group at the Institute for Ultrafast Spectroscopy and Lasers (IUSL). The light source used in the experiments is 150fs in duration, 1kHz repetition-rate pulses of light from a Ti:sapphire laser and amplifier system whose wavelength is tunable between 750 – 850nm. The recording system is the ultrafast electronic gated imaging system (UEGIS). The UEGIS is a compact gated image intensifier unit fiber-optically coupled to a CCD camera (LaVision, Picostar). It provides an electronic time gate pulse whose full-width-at-half-maximum (FWHM) duration could be adjusted to a minimum of approximately 80ps. The gate position could be varied over a 20ns range with a minimum step size 25ps.

In experiments, a suspension of Intralipid-10% (Kabi Pharmacia Inc., Clayton, North Carolina) in water is used as the medium to emulate a human breast tissue. Its transport mean free path is around 1mm at the wavelength of 800nm.

6.5 Useful programs

A few related programs are implemented by me to obtain a) the refractive index of titanium dioxide over a range of wavelength from 0.43μm through 1.53μm, b) the refractive index and the transport mean free path of the intralipid based on Staveren's work [100], and c) the Tikhonov regularized inversion. Listings of these programs can be found in appendix E.

Chapter 7

Time-resolved Fourier optical diffuse tomography

7.1 Introduction

Research on near-infrared (NIR) diffusive light for biomedical imaging and diagnosis has advanced over the past decade because of its potential to be a safe, non-invasive, affordable and superior diagnostics. [3,5,8] To seek a methodology which provides fast data acquisition and reconstruction to perform imaging with high resolution in real time, a variety of techniques have been explored including time resolved picosecond pulses, continuous waves, and diffuse photon density waves (DPDW). Most methods reconstruct three-dimensional optical property maps (OPM) by a matrix inversion or iterative techniques, or by three-dimensional rendering of two dimensional projection images. [9, 13, 14, 26, 101] The difficulty of inverting the whole three-dimensional map at once is usually time prohibitive when the number of volume elements involved increases, while three-dimensional rendering of two dimensional projection images

needs extra depth information of inhomogeneities inside turbid media to behave well and has other limitations [14, 15].

In this chapter, we introduce the theory of propagation of the spatial Fourier component of the scattered wave field inside the turbid medium, and then develop a new optical diffuse imaging methodology based on this theory, using the two-dimensional Fourier transform of photon intensity on a plane to detect inhomogeneities in a highly scattering turbid medium when illuminated by a picosecond (near) plane wave pulse. In such a spatial Fourier space, the picture of photon migration is much simplified, in the sense that different spatial frequency components of the OPM (2D Fourier transform on the xy plane) are decoupled from each other and only depend on the corresponding spatial frequency component of the photon intensity on the detector plane. Based on this observation, we obtain a super-fast reconstruction of 3D OPM by matrix inversions of each spatial component independently. The set of spatial frequency components used in reconstruction is chosen according to the level of noise. After a rigorous account of the theory and a brief description of the algorithm, examples of reconstruction of absorptive and scattering inhomogeneities located up to 2cm below the surface of a human-tissue-like semi-infinite turbid medium using backscattered photons are presented at the end.

7.2 Theory

The propagation of photon density $\phi(\mathbf{r}, t)$ at position $\mathbf{r}$ and time t in a highly scattering turbid medium can be described by the diffusion equation

$$\frac{\partial}{\partial t}\phi(\mathbf{r}, t) - c\nabla \cdot D(\mathbf{r})\nabla\phi(\mathbf{r}, t) + c\mu_a(\mathbf{r})\phi(\mathbf{r}, t) = S(\mathbf{r}, t). \tag{7.1}$$

The absorption coefficient μ_a (per unit length), and the diffusion coefficient $D = 1/(3\mu_s')$ where μ_s' is the reduced scattering coefficient, may depend on the position in the medium. c is the speed of light inside the medium, and S is the source term describing the density of photons generated per second.

For the case of a uniform medium and an incident source $S(\mathbf{r}, t)$ ($S = 0$ when $t < 0$), the incident wave field is $\phi_i(\mathbf{r}, t) = \int d^3\mathbf{r}' \int_0^t dt' S(\mathbf{r}', t') G(\mathbf{r}, \mathbf{r}', t-t')$ where $G(\mathbf{r}, \mathbf{r}', t)$ is the Green's function for the diffusion equation in a uniform turbid medium. When some weak inhomogeneities (objects such as tumors) are embedded in the medium, we write

$$\begin{aligned} \mu_{a,\mathrm{obj}}(\mathbf{r}) &= \mu_a + \delta\mu_a(\mathbf{r}) \\ \mu'_{s,\mathrm{obj}}(\mathbf{r}) &= \mu'_s + \delta\mu'_s(\mathbf{r}) \end{aligned} \tag{7.2}$$

where μ_a and μ_s' are the constant absorption and the reduced scattering coefficients of the otherwise homogeneous medium, $\mu_{a,\mathrm{obj}}(\mathbf{r})$ and $\mu'_{s,\mathrm{obj}}(\mathbf{r})$ are the absorption and the reduced scattering coefficients of the embedded inhomogeneity which are spatially dependent. Plugging Eq. (7.2) into Eq. (7.1), and noting the diffusion parameter of the inhomogeneity $D_{\mathrm{obj}}(\mathbf{r}) = D + \delta D(\mathbf{r}) = 1/(3\mu_s') - \delta\mu_s'(\mathbf{r})/(3\mu_s'^2)$, we have

$$\frac{\partial}{\partial t}\phi(\mathbf{r}, t) - Dc\nabla^2\phi(\mathbf{r}, t) + \mu_a c\phi(\mathbf{r}, t) = S(\mathbf{r}, t) + c\nabla \cdot \delta D(\mathbf{r})\nabla\phi(\mathbf{r}, t) - c\delta\mu_a(\mathbf{r})\phi(\mathbf{r}, t). \tag{7.3}$$

The complete right-hand side of Eq. (7.3) now acts as the source term, of which, $S(\mathbf{r}, t)$ contributes to the unperturbed wave field $\phi_0 = \phi_i(\mathbf{r}, t)$, and the rest contribute to the

scattered wave field,

$$\begin{aligned}\phi_s(\mathbf{r},t) &= \phi(\mathbf{r},t)-\phi_0(\mathbf{r},t)\\ &= \int d^3\mathbf{r}'\int_0^t dt' G(\mathbf{r},\mathbf{r}',t-t')(c\nabla_{\mathbf{r}'}\cdot\delta D(\mathbf{r}')\nabla_{\mathbf{r}'}\phi(\mathbf{r}',t')-c\delta\mu_a(\mathbf{r}')\phi(\mathbf{r}',t'))\\ &= -\int d^3\mathbf{r}'\int_0^t dt' G(\mathbf{r},\mathbf{r}',t-t')\delta\mu_a(\mathbf{r}')c\phi(\mathbf{r}',t')\\ &\quad+\int d^3\mathbf{r}'\int_0^t dt'\frac{\delta\mu_s'(\mathbf{r}')c}{3\mu_s'^2}\nabla_{\mathbf{r}'}G(\mathbf{r},\mathbf{r}',t-t')\cdot\nabla_{\mathbf{r}'}\phi(\mathbf{r}',t') \qquad (7.4)\end{aligned}$$

after integration by parts.

To first order in the variation of optical absorption and reduced scattering coefficients, we can just replace $\phi(\mathbf{r}',t')$ in Eq. (7.4) by ϕ_i, i.e., the total wave field is a superposition of the incident wave field ϕ_i and the singly scattered wave field ϕ_s. This is the well-known Born approximation.

Now consider the configuration of the frequently studied parallel planar geometry (slab or semi-infinite) with its boundaries at $z=0$ and $z=d$ ($d=+\infty$ for semi-infinite geometry). The exact Green function is [21]

$$G(\mathbf{r},\mathbf{r}',t)=\frac{1}{4\pi Dct}\exp(-\frac{|\rho-\rho'|^2}{4Dct}-\mu_a ct)G_z(z,z',t),\quad (t>0) \qquad (7.5)$$

where $\rho=(x,y)$, $\rho'=(x',y')$. $G_z(z,z',t)$ is chosen according to the boundary condition of the parallel planar geometry, and only depends on time t and z-coordinates of the source position $\mathbf{r}$ and the target position $\mathbf{r}'$. Its two dimensional Fourier transform on ρ,

$$\hat{G}(\mathbf{q},z,\rho',z',t) = \int d^2\rho G(\rho,z,\rho',z',t)\exp(-i\mathbf{q}\cdot\rho)$$

$$= \exp(-i\mathbf{q}\cdot\rho' - Dctq^2 - \mu_a ct)G_z(z,z',t)$$
$$= \hat{G}(\mathbf{q},z,z',t')\exp(-i\mathbf{q}\cdot\rho'). \quad (7.6)$$

For simplicity, let's restrict ourselves first to the case of a pure absorptive perturbation ($\delta\mu_a \neq 0$ and $\delta\mu_s' = 0$) and of an incident pulse $S(\mathbf{r},t) = S(\rho)\delta(z-z_s)\delta(t)$. The scattered wave field on a plane $0 < z < d$ is

$$\phi_s(\rho,z,t) = -\int d^3\mathbf{r}'\int d^2\rho''\int_0^t dt' G(\mathbf{r},\mathbf{r}',t-t')\delta\mu_a(\mathbf{r}')cS(\rho'')G(\mathbf{r}',\rho'',z_s,t') \quad (7.7)$$

from Eq. (7.4) after replacing ϕ by ϕ_i. Inside Eq. (7.7), expand the source term $S(\rho'')$, and Green functions $G(\mathbf{r},\mathbf{r}',t-t')$ and $G(\mathbf{r}',\rho'',z_s,t')$ into integrals of their Fourier components, we find

$$\begin{aligned}
\phi_s(\rho,z,t) &= -\frac{1}{(4\pi^2)^3}\int d^2\rho'\int dz'\int d^2\rho''\int_0^t dt' \\
&\quad\times\int d^2\mathbf{q}\hat{G}(\mathbf{q},z,z',t-t')\exp(i\mathbf{q}\cdot(\rho-\rho'))\delta\mu_a(\rho',z')c \\
&\quad\times\int d^2\mathbf{q}''\hat{S}(\mathbf{q}'')\exp(i\mathbf{q}''\cdot\rho'') \\
&\quad\times\int d^2\mathbf{q}'\hat{G}(\mathbf{q}',z',z_s,t')\exp(i\mathbf{q}'\cdot(\rho'-\rho'')) \\
&= -\frac{c}{(4\pi^2)^3}\int d^2\mathbf{q}\int d^2\mathbf{q}'\int d^2\mathbf{q}''\int_0^t dt' \\
&\quad\times\int dz'\exp(i\mathbf{q}\cdot\rho)\hat{G}(\mathbf{q},z,z',t-t')\hat{S}(\mathbf{q}'')\hat{G}(\mathbf{q}',z',z_s,t') \\
&\quad\times\int d^2\rho'\delta\mu_a(\rho',z')\exp(-i\rho'\cdot(\mathbf{q}-\mathbf{q}')) \\
&\quad\times\int d^2\rho''\exp(i\rho''\cdot(\mathbf{q}''-\mathbf{q}')) \\
&= -\frac{c}{(4\pi^2)^2}\int d^2\mathbf{q}\int d^2\mathbf{q}'\int_0^t dt'\int dz'\exp(i\mathbf{q}\cdot\rho)\hat{G}(\mathbf{q},z,z',t-t')
\end{aligned}$$

$$\times\delta\hat{\mu}_a(\mathbf{q}-\mathbf{q}',z')\hat{S}(\mathbf{q}')\hat{G}(\mathbf{q}',z',z_s,t') \tag{7.8}$$

where $\hat{S}(\mathbf{q})=\hat{S}(\mathbf{q},z_s)=\int d^2\rho S(\rho,z_s)\exp(-i\mathbf{q}\cdot\rho)$, $\delta\hat{\mu}_a(\mathbf{q},z)=\int d^2\rho\delta\mu_a(\rho,z)\exp(-i\mathbf{q}\cdot\rho)$ are two-dimensional Fourier transforms of the source on the $z=z_s$ plane, and of the perturbation of absorption coefficient over the $z=z$ plane, respectively. And at last, we recognize the two dimensional Fourier transform of the scattered wave field $\phi_s(\rho,z,t)$ on a plane z for the case of a pure absorptive perturbation

$$\hat{\phi}_s(\mathbf{q},z,t)=-\frac{c}{4\pi^2}\int d^2\mathbf{q}'dz'\delta\hat{\mu}_a(\mathbf{q}-\mathbf{q}',z')\hat{S}(\mathbf{q}',z_s)\int_0^t dt'\hat{G}(\mathbf{q},z,z',t-t')\hat{G}(\mathbf{q}',z',z_s,t'). \tag{7.9}$$

In a similar fashion, for the case of a pure scattering perturbation ($\delta\mu_a=0$ and $\delta\mu_s'\neq 0$), the two-dimensional Fourier transform of the scattered wave field is

$$\begin{aligned}\hat{\phi}_s(\mathbf{q},z,t) &= \frac{c}{12\pi^2\mu_s'^2}\int d^2\mathbf{q}'dz'\delta\hat{\mu}_s'(\mathbf{q}-\mathbf{q}',z')\hat{S}(\mathbf{q}',z_s)\\ &\quad\times\int_0^t dt'\{\mathbf{q}\cdot\mathbf{q}'\hat{G}(\mathbf{q},z,z',t-t')\hat{G}(\mathbf{q}',z',z_s,t')\\ &\quad+\frac{\partial\hat{G}(\mathbf{q},z,z',t-t')}{\partial z'}\frac{\partial\hat{G}(\mathbf{q}',z',z_s,t')}{\partial z'}\}.\end{aligned} \tag{7.10}$$

The general Fourier scattered wave field is the sum of Eq. (7.9) and Eq. (7.10). Denote the convolutions

$$\begin{aligned}w_a(\mathbf{q},\mathbf{q}',z,t;z') &= \int_0^t dt'\hat{G}(\mathbf{q},z,z',t-t')\hat{G}(\mathbf{q}',z',z_s,t')\\ w_s(\mathbf{q},\mathbf{q}',z,t;z') &= \int_0^t dt'\frac{\partial\hat{G}(\mathbf{q},z,z',t-t')}{\partial z'}\frac{\partial\hat{G}(\mathbf{q}',z',z_s,t')}{\partial z'}\end{aligned} \tag{7.11}$$

which are the weight functions involved in the propagation of spatial Fourier compo-

nents of the scattered wave field, we have

$$\begin{aligned}\hat{\phi}_s(\mathbf{q},z,t) &= -\frac{c}{4\pi^2}\int d^2\mathbf{q}'dz'\delta\hat{\mu}_a(\mathbf{q}-\mathbf{q}',z')\hat{S}(\mathbf{q}',z_s)w_a(\mathbf{q},\mathbf{q}',z,t;z') \\ &\quad +\frac{c}{12\pi^2\mu_s'^2}\int d^2\mathbf{q}'dz'\delta\hat{\mu}_s'(\mathbf{q}-\mathbf{q}',z')\hat{S}(\mathbf{q}',z_s) \\ &\quad \times\{\mathbf{q}\cdot\mathbf{q}'w_a(\mathbf{q},\mathbf{q}',z,t;z')+w_s(\mathbf{q},\mathbf{q}',z,t;z')\}. \qquad (7.12)\end{aligned}$$

Eq. (7.11) summarizes the properties of the background medium. Eq. (7.12) provides the relation between the scattered wavefield (measurement) and the distribution of hidden objects $\delta\hat{\mu}_s'$, $\delta\hat{\mu}_a$. The distribution of hidden objects is inverted from the scattered wavefield.

For the simple case when the incident wave is a plane wave pulse (see Appendix for justification), i.e., $S(\mathbf{r},t)=S\delta(z-z_s)\delta(t)$ where S is a constant, such that $\hat{S}(\mathbf{q},z_s)=4\pi^2S\delta(\mathbf{q})$, Eq. (7.12) simplifies to:

$$\hat{\phi}_s(\mathbf{q},z,t)=-Sc\int dz'\{\delta\hat{\mu}_a(\mathbf{q},z')w_a(\mathbf{q},0,z,t;z')-\frac{\delta\hat{\mu}_s'(\mathbf{q},z')}{3\mu_s'^2}w_s(\mathbf{q},0,z,t;z')\}. \quad (7.13)$$

The salient feature of the above result Eq. (7.13) is that different spatial frequency components of $\delta\hat{\mu}_a$ and $\delta\hat{\mu}_s'$ are decoupled from each other and the $\mathbf{q}$-component of the optical parameters depends only on the the corresponding spatial frequency component of the scattered wave field $\hat{\phi}_s(\mathbf{q},z,t)$. Thus the dimension of the inverse problem to be solved later is greatly reduced, as is the computation time.

Let's approximate the integration over z' by a summation, and fix $z=z_d$ at the detection plane (omit z hereafter), the Fourier scattered wave field on the detection

plane

$$\hat{\phi}_s(\mathbf{q},t) = Sc\Delta z \sum_{j=1}^{N_z}[-\delta\hat{\mu}_a(\mathbf{q},z_j)w_a(\mathbf{q},0,t;z_j) + \frac{\delta\hat{\mu}_s'(\mathbf{q},z_j)}{3\mu_s'^2}w_s(\mathbf{q},0,t;z_j)] \quad (7.14)$$

where Δz is the discretized step size, N_z is the total number of slices (layers) in the z direction between the source plane and detection plane, and z_j is the z-coordinate of the central position of layer j.

Set $\mathbf{q} = 0$ in Eq. (7.14),

$$\hat{\phi}_s(0,t) = Sc\Delta z \sum_{j=1}^{N_z}[-\delta\hat{\mu}_a(0,z_j)w_a(0,0,t;z_j) + \frac{\delta\hat{\mu}_s'(0,z_j)}{3\mu_s'^2}w_s(0,0,t;z_j)]. \quad (7.15)$$

the zero spatial frequency components $\delta\hat{\mu}_a(0,z_j)$ and $\delta\hat{\mu}_s'(0,z_j)$ can be readily solved without doing a complete reconstruction. Due to the nature of Fourier transform, they just provide the profile of the amount of total perturbation of absorption and reduced scattering coefficients per slice, i.e., the depth profile of the inhomogeneities.

The whole three-dimensional absorption and reduced scattering coefficients map is thus constructed through an inverse Fourier transform from all the $\mathbf{q}$-components of $\delta\hat{\mu}_a$ and $\delta\hat{\mu}_s'$ at different depths, each of which is solved independently from a series of time resolved scattered wave field $\hat{\phi}_s$ by Eq. (7.14).

A schematic diagram of the procedure of image reconstruction is shown in Fig. (7.1). The maximum spatial frequency (cutoff frequency) of the components used in the inversion is determined through a signal-noise-ratio analysis in which the Fourier components whose magnitude falls below a threshold (comparable to the noise level) are discarded. The regularization parameter in the matrix inversion is obtained by

the robust L-curve method. [94] The L-corner finder which locates the corner by maximum curvature [53] is implemented and used to obtain the regularization parameter. Neither visual estimate nor prior information is required for this procedure. L-curves are different for each spatial frequency $\mathbf{q}$. The regularization parameter is determined from the reconstruction of the depth profile (where an inversion for $\mathbf{q} = 0$ is performed). The same value is then used in the full 3D reconstruction (layer reconstructions, where inversion includes $\mathbf{q} \neq 0$).

Both transmission and/or backscattering image reconstruction configurations can easily be made using Eqs. (7.13) and (7.14).

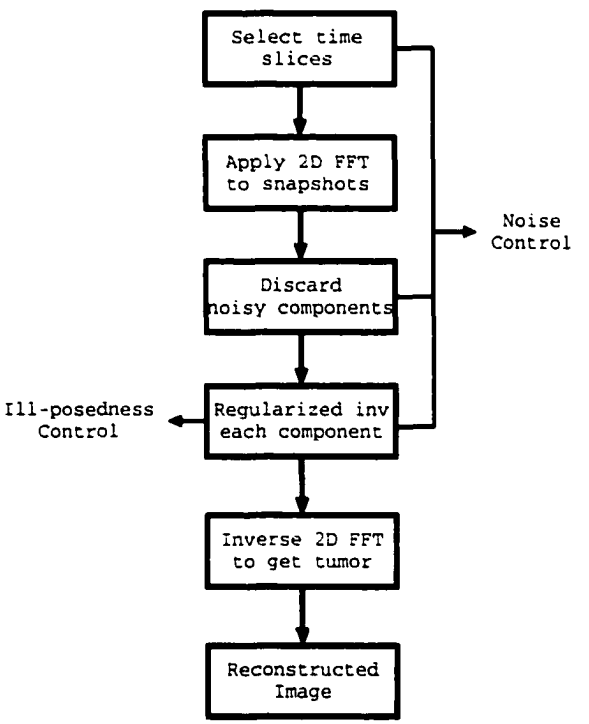

Figure 7.1: A schematic diagram of image reconstruction.

7.3 Simulation

For demonstration purposes, consider a semi-infinite turbid medium ($z < 0$) with its surface at $z = 0$ [Fig. (7.2)], whose absorption coefficient $\mu_a = 0.0033\text{mm}^{-1}$ and reduced scattering coefficient $\mu_s' = 1.0\text{mm}^{-1}$.

7.3.1 Absorptive inhomogeneity

Four absorbing objects A, B, C and D, each 6.25mm × 6.25mm × 3mm and with absorption coefficient $\mu_{a,\text{obj}} = 0.02\text{mm}^{-1}$ and reduced scattering coefficient equal to that of the background, are placed at depth 7.5mm, 7.5mm, 19.5mm and 19.5mm below the surface, and their xy coordinates are $(-25, -18.75)$mm, $(-12.5, -3.1)$mm, $(9.4, 15.6)$mm and $(9.4, 6.25)$mm, respectively. The medium is illuminated by an incident pulse of a Gaussian shape of $\exp(-\rho^2/2\sigma^2)$ with $\sigma = 50$mm inside an aperture of radius 50mm, propagating along the negative z-axis at time $t = 0$.

These parameters are potentially applicable to optical mammography of the compressed-breast-toward-chest using backscattered photons. A series of measurements (total $N_t = 15$ snapshots from 300ps to 2400ps) of an area 100mm × 100mm on the surface plane $z = 0$ are computed by using the direct calculation for the Gaussian pulse in $\mathbf{r}$ space. The simulated data are used as input for inversion after adding a 1%, 5% or 10% Gaussian noise.

In the reconstruction part, the near-surface region of the turbid medium of depth up to 3cm is sliced into $N_z = 10$ layers, i.e., $\Delta z = 0.3$cm, and objects A and B are then located on layer 3, C and D on layer 7. The detection plane of an area of $10 \times 10\text{cm}^2$ is divided uniformly into a $N_x N_y = 32 \times 32$ grid. Objects A, B, C and D all take 2×2 elements by this grid. The results of reconstruction are shown below.

Depth profile

The absorption depth profile, the total absorption perturbation per layer $\int d^2\rho\delta\mu_a(\rho, z)$ vs depth z is shown in Fig. (7.3) with different noise levels for cases (a) 1% noise, (b) 5% noise and (c) 10% noise. In (a), there is one peak at depth $z = 0.75$cm (layer 3) where objects A and B are embedded, and another peak at $z = 1.95$cm (layer 7) where objects C and D are embedded. The width of the first peak at half height is 0.34cm, about the thickness of one layer (0.3cm), which means the depth of objects A and B is resolved very well. The second peak of objects C and D spans two and a half layers with its width of peak at half height 0.74cm, but its peak position is still correct.

When the level of noise increases, the peak values of both peaks decrease, and the half widths increase. The effect of noise on the second peak at $z = 1.95$cm is much more significant than that on the first one at $z = 0.75$cm.

Layer reconstruction

The full 3D OPM is reconstructed. The reconstructed absorption coefficients of the layers at the two peak positions are shown in Fig. (7.4), Fig. (7.5) and Fig. (7.6) for the three noise levels respectively. Fig. (7.4) shows objects A and B are clearly resolved as two objects centered at their original positions with negligible expansion; and objects C and D at depth $z = 1.95$cm are also detected at the correct central positions, but the resolved images are expanded on the xy plane. With the increase of noise level, the shape of objects A and B blurs from Figs. (7.4a) to (7.5a) and (7.6a), and the blur is even worse for objects C and D under the same condition (from Figs. (7.4b) to (7.5b) and (7.6b)).

At the noise level of 1%, the reconstructed absorption parameter for objects A and B is 0.0071mm^{-1} at noise level 1%, about 36% of the original value 0.02mm^{-1} of the absorptive inhomogeneity. In other words, the objects appears larger in space with a weakened absorption parameter. As the noise level increases, the effect is accentuated with a further reduction in the resolved absorption parameter.

7.3.2 Scattering inhomogeneity

For another example, four scattering objects E, F, G and H, each 6.25mm × 6.25mm × 3mm and with reduced scattering coefficient $\mu'_{s,\text{obj}} = 0.5\text{mm}^{-1}$ and absorption coefficient equal to that of the background, are placed at depth 7.5mm, 7.5mm, 13.5mm and 13.5mm below the surface, and their xy coordinates are $(-25, -18.75)$mm, $(-12.5, -3.1)$mm, $(9.4, 15.6)$mm and $(9.4, 6.25)$mm, respectively. The objects E and F are now located on layer 3, and G and H on layer 5. The same source and the inversion procedure in the previous example are used here. The results of reconstruction are shown below.

Depth profile

The scattering depth profile is shown in Fig. (7.7) with different noise levels for cases (a) 1% noise, (b) 5% noise and (c) 10% noise. Two peaks are correctly revealed with the first at depth $z = 0.75$cm (layer 3) and another at $z = 1.35$cm (layer 5) where objects E and F, G and H are embedded respectively. In (a), the width of the first peak at half height is 0.3cm, and that of the second peak is 0.42cm. Thus the depth of these objects are resolved quite well.

With the increase of the noise level, we observe the same behavior of decreasing

quality of depth resolution as in the absorptive case.

Layer reconstruction

The reconstructed scattering coefficients of the layers at the two peak positions (layer 3 and layer 5) are shown in Fig. (7.8), Fig. (7.9) and Fig. (7.10) for the three noise levels respectively.

We observe a similar result as for the case of absorptive case. Objects E and F are better resolved than objects G and H which are deeper into the turbid medium, and the noise has more adverse effect on objects G and H than on objects E and F. The reconstructed reduced scattering coefficient of objects E and F is 0.27mm^{-1}, about 54% of the original value of the embedded scattering inhomogeneity, at the noise level of 1%.

7.4 Discussion

A fast time-resolved Fourier optical diffuse tomography based on decoupled propagation of spatial Fourier components of the scattered wave field when illuminated by a plane wave is presented. For a wave not strictly plain but whose zero-frequency component dominates, this approximation is still valid as long as the radial dimension of the volume where inhomogeneities exist are much smaller than the effective-width of the Gaussian beam (see Appendix).

The image reconstruction method provided is efficient. The optical parameters at $N_x N_y N_z$ different voxels are reconstructed from a set of N_t measurements by N_k^2 times of inversions of $N_z \times N_z$ matrices where $N_k^2 < N_x N_y$ is the total number of Fourier components with the noisy ones discarded. Our procedure is much more efficient

compared to a direct reconstruction where an inversion of $N_xN_yN_z \times N_xN_yN_z$ matrix is involved. The speedup is about $O(N_xN_y)$ times faster. The time this algorithm takes to perform a complete 3D reconstruction in the above examples (of $32 \times 32 \times 10$ volume elements) is less than half a minute using a scripting language Python on one 180Mhz CPU of Origin 200 computer from Silicon Graphic Inc. This algorithm scales only linearly with the number of elements in the xy grid, so it can be used to handle much larger data sets in real time with little difficulty.

This approach does not limit the number or the thickness of the inhomogeneities. It allows multiple inhomogeneities and one inhomogeneity may span several layers.

With little effort, a depth profile (the sum of the perturbation of optical parameter vs depth) of the inhomogeneities inside a highly scattering turbid medium can be obtained. This information itself may be very useful in some cases. When the inhomogeneity is found to exist only in one layer from the depth profile, the summation in Eq. (7.14) no longer exists. A direct inverse Fourier transform can thus be used to resolve the inhomogeneity when it is a sole absorptive or scattering perturbation.

7.5 Appendix

Eq. (7.12) is the exact formula to calculate the scattered wave field. For a pulse $S(\mathbf{r}, t) = S(\rho)\delta(z - z_s)\delta(t)$ with Gaussian shape $S(\rho) = S_0 \exp(-\rho^2/2\sigma^2)$, we have $\hat{S}(\mathbf{q}) = 2\pi\sigma^2 S_0 \exp(-\sigma^2 q^2/2)$, and the first term of Eq. (7.12):

$$\begin{aligned} A &= -\frac{\sigma^2 S_0 c}{2\pi} \int d^2\mathbf{q}' dz' \delta\hat{\mu}_a(\mathbf{q} - \mathbf{q}', z') \exp(-\sigma^2 q'^2/2) w_a(\mathbf{q}, \mathbf{q}', z, t; z') \\ &= -\frac{\sigma^2 S_0 c}{2\pi} \int d^2\mathbf{q}' dz' d^2\rho' \delta\mu_a(\rho', z') \exp(-i(\mathbf{q} - \mathbf{q}') \cdot \rho' - \sigma^2 q'^2/2) w_a(\mathbf{q}, \mathbf{q}', z, t; z') \end{aligned}$$

$$= -\frac{\sigma^2 S_0 c}{2\pi} \int d^2\rho' dz' \delta\mu_a(\rho', z') \exp(-i\mathbf{q}\cdot\rho') \int_0^t dt' \hat{G}(\mathbf{q}, z, z', t-t') G_z(z', z_s, t')$$
$$\times \exp(-\mu_a c t') \int d^2\mathbf{q}' \exp(-\sigma^2 q'^2/2 - Dct' q'^2 + i\mathbf{q}'\cdot\rho') \quad (7.16)$$

after plugging in Eq. (7.11) and Eq. (7.6).

The last integral of Eq. (7.16) can be performed exactly and turns out to be $\pi R^{-2} \exp(-4\rho'^2/R^2)$ where the effective width

$$R^2 = \sigma^2/2 + Dct' > \sigma^2/2. \quad (7.17)$$

When the inhomogeneities exist inside a region of radial dimension L around the origin of xy coordinate system satisfying $L \ll R$, we can approximate $\exp(-4\rho'^2/R^2)$ by 1 which is equivalent to letting $\mathbf{q}' \to 0$, the case of an incident plane wave Eq. (7.13). The error made by such an approximation is of a second order in L/R.

The same analysis can be applied to the second term of Eq. (7.12).

Thus our plane wave approximation can be justified for inhomogeneities whose radial distance from the origin L is much smaller than the effective width R of the beam.

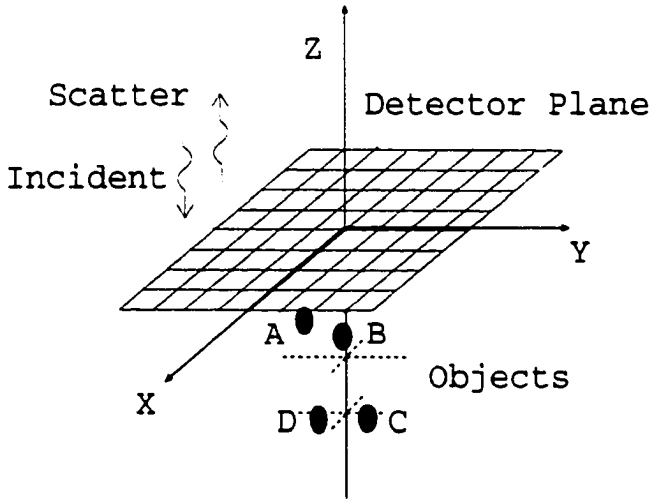

Figure 7.2: The geometry for time-resolved Fourier optical diffuse tomography using backscattered photons. The source is a picosecond (near) plane wave pulse, and a series of snapshots of a 10 × 10cm^2 area on the surface are computed as the input to image reconstruction. The absorptive objects A (−2.5, −1.875, −0.75)cm, B (−1.25, −0.31, −0.75)cm, C (0.94, 1.56, −1.95)cm and D (0.94, −0.625, −1.95)cm, or scattering objects E (−2.5, −1.875, −0.75)cm, F (−1.25, −0.31, −0.75)cm, G(0.94, 1.56, −1.35)cm and H (0.94, −0.625, −1.35)cm are used in the simulation.

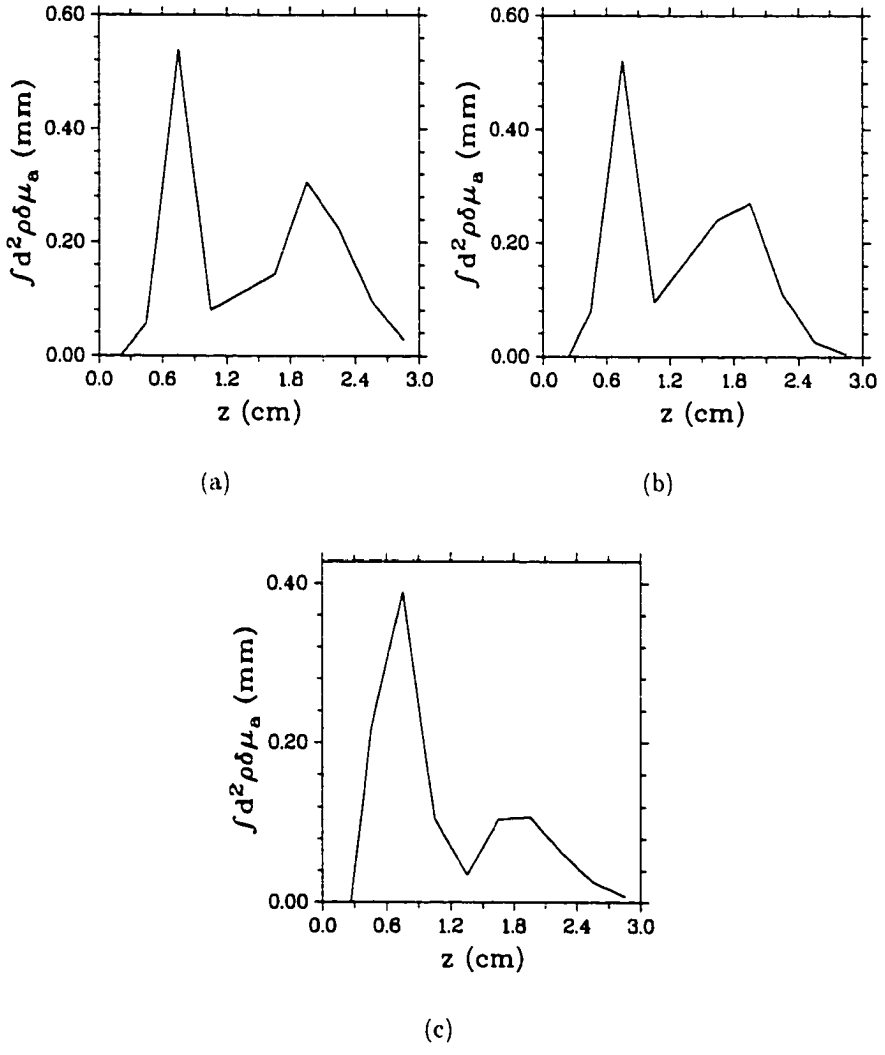

Figure 7.3: The absorption depth profile for (a) with 1% noise, (b) 5% noise, and (c) 10% noise.

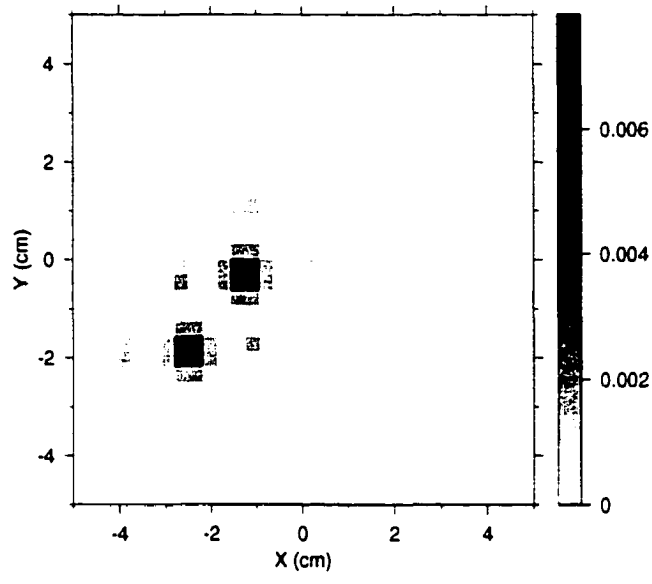

(a)

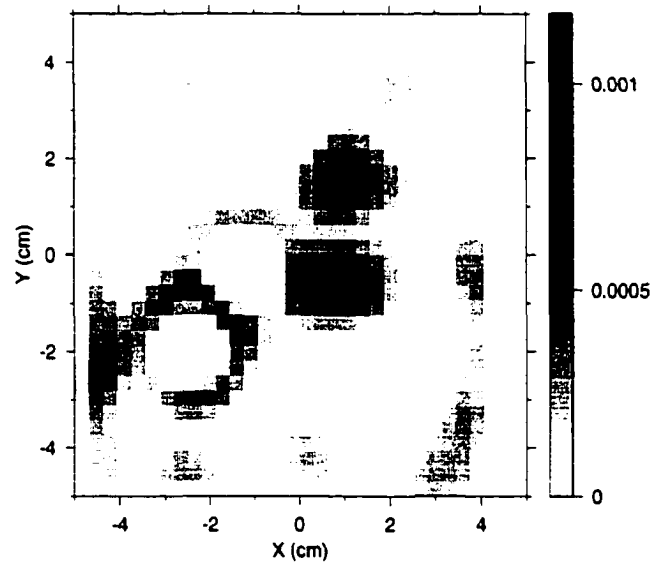

(b)

Figure 7.4: Layer reconstruction at a noise level of 1%: (a) resolved objects A (left) and B (right) at $z = 0.75$cm (layer 3), and (b) resolved objects C (upper) and D (lower) at $z = 1.95$cm (layer 7). The darkness of the pixel represents the resolved absorption coefficient in the unit of mm^{-1}.

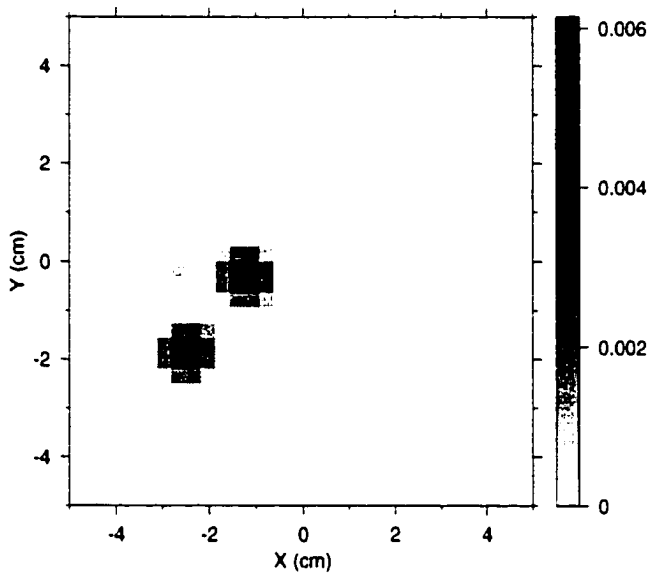

(a)

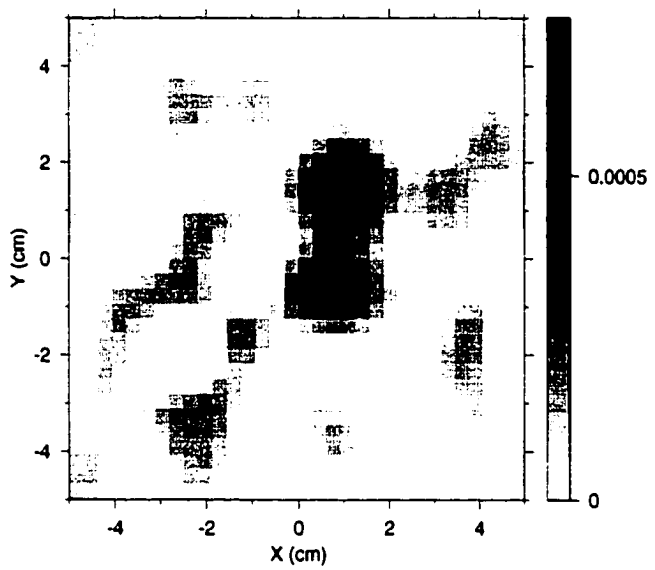

(b)

Figure 7.5: Layer reconstruction at a noise level of 5%: (a) resolved objects A (left) and B (right) at $z = 0.75$cm (layer 3), and (b) resolved objects C (upper) and D (lower) at $z = 1.95$cm (layer 7). The darkness of the pixel represents the resolved absorption coefficient in the unit of mm^{-1}.

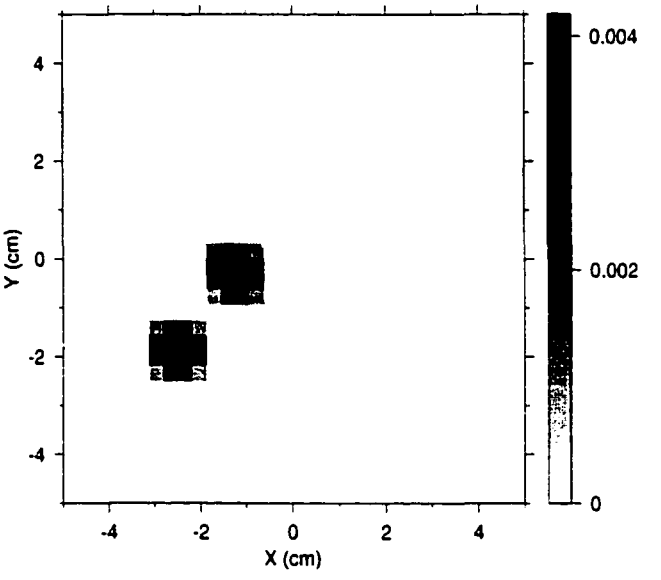

(a)

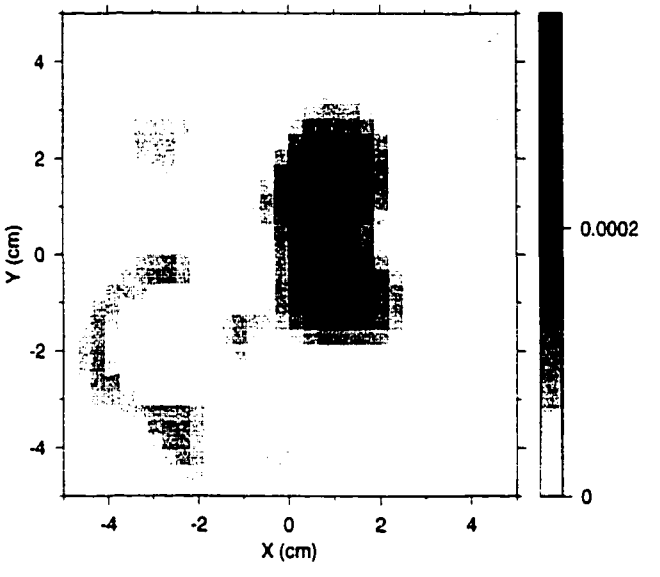

(b)

Figure 7.6: Layer reconstruction at a noise level of 10%: (a) resolved objects A (left) and B (right) at $z = 0.75$cm (layer 3), and (b) resolved objects C (upper) and D (lower) at $z = 1.95$cm (layer 7). The darkness of the pixel represents the resolved absorption coefficient in the unit of mm^{-1}.

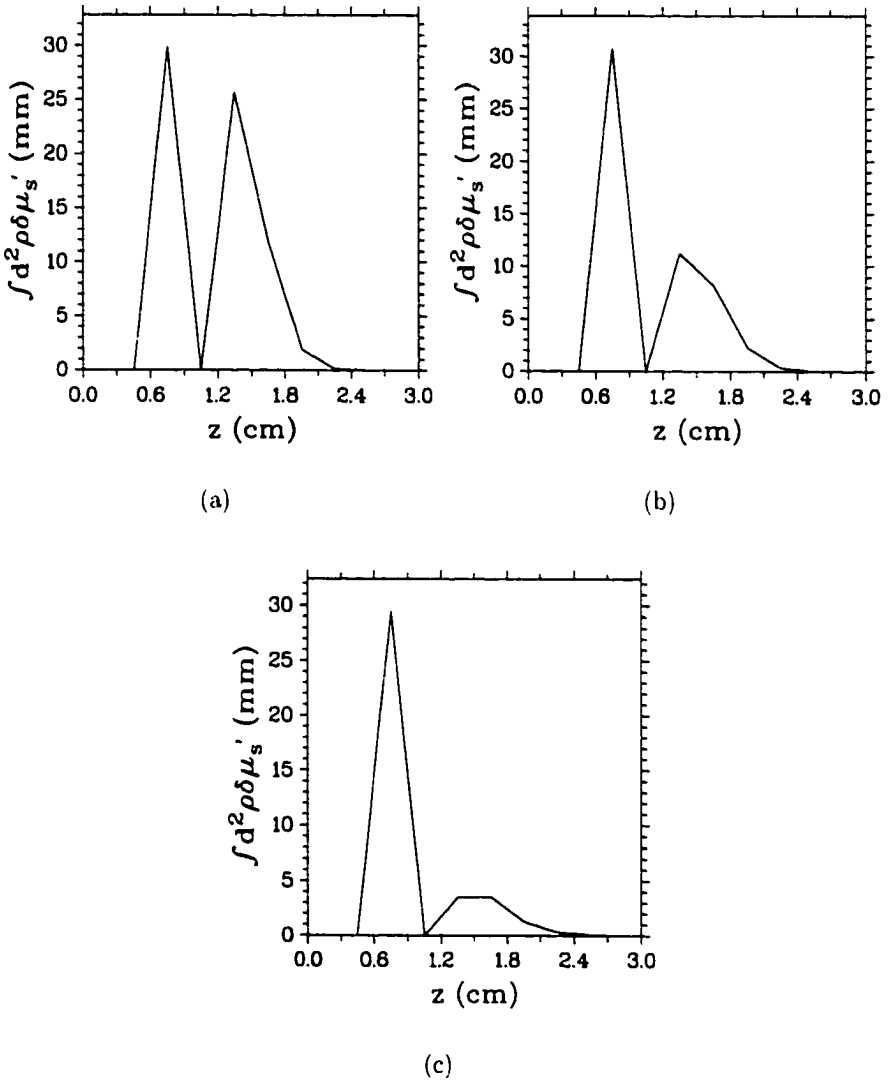

Figure 7.7: The scattering depth profile for (a) with 1% noise, (b) 5% noise, and (c) 10% noise.

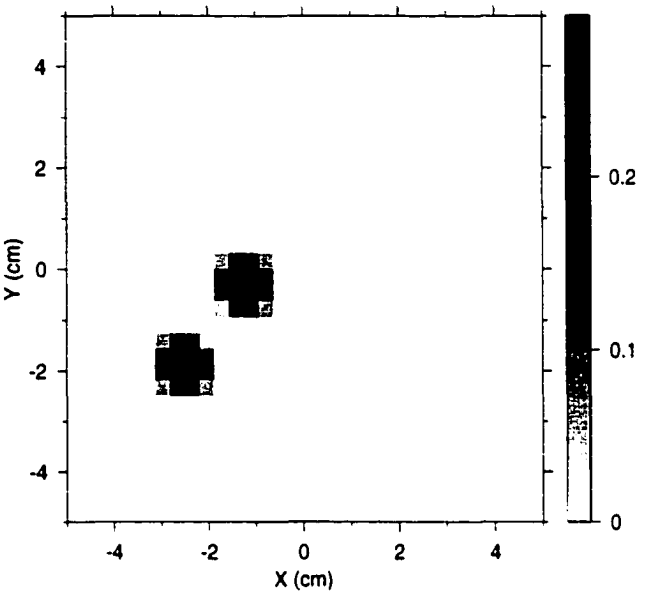

(a)

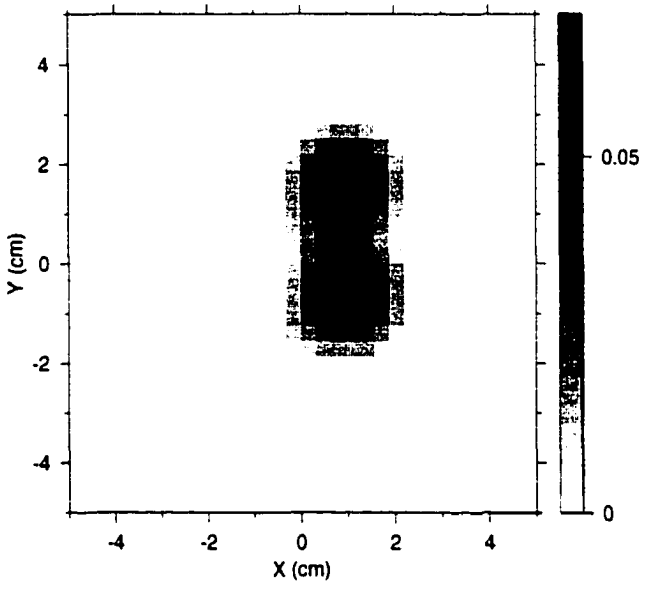

(b)

Figure 7.8: Layer reconstruction at a noise level of 1%: (a) resolved objects E (left) and F (right) at $z = 0.75$cm (layer 3), and (b) resolved objects G (upper) and H (lower) at $z = 1.35$cm (layer 5). The darkness of the pixel represents the resolved reduced scattering coefficient in the unit of mm^{-1}.

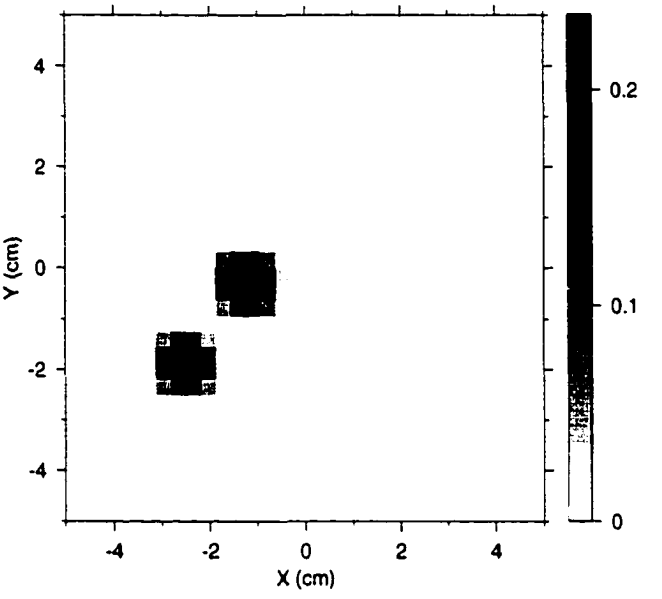

(a)

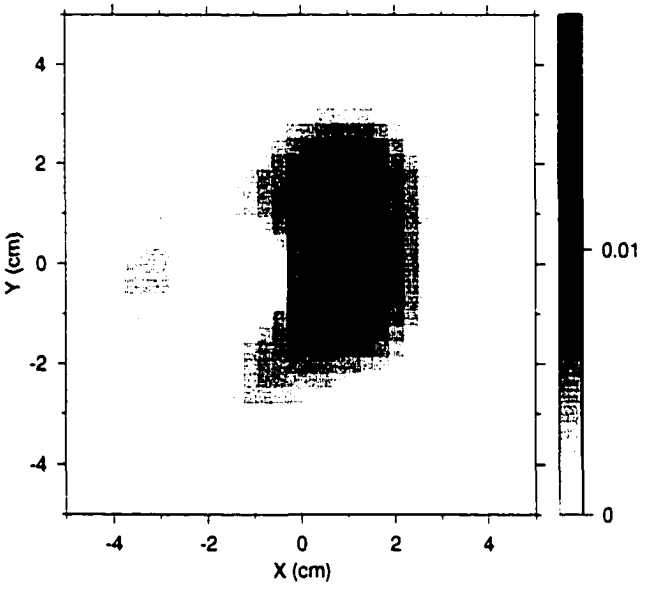

(b)

Figure 7.9: Layer reconstruction at a noise level of 5%: (a) resolved objects E (left) and F (right) at z = 0.75cm (layer 3), and (b) resolved objects G (upper) and H (lower) at z = 1.35cm (layer 5). The darkness of the pixel represents the resolved reduced scattering coefficient in the unit of mm^{-1}.

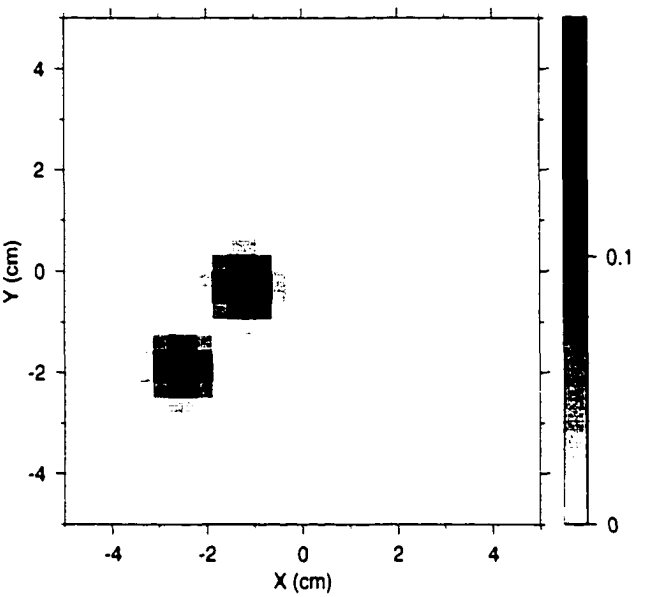

(a)

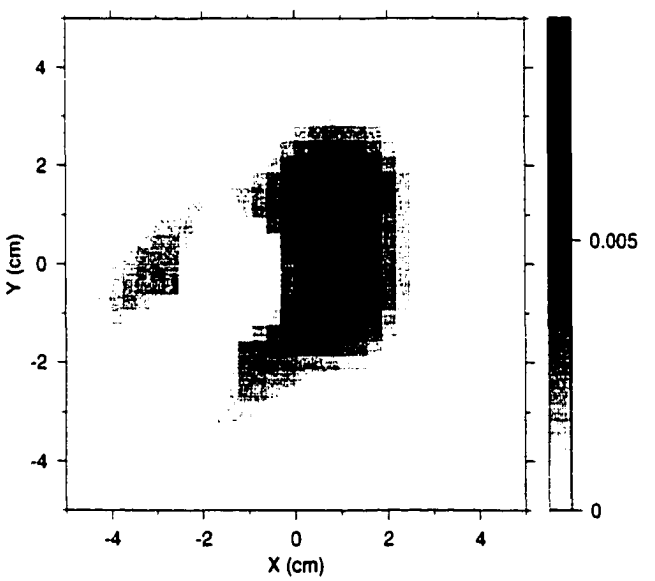

(b)

Figure 7.10: Layer reconstruction at a noise level of 10%: (a) resolved objects E (left) and F (right) at $z = 0.75$cm (layer 3), and (b) resolved objects G (upper) and H (lower) at $z = 1.35$cm (layer 5). The darkness of the pixel represents the resolved reduced scattering coefficient in the unit of mm^{-1}.

Chapter 8

Summary and Outlook

8.1 Summary

Image reconstruction in turbid media has a vast number of applications across different fields from remote sensing to biomedical diagnostics. This thesis specialized in the topic of image reconstruction in highly scattering media using optical methods, especially optical mammography. Optical mammography is being actively developed as a non-invasive and safe imaging modality. It possesses unique advantages over other methodologies because it is able to map the characterization of lesions by accessing both scattering and absorption properties of tumors and the surrounding tissue at different wavelengths in the near infrared range.

The assessment of the scattering and absorption properties of breast tissue is usually obtained by assuming the diffusion approximation. This approximation introduces errors from scattering close to the light source or the detector. We discussed a novel transport forward model for photon migration in turbid media based on radiative transfer which describes both the ballistic and snake photons at early times

and diffusive photons at later times. This transport model was compared with Monte Carlo simulations and its superiority over the diffusion approximation was manifested. The weight function for image reconstruction under this new model was shown to have a strong dependence at both early and later times on absorption and/or scattering inhomogeneities located in the propagation direction of and close to the source, or in the field of view of and close to the detector. This effect originates from the initial ballistic motion of incident photons, which is substantially underestimated by the diffusion approximation.

In the second part, we discussed the techniques involved in the regularized inversion and then presented a family of three-dimensional time-resolved image reconstruction methods. With use of a point source or a flat expanded source, near real-time 3D tomographic image reconstructions using the diffusion approximation have been successfully obtained using simulation and preliminary experiment, for both transmission and backscattering cases. We achieved a tremendous speed up compared with a direct matrix inversion by exploiting the symmetry presented in the problem and using fast Fourier transforms. The regularization parameter of the inversion is determined through a robust L-curve method that avoids arbitrariness.

8.2 Outlook

Image reconstruction in turbid media is a science and also an art.

With use of the more accurate forward model provided by the cumulant approximation to radiative transfer, some deficiencies of the diffusion approximation can be overcome:

- both diffusive photons and photons traveling comparatively short trajectories (limited by the signal-to-noise ratio) can be used to reconstruct an image
- the modeling error from the contribution to light intensity from inhomogeneity at regions near the source or detector, introduced by the diffusion approximation, will be overcome

Strong light scattering is the main factor which limits the spatial resolution obtainable through optical mammography. The use of a transport model rather than a diffusion approximation in the tomographic imaging will improve the contrast and resolution of optical mammography because of both a more accurate forward model and the inclusion of early light which experiences much less scattering. Our strategy developed in a semi-real time three-dimensional image reconstruction of optical properties using the diffusion approximation by using Fourier techniques can be extended to use this new forward model because the replacement does not break the symmetry in the problem.

The amount of improvement of inversion quality with use of the transport forward model rather than the diffusion approximation depends on other factors than just the accuracy of the forward model. Three elements, i.e., the forward model, the prior information and the noise must be all addressed to improve the quality of reconstruction.

For image reconstruction of a slab of a turbid medium with a thickness of twenty transport mean free path or larger, the mere improvement on the forward model (replacing the diffusion approximation by our new transport forward model) will not yield an appreciable improvement in the quality of reconstruction because that, a) the diffusion approximation is not bad for the slab of that thickness; b) the modeling

error, that the diffusion approximation fails to provide a correct weight function for an inhomogeneity located close to the source or the detector, can be compensated to an extent by a suitable choice of regularization parameters in the inverse algorithm with help of the prior information.

Thus to take full advantage of the new transport forward model, it is important to utilize measurements from earlier time which are not well modeled and may not have been usable in the diffusion approximation previously. The signal to noise ratio for these earlier time data, however, is low because the noise is proportional to the square root of the photon counts in the shot noise limit. The noise is intensity dependent and not white. Hence it is essential that reconstruction algorithms should take into account the fact that the noise is intensity dependent and Poisson in the shot-noise limit in order to take full advantage of our improved forward model.

Research on tomography with explicit modeling of Poisson noise is warranted. One approach to model the noise explicitly in the inverse problem is to regard the measurement as a random process and enhance the Tikhonov regularization procedure accordingly, which is currently under investigation.

Finally with help of tissue spectroscopy, an optimal single wavelength or multiple wavelengths to perform the tomographic reconstruction may be identified. For example, two nearby wavelengths λ and $\lambda+\Delta\lambda$ may be identified and the difference between measured intensities at the two wavelengths, $\mathbf{y}(\lambda) - \mathbf{y}(\lambda + \Delta\lambda)$, may cancel out most of the scattering contribution such that the reconstruction involves only absorption inhomogeneities because the change of scattering coefficient at nearby wavelengths is negligible. Furthermore, the difference between measured intensities at two nearby wavelengths in a backscattered configuration will be more sensitive to deeper regions

and yields a better reconstruction of that region because the contribution due to inhomogeneities near surface tends to cancel each other.

Appendix A

Abbreviations

3D three-dimensional

CA cumulant approximation

DA diffusion approximation

DPDW diffuse photon density waves

FFT fast Fourier transform

FWHM full-width-at-half-maximum

IUSL the Institute for Ultrafast Spectroscopy and Lasers

MC Monte Carlo

NIR near-infrared

OPM optical parameter map

Appendix B

Green's Function Associated with Source

A fast evaluation of the Green's function associated with source $G^{S}(\mathbf{r}, t)$ is very important in developing the image reconstruction algorithms. We list here the results for sources of a Gaussian or elliptic shape.

For a Gaussian shape source:

$$f(\rho) = \begin{cases} N^{-1}\exp(-\rho^2/2\sigma^2), & \text{for } \rho \leq R \\ 0, & \text{for } \rho > R \end{cases} \tag{B.1}$$

where N is a normalization factor and $N = 2\pi\sigma^2(1-\exp(-R^2/2\sigma^2))$[Fig. (B.1)], we have,

$$\begin{aligned} G^{S}_{2D}(\rho, t) &= \frac{R^2}{16\pi Dct\sigma^2(1-\exp(-R^2/2\sigma^2))} \\ &\times \int_{-1}^{1} dx \exp(-\frac{\rho^2}{4Dct} - \frac{(\sigma^2+2Dct)(x+1)R^2}{8Dct\sigma^2}) \mathrm{I}_0(\frac{\rho R\sqrt{x+1}}{2\sqrt{2}Dct}) \end{aligned} \tag{B.2}$$

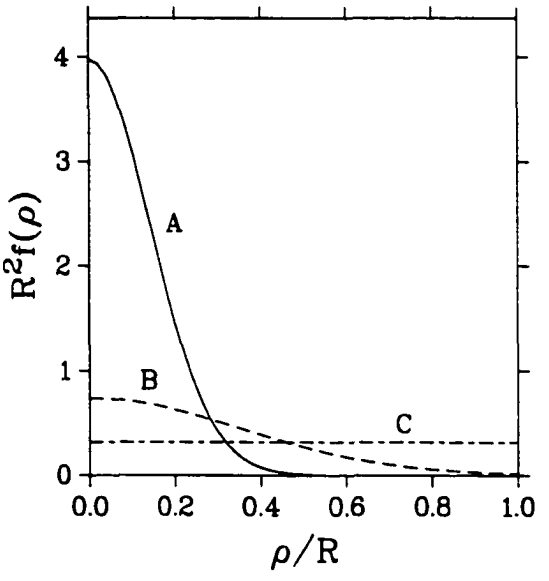

Figure B.1: Gaussian shape sources with $\sigma/R = 0.2$ (A), 0.5 (B) and 10 (C).

which can be calculated using adaptive numerical quadrature methods. At the plane wave limit, $\sigma \gg \sqrt{Dct}, R$, Eq. (B.2) yields

$$G^{S}_{2D,\text{plane}}(\rho,t) = \frac{1}{8\pi Dct}\int_{-1}^{1} dx \exp(-\frac{\rho^2}{4Dct} - \frac{(x+1)R^2}{8Dct})\mathrm{I}_0(\frac{\rho R\sqrt{x+1}}{2\sqrt{2}Dct}) \simeq \frac{1}{\pi R^2}. \tag{B.3}$$

At the point source limit, $\sigma \ll R$,

$$G^{\mathrm{S}}_{2D,\text{point}}(\rho,t) = \frac{1}{2\pi(2Dct+\sigma^2)}\exp(-\frac{\rho^2}{4Dct})\int_0^{\infty} dx \exp(-x)\mathrm{I}_0(\frac{\rho\sigma x}{\sqrt{Dct(2Dct+\sigma^2)}}) \tag{B.4}$$

from Eq. (2.22).

For an elliptic shape of source:

$$f(\rho) = \begin{cases} (N_xN_y)^{-1}\exp(-x^2/2\sigma_x^2 - y^2/2 & \text{for } |x| < R_x, |y| < R_y \\ 0 & \text{otherwise} \end{cases} \tag{B.5}$$

where $N_x = \sqrt{2\pi}\sigma_x \operatorname{erf}(R_x/\sqrt{2}\sigma_x)$ and $N_y = \sqrt{2\pi}\sigma_y \operatorname{erf}(R_y/\sqrt{2}\sigma_y)$, we have

$$\begin{aligned}
&\int_{-R_x}^{R_x} dx_s N_x^{-1} \exp(-x_s^2/2\sigma_x^2) \frac{1}{\sqrt{4\pi Dct}} \exp(-\frac{(x_s - x)^2}{4Dct}) \\
&= \frac{\operatorname{erf}^{-1}(\frac{R_x}{\sqrt{2}\sigma_x})}{\sqrt{8\pi(2Dct + \sigma_x^2)}} \exp(-\frac{x^2}{2(2Dct + \sigma_x^2)}) \left\{ \operatorname{erf}(\frac{R_x - \beta_x x}{\sqrt{4\beta_x Dct}}) + \operatorname{erf}(\frac{R_x + \beta_x x}{\sqrt{4\beta_x Dct}}) \right\}
\end{aligned} \tag{B.6}$$

where $\beta_x = \sigma_x^2/(2Dct + \sigma_x^2)$, thus

$$\begin{aligned}
G_{2D}^2(\rho, t) &= \frac{\operatorname{erf}^{-1}(R_x/\sqrt{2}\sigma_x) \operatorname{erf}^{-1}(R_y/\sqrt{2}\sigma_y)}{8\pi\sqrt{(2Dct + \sigma_x^2)(2Dct + \sigma_y^2)}} \exp(-\frac{x^2}{2(2Dct + \sigma_x^2)} - \frac{y^2}{2(2Dct + \sigma_y^2)}) \\
&\quad \times \left\{ \operatorname{erf}(\frac{R_x - \beta_x x}{\sqrt{4\beta_x Dct}}) + \operatorname{erf}(\frac{R_x + \beta_x x}{\sqrt{4\beta_x Dct}}) \right\} \\
&\quad \times \left\{ \operatorname{erf}(\frac{R_y - \beta_y y}{\sqrt{4\beta_y Dct}}) + \operatorname{erf}(\frac{R_y + \beta_y y}{\sqrt{4\beta_y Dct}}) \right\}
\end{aligned} \tag{B.7}$$

where $\beta_y = \sigma_y^2/(2Dct + \sigma_y^2)$.

Appendix C

Parallel Monte Carlo Simulation Code

The parallel Monte Carlo code to calculate the photon density and photon distribution at any position in a uniform medium (infinite or semi-infinite) is presented here. This program uses the Multiplicative Lagged Fibonacci Generator from the Scalable Parallel Random Number Generator libraries (SPRNG) to generate random numbers and Message Passing Interface (MPI) to parallelize the simulation. It supports resuming from previous finished Monte Carlo calculation.

Listing C.1: MPI Monte Carlo Code

```
1  /*
2   * A program for photon density and photon distribution calculation
3   * using the Monte Carlo method.
4   *
5   * Features:
6   *          Use MPI
7   *          Checkpoint capability
8   *
9   * By M. Xu, 8/17/2001
10  */
11
```

```
12 #include <assert.h>
13 #include <stdio.h>
14 #include <stdlib.h>
15 #include <math.h>
16 #include <mpi.h>                    /* MPI header file */
17
18 /* Uncomment the following line to get the interface with pointer
      checking */
19 /* #define CHECK_POINTERS */
20 #define SIMPLE_SPRNG
21 #define USE_MPI
22 #include "sprng.h"                  /* SPRNG header file */
23 #define SEED 985456376              /* seed for sprng */
24 #define ranf() sprng() /* we will be using sprng as random number
      generator */
25
26 /*#define SEMI_SPACE*/              /* in semi-infinite space */
27 #undef SEMI_SPACE                   /* in infinite space */
28
29 #define RING_TARGET                 /* over rings on the plane */
30 /* #define POINT_TARGET */
31
32 #define PI M_PI
33 #define TBINS 201                   /* time bins */
34
35 static char rcsid[] = "$Id: time_mc_mpi.c,v
       1.12 2001/08/28 19:46:49 minxu Exp $";
36
37 static double mu_a = 0.;            /* absorption coefficient in 1/mm */
38 static double mu_s = 10;            /* Scattering Coefficient in 1/mm */
39 static double g = 0.9;              /* Scattering Anisotropy -1<=g<=1 */
40 static double n = 1.;               /* Index of refraction of medium */
41 static double ps_per_bin = 0.5;     /* picoseconds per bin */
42
43 static double x,y,z,t,xold,yold,zold,told,u,v,w; /* positions, time
      , and directional cosines */
44 static double rs;                   /* Specular Reflection */
45 static double rd;                   /* Total Backscattered Reflection */
46 static double albedo, crit_angle, weight, bit;
47
48 #ifdef POINT_TARGET
49 #undef RING_TARGET
50 #define ABINS 201                   /* cos(theta) bins from [-1, 1] */
51 static double tx = 0, ty = 0;
52 static double tz = 60, delta = 2; /* target (tx,ty,tz), [tz-delta/2,
53                                        * tz+delta/2], in mfp */
54 static double count[TBINS];         /* local photon counts in each bin
       */
55 static double countI[TBINS][ABINS]; /* local photon counts within
      the forward direction in each bin */
56 #endif
57
58 #ifdef RING_TARGET
```

```
59 #undef POINT_TARGET
60 #define ABINS 300                    /* redefine ABINS as the number of
       rings */
61 #define R_STEP 1                     /* total 300mfp = 30lt */
62 static double tz = 30, delta = 2; /* target (.,tz), [tz-delta/2,
63                                        * tz+delta/2], in mfp */
64 static double count[TBINS];          /* local photon counts in each bin
       */
65 static double countI[TBINS][ABINS]; /* local photon counts within
       the forward direction in each bin */
66 #endif
67
68 static void launch()                 /* Start the photon */
69 {
70     x = 0.0; y = 0.0; z = 0.0; t = 0.0; told = 0.0;
71     u = 0.0; v = 0.0; w = 1.0;
72     weight = 1.0 - rs;
73 }
74
75
76 static void bounce ()                /* Interact with top surface */
77 {
78     double tt, temp, templ, tf;
79
80     w = -w;
81     z = -z;
82     if (w <= crit_angle) return; /* total internal reflection */
83
84     tt    = sqrt(1.0-n*n*(1.0-w*w)); /* cos of exit angle */
85     templ = (w - n*tt)/(w + n*tt);
86     temp  = (tt - n*w)/(tt + n*w);
87     tf    = 1.0-(templ*templ+temp*temp)/2.0; /* Fresnel transmission
          */
88     rd   += tf * weight;
89
90     weight -= tf * weight;
91 }
92
93
94 static void move()                   /* move to next scattering or
       absorption event */
95 {
96     double d;
97     d = -log(ranf());
98     assert(d>0);
99     xold = x;
100    yold = y;
101    zold = z;
102    told = t;
103    x += d * u;
104    y += d * v;
105    z += d * w;
106    t += d;                           /* total path length in mfp */
```

```
107 #ifdef SEMI_SPACE
108     if ( z<=0 ) bounce();
109 #endif
110 }
111
112
113 static void scatter()           /* Scatter photon and establish new
        direction */
114 {
115     double x1, x2, x3, tt, mu;
116
117     for(;;) {                   /*new direction*/
118         x1=2.0*ranf() - 1.0;
119         x2=2.0*ranf() - 1.0;
120         if ((x3=x1*x1+x2*x2)<=1) break;
121     }
122     if (g==0) {                 /* isotropic */
123         u = 2.0 * x3 -1.0;
124         v = x1 * sqrt((1-u*u)/x3);
125         w = x2 * sqrt((1-u*u)/x3);
126         return;
127     }
128
129     /* generate mu = cos(theta) from superposition */
130     mu = (1-g*g)/(1-g+2.0*g*ranf());
131     mu = (1 + g*g-mu*mu)/2.0/g;
132     assert(-1 - 1e-11 <= mu && mu <= 1 + 1e-11);
133
134     if ( fabs(w) < 0.7 ) {
135         tt = mu * u + sqrt((1-mu*mu)/(1-w*w)/x3) * (x1*u*w-x2*v);
136         v  = mu * v + sqrt((1-mu*mu)/(1-w*w)/x3) * (x1*v*w+x2*u);
137         w  = mu * w - sqrt((1-mu*mu)*(1-w*w)/x3) * x1;
138     } else {
139         tt = mu * u + sqrt((1-mu*mu)/(1-v*v)/x3) * (x1*u*v + x2*w);
140         w  = mu * w + sqrt((1-mu*mu)/(1-v*v)/x3) * (x1*v*w - x2*u);
141         v  = mu * v - sqrt((1-mu*mu)*(1-v*v)/x3) * x1;
142     }
143     u = tt;
144     assert(1-1e-12<u*u+v*v+w*w && u*u+v*v+w*w<1+1e-12);
145 }
146
147
148 static void absorb ()           /* Absorb light in the medium */
149 {
150     weight *= albedo;
151     if (weight < 0.001){        /* Roulette */
152         bit -= weight;
153         if (ranf() > 0.1) weight = 0; else weight /= 0.1;
154         bit += weight;
155     }
156 }
157
158
```

```
159 static void read_pre_state(int id, double count[TBINS], double
        countI[TBINS][ABINS], double *photons, char *bytes)
160 {
161     FILE *fin;
162     int i, j, size;
163     double junk;
164     char fname[100], line[300000];
165
166     sprintf(fname, "time_mc_mpi.out.%02d", id);
167     fin = fopen(fname, "r");
168     fprintf(stderr, "%02d:\tFile: %s\n", id, fname);
169
170     fread(&size, 1, sizeof(int), fin);
171     fread(bytes, 1, size, fin);
172     fgets(line, sizeof(line), fin); /* finished the bytes line */
173     fgets(line, sizeof(line), fin); /* rcsid */
174
175     fgets(line, sizeof(line), fin);
176     sscanf(line, "Scattering   =%lf", &junk);
177     if (junk != mu_s) {
178         fprintf(stderr, "Incompatible mu_s found: %f %f\n", junk,
                mu_s);
179         exit(1);
180     }
181
182     fgets(line, sizeof(line), fin);
183     sscanf(line, "Absorption   =%lf", &junk);
184     if (junk != mu_a) {
185         fprintf(stderr, "Incompatible mu_a found.\n");
186         exit(1);
187     }
188
189     fgets(line, sizeof(line), fin);
190     sscanf(line, "Anisotropy   =%lf",    &junk);
191     if (junk != g) {
192         fprintf(stderr, "Incompatible g found.\n");
193         exit(1);
194     }
195
196     fgets(line, sizeof(line), fin);
197     sscanf(line, "Refr Index   =%lf",    &junk);
198     if (junk != n) {
199         fprintf(stderr, "Incompatible n found.\n");
200         exit(1);
201     }
202
203     fgets(line, sizeof(line), fin);
204     sscanf(line, "Ps_per_bin   =%lf", &junk);
205     if (junk != ps_per_bin) {
206         fprintf(stderr, "Incompatible ps_per_bin found.\n");
207         exit(1);
208     }
209
```

```
210     fgets(line, sizeof(line), fin);
211     sscanf(line, "Photons      =%lf",    photons);
212
213     fgets(line, sizeof(line), fin);
214     sscanf(line, "Specular Refl=%lf",    &rs);
215
216     fgets(line, sizeof(line), fin);
217     sscanf(line, "Backsct Refl =%lf",    &rd);
218     fprintf(stderr, "%02d:\tPrevious photons, rs, rd: %f %f %f\n",
           id, *photons, rs, rd);
219
220     fgets(line, sizeof(line), fin);
221     fgets(line, sizeof(line), fin);
222
223     for (i=0; i<TBINS; i++) {
224         fscanf(fin, "%lf %lf", &junk, &count[i]);
225         for (j=0; j<ABINS; j++) fscanf(fin, " %lf", &countI[i][j]);
226         fscanf(fin, "\n");
227     }
228
229     fclose(fin);
230
231     /* fprintf(stderr, "CHECK: %f %f %f %f %f %f\n", count[0], count
           [1], countI[0][0], countI[1][0], countI[0][200], countI
           [1][200]); */
232 }
233
234
235 static void write_cur_state(int id, double count[TBINS], double
       countI[TBINS][ABINS], double photons, char *bytes, int size)
236 {
237     FILE *fout;
238     char fname[100], cmd[300];
239     int i, j;
240
241     if (id != -1)
242         sprintf(fname, "time_mc_mpi.out.%02d", id);
243     else
244         sprintf(fname, "time_mc_mpi.out");
245
246     sprintf(cmd, "mv %s %s.bak", fname, fname);
247     system(cmd);
248     fout = fopen(fname, "w");
249
250     fwrite(&size, 1, sizeof(int), fout);
251     fwrite(bytes, 1, size, fout);
252     fprintf(fout, "\n%s\n", rcsid);
253     fprintf(fout, "Scattering   = %8.3f\n", mu_s);
254     fprintf(fout, "Absorption   = %8.3f\n", mu_a);
255     fprintf(fout, "Anisotropy   = %8.3f\n",    g);
256     fprintf(fout, "Refr Index   = %8.3f\n",    n);
257     fprintf(fout, "Ps_per_bin   = %8.3f\n",    ps_per_bin);
258     fprintf(fout, "Photons      = %e\n",       photons);
```

```
259     fprintf(fout, "Specular Refl= %10.5f\n",    rs);
260     fprintf(fout, "Backsct Refl = %10.5f\n",    rd);
261     fprintf(fout, "Time    Photon Density    Photon Intensity (cos
           : -1..1)\n");
262     fprintf(fout, "[ps]    [number]          [number]\n");
263
264     for (i=0; i<TBINS; i++) {
265         fprintf(fout, "%6.4f %e", i*ps_per_bin, count[i]);
266         for (j=0; j<ABINS; j++) fprintf(fout, " %e", countI[i][j]);
267         fprintf(fout, "\n");
268     }
269
270     fclose(fout);
271 }
272
273
274 static void work (int id, double *photons, int resume)
275 {
276     int i, j, k, size;
277     double bins_per_mfp, ophotons, tmp;
278     char *bytes, packed[MAX_PACKED_LENGTH];
279
280     if  (resume == 1) {
281         read_pre_state(id, count, countI, &ophotons, packed);
282         unpack_sprng(packed);
283     }
284
285     fprintf(stderr, "START 00 %f\n", countI[0][0]);
286
287     albedo = mu_s / (mu_s + mu_a);
288     rs = (n-1.0)*(n-1.0)/(n+1.0)/(n+1.0); /* specular reflection */
289     crit_angle = sqrt(1.0-1.0/n/n); /* cos of critical angle */
290     bins_per_mfp = (1.0/mu_s) / (0.2998/n) / ps_per_bin;
291
292     for (i = 1; i <= *photons; i++){
293         if ( i % 10000 == 0) fprintf(stderr, "%02d:\t%d\n", id, i);
294         launch ();
295         while (weight > 0) {
296             move ();
297
298 #ifdef POINT_TARGET
299             j = (1+w)/2*(ABINS-1);
300
301             /* put the photon (told, t] into corresponding bins */
302             for ( k = told*bins_per_mfp+1; k <= t*bins_per_mfp; k
                   ++) {
303                 if (k >= TBINS) continue;
304                 if ( fabs(zold + w*(k/bins_per_mfp-told) - tz) <
                       delta/2
305                   && fabs(xold + u*(k/bins_per_mfp-told) - tx) <
                         delta/2
306                   && fabs(yold + v*(k/bins_per_mfp-told) - ty) <
                         delta/2 ) {
```

```
307                     count[k] += weight;
308                     countI[k][j] += weight;
309                 }
310             }
311
312
313             if ( TBINS < (t+sqrt((x-tx)*(x-tx)+(y-ty)*(y-ty)+(z-tz
                    )*(z-tz))
314                         -delta/2)*bins_per_mfp )
315                 break;          /* too far away to touch the (tx, ty
                    , tz) in
316                                  * time TBINS */
317 #endif
318
319 #ifdef RING_TARGET
320             /* put the photon (told, t] into corresponding bins */
321             for ( k = told*bins_per_mfp+1; k <= t*bins_per_mfp; k
                    ++) {
322                 if (k >= TBINS) continue;
323                 if ( fabs(zold + w*(k/bins_per_mfp-told) - tz) <
                        delta/2 ) {
324                     count[k] += weight;
325                     if ( w >= 0.99 ) {
326                         tmp = k/bins_per_mfp-told;
327                         j = (int)( sqrt( (xold + u*tmp)*(xold + u*
                            tmp) + (yold + v*tmp)*(yold + v*tmp) ) /
                            R_STEP );
328                         assert (j<ABINS);
329                         countI[k][j] += weight;
330                         if (countI[0][0] != 0) {
331                             fprintf(stderr, "WARNING: 00 %f at round
                                %d\n", countI[0][0], i);
332                             fprintf(stderr, "DEBUG: xold, yold, zold
                                , told=%f %f %f %f\n", xold, yold,
                                zold, told);
333                             fprintf(stderr, "DEBUG: u, v, w=%f %f %f
                                \n", u, v, w);
334                             fprintf(stderr, "DEBUG: x, y, z, t=%f %f
                                %f %f\n", x, y, z, t);
335                             fprintf(stderr, "DEBUG: intercept at x,
                                y, z, t=%f %f %f %f\n", xold+u*tmp,
                                yold+v*tmp, zold+w*tmp, told+tmp);
336                             fprintf(stderr, "DEBUG: k, j, tmp,
                                bins_per_mfp=%d %d %f %f\n", k, j,
                                tmp, bins_per_mfp);
337                             exit(1); }
338                     }
339                 }
340             }
341
342             if ( TBINS < (t + fabs(z-tz) -delta/2)*bins_per_mfp )
343                 break;          /* too far away to touch the (, , tz
                    ) in
344                                  * time TBINS */
```

```
345 #endif
346
347             absorb ();
348             scatter ();
349         }
350     }
351
352     *photons += bit + ophotons;
353     size = pack_sprng(&bytes);
354
355     fprintf(stderr, "END 00 %f\n", countI[0][0]);
356     write_cur_state(id, count, countI, *photons, bytes, size);
357 }
358
359
360 int main(int argc, char *argv[])
361 {
362     int myid, nprocs, resume;
363     int i, j;
364     double sum[TBINS], sumI[TBINS][ABINS], ugly[TBINS*ABINS], uglyut
        [TBINS*ABINS];
365     double photons, photons_arr
        [] = {100000*1, 1000000*1, 1000000*1, 1000000*1, 1000000*1};
        /* in each process, 1 unit takes about 14min */
366     double total_photons = 0;
367     MPI_Datatype MatrixType;
368
369     MPI_Init(&argc, &argv);         /* Initialize MPI */
370     MPI_Comm_rank(MPI_COMM_WORLD, &myid); /* find process id */
371     MPI_Comm_size(MPI_COMM_WORLD, &nprocs); /* find number of
        processes */
372
373     MPI_Type_vector(TBINS, ABINS, ABINS, MPI_DOUBLE, &MatrixType);
374     MPI_Type_commit(&MatrixType);
375
376     if(myid == 0)
377     {
378         printf("Is this a resume? (1 for resume, otherwise restart
            ): ");
379         scanf("%d", &resume);
380     }
381     MPI_Bcast(&resume, 1, MPI_INT, 0, MPI_COMM_WORLD);
382
383     init_sprng(SPRNG_MLFG, SEED, LAG1279);      /* initialize stream
        */
384
385     printf("\n\nProcess %d, print information about stream:\n", myid
        );
386     print_sprng();
387
388     photons = photons_arr[myid];
389     work(myid, &photons, resume);
390
```

```
391     for (i = 0; i < TBINS; i++)
392         for (j = 0; j < ABINS; j++)
393             ugly[i*ABINS+j] = countI[i][j];
394
395     MPI_Reduce(count, sum, TBINS, MPI_DOUBLE, MPI_SUM, 0,
            MPI_COMM_WORLD);
396     /* MPI_Reduce(&countI[0][0], &sumI[0][0], 1, MatrixType, MPI_SUM
            , 0, MPI_COMM_WORLD); */
397     MPI_Reduce(ugly, uglyut, TBINS*ABINS, MPI_DOUBLE, MPI_SUM, 0,
            MPI_COMM_WORLD);
398     MPI_Reduce(&photons, &total_photons, 1, MPI_DOUBLE, MPI_SUM, 0,
            MPI_COMM_WORLD);
399
400     if (myid == 0) {
401         for (i = 0; i < TBINS; i++)
402             for (j = 0; j < ABINS; j++)
403                 sumI[i][j] = uglyut[i*ABINS+j];
404         write_cur_state(-1, sum, sumI, total_photons, "", 0);
405     }
406
407     MPI_Finalize();                 /* Terminate MPI */
408
409     return 0;
410 }
```

Appendix D

Cumulant Solution to the Boltzmann Equation

The Boltzmann equation for photon distribution function $I(\mathbf{r}, \mathbf{s}, t)$ at position $\mathbf{r}$, direction $\mathbf{s}$ and time t from a unit source at position $\mathbf{r}_0$ propagating along $\mathbf{s}_0$ at time $t = 0$, is given by

$$\begin{aligned} &\frac{\partial}{\partial t} I(\mathbf{r}, \mathbf{s}, t) + c\mathbf{s} \cdot \nabla_{\mathbf{r}} I(\mathbf{r}, \mathbf{s}, t) + c[\mu_s(\mathbf{r}) + \mu_a(\mathbf{r})] I(\mathbf{r}, \mathbf{s}, t) \\ &= c\mu_s(\mathbf{r}) \int d\mathbf{s}' P(\mathbf{s}, \mathbf{s}') I(\mathbf{r}, \mathbf{s}', t) d\mathbf{s}' + \delta(\mathbf{r} - \mathbf{r}_0)\delta(\mathbf{s} - \mathbf{s}_0)\delta(t) \end{aligned} \tag{D.1}$$

where c is the light speed inside the medium, μ_a and μ_s denote the position-dependent absorption and scattering coefficients with a unit of inverse length, and $P(\mathbf{s}, \mathbf{s}')$ is the normalized phase function of the light propagation in the medium.

Assume the medium is infinite and uniform, and the known phase function depends only on the scattering angle $\mathbf{s}\cdot\mathbf{s}'$, the phase function can then be expanded in Legendre

polynomials,

$$P(\mathbf{s}, \mathbf{s}') = (4\pi)^{-1} \sum_l a_l \, \mathrm{P}_l(\mathbf{s} \cdot \mathbf{s}'). \tag{D.2}$$

The key observation is that the photon evolution in direction space, $F(\mathbf{s}, t|\mathbf{s}_0) = \int d^3\mathbf{r} I(\mathbf{r}, \mathbf{s}, t|\mathbf{r}_0, \mathbf{s}_0)$, can be analytically solved. The photon evolution in direction space obeys a separable equation

$$\begin{aligned} & \frac{\partial}{\partial t} F(\mathbf{s}, t|\mathbf{s}_0) + c[\mu_s + \mu_a] F(\mathbf{s}, t|\mathbf{s}_0) \\ = \; & c\mu_s \int d\mathbf{s}' P(\mathbf{s} \cdot \mathbf{s}') F(\mathbf{s}', t|\mathbf{s}_0) + \delta(\mathbf{s} - \mathbf{s}_0)\delta(t) \end{aligned} \tag{D.3}$$

with the solution

$$F(\mathbf{s}, t|\mathbf{s}_0) = \frac{\exp(-\mu_a c t)}{4\pi} \sum_l (2l + 1) \exp(-g_l t) \, \mathrm{P}_l(\mathbf{s} \cdot \mathbf{s}_0). \tag{D.4}$$

Here $g_l = c\mu_s[1 - a_l/(2l + 1)]$, especially $g_0 = 0$ and $g_1 = c\mu_s'$ where μ_s' is the reduced scattering coefficient.

The characteristic function of the photon distribution $I(\mathbf{r}, \mathbf{s}, t)$ is defined as

$$\langle \exp(-i\mathbf{k} \cdot \mathbf{r}) \rangle = \int d\mathbf{r} \exp(-i\mathbf{k} \cdot \mathbf{r}) \, I(\mathbf{r}, \mathbf{s}, t). \tag{D.5}$$

Hence the photon distribution itself equals to

$$I(\mathbf{r}, \mathbf{s}, t) = \frac{1}{(2\pi)^3} \int d\mathbf{k} \exp(i\mathbf{k} \cdot \mathbf{r}) \langle \exp(-i\mathbf{k} \cdot \mathbf{r}) \rangle . \tag{D.6}$$

through an inverse Fourier transform.

The photon distribution $I(\mathbf{r}, \mathbf{s}, t)$ can then be expressed as

$$\begin{aligned} & I(\mathbf{r}, \mathbf{s}, t) \\ = & \frac{1}{(2\pi)^3} \left\langle \int d\mathbf{k} \exp(i\mathbf{k} \cdot \mathbf{r}) \right. \\ & \left. \times \exp\left[\sum_{n=1}^{\infty} \sum_{n_1+n_2+n_3=n} \frac{(-ic)^n \, C_{n_1+n_2}^{n_1} \, C_n^{n_1+n_2} \, k_1^{n_1} k_2^{n_2} k_3^{n_3}}{n!} A_c \right] \right\rangle \end{aligned} \tag{D.7}$$

by applying the cumulant expansion theorem [75] to the term $\langle \exp(-i\mathbf{k} \cdot \mathbf{r}) \rangle$ in Eq. (D.6). Here the cumulant

$$A_c = \langle r_1^{n_1} r_2^{n_2} r_3^{n_3} \rangle_c = \left\langle \left(\int_0^t s_1(t')dt' \right)^{n_1} \left(\int_0^t s_2(t')dt' \right)^{n_2} \left(\int_0^t s_3(t')dt' \right)^{n_3} \right\rangle_c$$

is obtainable from moments by its definition [75]. For example, the second cumulant is defined as $\langle xy \rangle_c = \langle xy \rangle - \langle x \rangle \langle y \rangle$.

We only need to evaluate the moments of a form of

$$\begin{aligned} A &= \left\langle \left(\int_0^t s_1(t')dt' \right)^{n_1} \left(\int_0^t s_2(t')dt' \right)^{n_2} \left(\int_0^t s_3(t')dt' \right)^{n_3} \right\rangle \\ &= \left\langle \int_0^t dt^{(1)} \cdots \int_0^t dt^{(n)} \underbrace{s_1(t^{(1)}) \cdots s_1(t^{(n_1)})}_{n_1} \right. \\ &\quad \left. \times \underbrace{s_2(t^{(n_1+1)}) \cdots s_2(t^{(n_1+n_2)})}_{n_2} \underbrace{s_3(t^{(n_1+n_2+1)}) \cdots s_3(t^{(n)})}_{n_3} \right\rangle \end{aligned} \tag{D.8}$$

which is an assemble average inside the direction space and over all possible ordering of time $t^{(i)}$. The contribution from a specific ordering of time can be evaluated using the exact Green's function $F(\mathbf{s}, t|\mathbf{s}_0)$ in the direction space through the following

formula

$$\left\langle \int_0^t dt^{(n)} \dots \int_0^t dt^{(1)} \sigma_n(t^{(n)}) \dots \sigma_1(t^{(1)}) \right\rangle_{t^{(1)} \le t^{(2)} \le \dots \le t^{(n)}}$$
$$= \frac{1}{F(\mathbf{s}, t|\mathbf{s}_0)} \int_0^t dt^{(n)} \int_0^{t^{(n)}} dt^{(n-1)} \dots \int_0^{t^{(2)}} dt^{(1)} \int d\mathbf{s}^{(n)} \int d\mathbf{s}^{(n-1)} \dots \int d\mathbf{s}^{(1)}$$
$$\times F(\mathbf{s}, t - t^{(n)}|\mathbf{s}^{(n)}) \sigma_n F(\mathbf{s}^{(n)}, t^{(n)} - t^{(n-1)}|\mathbf{s}^{(n-1)}) \sigma_{n-1} \dots \sigma_1 F(\mathbf{s}^{(1)}, t^{(1)}|\mathbf{s}_0)$$

where σ_i is a function of the direction $\mathbf{s}$ at different times and which comes from the property of the Green's function.

The code to calculate the photon distribution up to an arbitrary order has been implemented in C++ using the g++ compiler (version 2.95.4) in a Linux box. The code is too big to be fully listed here.

Listing D.1: Makefile

```
1  CSRC=dfunc.C test.C permute.C misc.C termvec.C cumulant.C tree.C
       legendre.C # mk4storage.C
2  FSRC=
3  OBJS=${CSRC:.C=.o} ${FSRC:.r=.o}
4  CXXFLAGS=-g  -O3 -Wall -pedantic
5  FFLAGS=-g -I/usr/local/include
6  LFLAGS=-L/usr/local/lib -lalfpack -lslatec -llapack -lblas -lg2c #-
       lmk4
7  CXX=/usr/bin/g++
8
9  .C.o:
10         ${CXX} ${CXXFLAGS} -c $*.C
11
12 .r.o:
13         r2f $*.r
14         ${FC} ${FFLAGS} -c $*.f
15
16 all: ${OBJS}
17         ${CXX} ${CXXFLAGS} -o test ${OBJS} ${LFLAGS}
18
19 termvt: termvec.o
20         ${CXX} ${CXXFLAGS} -o termvec $<
21
22 clean:
23         rm -f *.o *~ *.bak
24 # DO NOT DELETE
```

```
25
26 cumulant.o: cumulant.h tree.h /usr/include/complex.h /usr/include/
       features.h
27 cumulant.o: /usr/include/sys/cdefs.h /usr/include/gnu/stubs.h
28 cumulant.o: /usr/include/bits/mathdef.h /usr/include/bits/cmathcalls
       .h misc.h
29 cumulant.o: /usr/include/math.h /usr/include/bits/huge_val.h
30 cumulant.o: /usr/include/bits/mathcalls.h config.h dfunc.h termvec.h
31 cumulant.o: permute.h xtlstorage.h
32 dfunc.o: dfunc.h /usr/include/math.h /usr/include/features.h
33 dfunc.o: /usr/include/sys/cdefs.h /usr/include/gnu/stubs.h
34 dfunc.o: /usr/include/bits/huge_val.h /usr/include/bits/mathdef.h
35 dfunc.o: /usr/include/bits/mathcalls.h /usr/include/complex.h
36 dfunc.o: /usr/include/bits/cmathcalls.h termvec.h misc.h config.h
       permute.h
37 dfunc.o: xtlstorage.h
38 legendre.o: legendre.h /usr/include/math.h /usr/include/features.h
39 legendre.o: /usr/include/sys/cdefs.h /usr/include/gnu/stubs.h
40 legendre.o: /usr/include/bits/huge_val.h /usr/include/bits/mathdef.h
41 legendre.o: /usr/include/bits/mathcalls.h misc.h /usr/include/
       complex.h
42 legendre.o: /usr/include/bits/cmathcalls.h config.h
43 misc.o: misc.h /usr/include/math.h /usr/include/features.h
44 misc.o: /usr/include/sys/cdefs.h /usr/include/gnu/stubs.h
45 misc.o: /usr/include/bits/huge_val.h /usr/include/bits/mathdef.h
46 misc.o: /usr/include/bits/mathcalls.h /usr/include/complex.h
47 misc.o: /usr/include/bits/cmathcalls.h config.h
48 permute.o: permute.h misc.h /usr/include/math.h /usr/include/
       features.h
49 permute.o: /usr/include/sys/cdefs.h /usr/include/gnu/stubs.h
50 permute.o: /usr/include/bits/huge_val.h /usr/include/bits/mathdef.h
51 permute.o: /usr/include/bits/mathcalls.h /usr/include/complex.h
52 permute.o: /usr/include/bits/cmathcalls.h config.h
53 termvec.o: termvec.h /usr/include/math.h /usr/include/features.h
54 termvec.o: /usr/include/sys/cdefs.h /usr/include/gnu/stubs.h
55 termvec.o: /usr/include/bits/huge_val.h /usr/include/bits/mathdef.h
56 termvec.o: /usr/include/bits/mathcalls.h
57 test.o: cumulant.h tree.h /usr/include/complex.h /usr/include/
       features.h
58 test.o: /usr/include/sys/cdefs.h /usr/include/gnu/stubs.h
59 test.o: /usr/include/bits/mathdef.h /usr/include/bits/cmathcalls.h
       misc.h
60 test.o: /usr/include/math.h /usr/include/bits/huge_val.h
61 test.o: /usr/include/bits/mathcalls.h config.h dfunc.h termvec.h
       permute.h
62 test.o: xtlstorage.h
63 tree.o: tree.h /usr/include/complex.h /usr/include/features.h
64 tree.o: /usr/include/sys/cdefs.h /usr/include/gnu/stubs.h
65 tree.o: /usr/include/bits/mathdef.h /usr/include/bits/cmathcalls.h
       misc.h
66 tree.o: /usr/include/math.h /usr/include/bits/huge_val.h
67 tree.o: /usr/include/bits/mathcalls.h config.h
```

Appendix E

Miscellaneous Codes

Listing E.1: intralipid.py

```
1  # Intralipid-10% 500mL has:
2  # type            g        mL
3  # glycerin        11.25    8.92
4  # lecithin        6        5.82
5  # soybean oil     50       53.94
6  # water           430.5    431.33
7  #
8  # The absorption and scattering is mainly from soybean oil.
9  # The wavelength should be in nm.
10 import fmm
11 from Math import sqrt, array
12 import Interpolation
13
14 def refraction_index_tio2(wavelength):
15     " return no, ne, n at one wavelength, in micro "
16     wv = [0.4358, 0.4916, 0.4960, 0.5461, 0.5770, 0.5791, 0.6907,\
17           0.7082, 1.014, 1.5296]
18     no = [2.853, 2.725, 2.718, 2.652, 2.623, 2.621, 2.555, 2.548,\
19           2.484, 2.454]
20     ne = [3.216, 3.051, 3.042, 2.958, 2.921, 2.919, 2.836, 2.826,\
21           2.747, 2.71]
22
23     s1 = Interpolation.InterpolatingFunction((array(wv),), array(no
       ))
24     s2 = Interpolation.InterpolatingFunction((array(wv),), array(ne
       ))
25     vno = s1(wavelength)
26     vne = s2(wavelength)
27     vn  = vno*vne*sqrt(2./(vno*vno+vne*vne))
```

```
28      #print "# TiO2 wavelength(micro), no, ne, n=", wavelength, vno,
            vne, vn
29      return vno, vne, vn
30
31  def refraction_index(wavelength, type):
32      # wavelength in nm.
33      wavelength = wavelength + 0.0
34      if type == "soybean":
35          return 1.451 + 1.154*10e4/wavelength**2 - 1.132*10e9/
                wavelength**4
36      if type == "water":
37          return 1.311 + 1.154*10e4/wavelength**2 - 1.132*10e9/
                wavelength**4
38      if type == "tio2":
39          return refraction_index_tio2(wavelength/1000.)[2]
40      raise RuntimeError, "Unknown type"
41
42  def constituent(intralipid10, water):
43      # different constituent in mL
44      glycerin = intralipid10*8.92/500
45      lecithin = intralipid10*5.82/500
46      soybean = intralipid10*53.94/500
47      water = intralipid10*431.33/500 + water
48      return glycerin, lecithin, soybean, water
49
50  def lt(wavelength, intralipid10, water):
51      # wavelength in nm, intralipid10: Intralipid-10% in mL, water:
            water in mL
52      # for intralipid-10%
53      g = 1.1 - 0.58*wavelength/1000
54      mus0 = 0.016*(wavelength/1000.)**(-2.4)
55      musp0 = mus0*(1-g)
56      lt0 = 1./musp0
57      density0 = 53.94/500
58      # this liquid
59      glycerin, lecithin, soybean, water = constituent(intralipid10,
            water)
60      density = soybean/(water+soybean+glycerin+lecithin)
61      return lt0*density0/density/1000
62
63  def composition_refraction_index(wavelength, intralipid10, water):
64      # Use Bruggeman approach
65      glycerin, lecithin, soybean, water = constituent(intralipid10,
            water)
66      # p is the volume percentage of soybean
67      p = soybean/(water+soybean)
68      n1 = refraction_index(wavelength, 'soybean')
69      n2 = refraction_index(wavelength, 'water')
70      print n1, n2
71      e1 = n1**2
72      e2 = n2**2
73      def f(ebar, e1, e2, p):
74          return p*(ebar-e1)/(e1+2*ebar) + (1-p)*(ebar-e2)/(e2+2*ebar)
75      ebar = fmm.zeroin(f, e1, e2, 1e-10, e1, e2, p)
```

```
76      return sqrt(ebar)
77
78  print "lt=", lt(800, 770, 7500)
79  print "n=", composition_refraction_index(800, 58, 580)
80  print "n=", refraction_index(800, 'water')
81
82
83  print "\nTiO2 at 527nm, n=", refraction_index(527, "tio2")
84  print "\nWater at 527nm, n=", refraction_index(527, "water")
85
86  print "\nTiO2 at 800nm, n=", refraction_index(800, "tio2")
87  print "\nWater at 800nm, n=", refraction_index(800, "water")
88
89  print "8/28/01"
90  print lt(1250, 194, 1225)
91
92  print "9/5/01"
93  print "\nTiO2 at 800nm, n=", refraction_index(800, "tio2")
```

Listing E.2: lc.py

```
1   # $Modified: Wed May 17 10:06:31 2000 by minxu $
2   import RNG
3   from fmm import fmin
4   from GLOBAL import Gmin
5   from curve import Curve
6   from graph2d import Graph2d
7   from Math import trans, mult, pi, zeros, cos, sin, exp, arange, triu
        , svd, rand, norm, paws, array, sum, xmin, sqrt, shape, herm, log
        , svd, concat
8
9
10  tikhonov_error = 'tikhonov_error'
11
12  class tikhonov:
13      def __init__(self, a, b, u=None, s=None, lams=None):
14          " a must be a real mxn matrix while b may be a complex array
                "
15          self.eps = 2.2e-16
16          if a == None:
17              self.u = u
18              self.s = s
19          else:
20              if a.typecode() in ['F', 'D']:
21                  raise tikhonov_error, 'data type error'
22              self.a = a
23              [self.u, self.s, self.v] = svd(a)
24          self.b = b
25          self.zbeta = mult(trans(self.u), b)
26          self.beta = abs(self.zbeta)
27          self.zxi = self.zbeta/self.s
28          self.xi = abs(self.zxi)
29          if shape(self.u)[0] > shape(self.u)[1]:
30              self.over_determined = 1
```

```
31              self.min_residue = norm(b-mult(self.u, self.zbeta))
32              # Or written in the following equvalent form
33              # self.min_residue = sqrt( mult(herm(b), b) - mult(herm(
                    self.zbeta), self.zbeta) )
34          else:
35              self.over_determined = 0
36              self.min_residue = 0
37          if lams == None:
38              self.reg_params()
39          else:
40              self.lams = lams
41          # the optimal reg_param
42          self.reg_c = 0
43          self.use_GLOBAL = 1
44
45      def reg_params(self, npoints=20):
46          " provide npoints of lambda points in an increasing order"
47          smin = 16*self.eps
48          reg_param = zeros(npoints, 'd')
49          reg_param[0] = max([self.s[len(self.s)-1], self.s[0]*smin]);
50          ratio = (self.s[0]/reg_param[0])**(1./(npoints-1));
51          for i in range(1, npoints):
52              reg_param[i] = ratio*reg_param[i-1]
53          self.lams = reg_param
54
55      def rho_eta(self, lam=None):
56          " return [rho, eta] "
57          if lam == None:
58              lam = self.lams
59          lam = array(lam)
60          nlam = len(lam)
61          rho = zeros(nlam, 'd')
62          eta = zeros(nlam, 'd')
63          for i in range(nlam):
64              f = (self.s**2)/(self.s**2 + lam[i]**2)
65              eta[i] = norm(f*self.xi);
66              rho[i] = norm((1-f)*self.beta);
67              if self.over_determined:
68                  rho[i] = sqrt(rho[i]**2 + self.min_residue**2)
69          if nlam == 1:
70              return [rho[0], eta[0]]
71          else:
72              return [rho, eta]
73
74      def solu(self, lam):
75          " accept one lam and return the solu "
76          return mult(self.s*self.zbeta/(self.s**2 + lam**2), self.v)
77
78
79  class lc(tikhonov):
80      def __init__(self, a, b, u=None, s=None, lams=None, verbose=0):
81          tikhonov.__init__(self, a, b, u, s, lams)
82          self.verbose = verbose
```

```
83
84      def lcfun(self, lam=None):
85          " computes the NEGATIVE of the curvature of l_curve "
86          # Initialization.
87          if lam == None:
88              lam = self.lams
89          lam = array(lam)
90          nlam = len(lam)
91          phi = zeros(nlam,'d'); dphi = zeros(nlam,'d');
92          psi = zeros(nlam,'d'); dpsi = zeros(nlam,'d');
93          eta = zeros(nlam,'d'); rho = zeros(nlam,'d');
94
95          # Compute some intermediate quantities.
96          for i in range(nlam):
97              f   = (self.s*self.s)/(self.s*self.s + lam[i]**2);
98              cf = 1 - f;
99              eta[i] = norm(f*self.xi);
100             rho[i] = norm(cf*self.beta);
101             f1 = -2*f*cf/lam[i];
102             f2 = -f1*(3-4*f)/lam[i];
103             phi[i]  = sum(f*f1*self.xi**2);
104             psi[i]  = sum(cf*f1*self.beta**2);
105             dphi[i] = sum((f1**2 + f*f2)*self.xi**2);
106             dpsi[i] = sum((-f1**2 + cf*f2)*self.beta**2);
107
108         # Now compute the first and second derivatives of eta and
              rho
109         # with respect to lam;
110         deta  =  phi/eta;
111         drho  = -psi/rho;
112         ddeta =  dphi/eta - deta*(deta/eta);
113         ddrho = -dpsi/rho - drho*(drho/rho);
114
115         # the above only holds when min_residue=0. if not
116         # then:
117         # assume: rho/rho_0 = alpha = sqrt(1+(min_residue/rho_0)^2)
118         #         rho = alpha*rho_0
119         #         drho  = drho_0/alpha
120         #         ddrho = (alpha^2*drho^2 + rho*ddrho_0/alpha - drho
              ^2)/rho
121         if self.over_determined:
122             alpha = sqrt(1+(self.min_residue/rho)**2)
123             rho   = alpha*rho
124             drho  = drho/alpha
125             ddrho = ((alpha*alpha-1)*drho*drho + rho*ddrho/alpha)/
                  rho
126
127         # Convert to derivatives of log(eta) and log(rho).
128         dlogeta  = deta/eta;
129         dlogrho  = drho/rho;
130         ddlogeta = ddeta/eta - dlogeta**2;
131         ddlogrho = ddrho/rho - dlogrho**2;
132
```

```
133             # Let g = -curvature.
134             g = - (dlogrho*ddlogeta - ddlogrho*dlogeta)/(dlogrho**2 +
                    dlogeta**2)**(1.5);
135             if nlam == 1: return g[0]
136             else: return g
137
138         def lcfunlog(self, loglam):
139             return self.lcfun(exp(loglam))
140
141         def l_corner(self):
142             " L_CORNER Locate the corner of the L-curve. Reg_param is in
                    an increasing order"
143             #
144             # [reg_c,rho_c,eta_c,kappa_max] =
145             #         l_corner(reg_param,U,s,b,method)
146             #
147             # Locates the "corner" of the L-curve in log-log scale.
148             #
149             # It is assumed that corresponding values of || A x - b
                    ||, || L x ||,
150             # and the regularization parameter are stored in the arrays
                    rho, eta,
151             # and reg_param, respectively (such as the output from
                    routine l_curve)
152             #
153             # Locate the corner.  If the curvature is negative
                    everywhere,
154             # then define the leftmost point of the L-curve as the
                    corner.
155             if self.use_GLOBAL:
156                 if self.verbose: print 'Use GLOBAL'
157                 [gmin, logreg_c, nf] = Gmin(self.lcfunlog, log(min(self.
                        lams)), log(max(self.lams)))
158                 reg_c = exp(logreg_c)
159             else:
160                 # Compute g = - curvature of L-curve.
161                 if self.verbose: print 'Use fmin'
162                 g = self.lcfun();
163                 while (1):
164                     [gmin, gi] = xmin(g)
165                     if gi != 0: break
166                     g = g[1:]
167                     if len(g) == 1:
168                         print 'l_corner warning: it is not a L-curve'
169                         print 'But I will continue.'
170                         gmin = g
171                         break
172 ##                  if len(g) == 1:
173 ##                      raise tikhonov_error, " l_corner failed"
174                 reg_c = fmin(self.lcfun, self.lams[max([0,gi-1])], self.
                        lams[min([gi+1, len(g)-1])], 1e-10)
175             kappa_max = - self.lcfun(reg_c) # Maximum curvature.
176             self.reg_c = reg_c
177             return [self.reg_c, kappa_max]
```

```
178
179     def plotlc(self):
180         [rho, eta] = self.rho_eta()
181         g = self.lcfun()
182         # the L_curve
183         c1 = Curve(y=eta, x=rho, type='line')
184         c2 = Curve(y=eta, x=rho, type='none', marks=1, marker='\5')
185         # the curvature curve
186         c3 = Curve(y=exp(g), x=rho)
187         g1 = Graph2d(c1, axis_scales='loglog')
188         g1.add(c2)
189         g1.add(c3)
190
191         if self.reg_c:
192             [rho_c, eta_c] = self.rho_eta(self.reg_c)
193             # the position of maxmimum curvature
194             c4 = Curve(y=arange(min(eta), max(eta), (max(eta)-min(
                    eta))/10), x=[rho_c]*10, type='dash')
195             g1.add(c4)
196         g1.plot()
197         paws()
198
199
200 class gcv(tikhonov):
201     def __init__(self, a, b, u=None, s=None, lams=None, verbose=0):
202         tikhonov.__init__(self, a, b, u, s, lams)
203         self.verbose = verbose
204
205     def gcvfun(self, lam=None):
206         " computes the GCV function "
207         # Initialization.
208         if lam == None:
209             lam = self.lams
210         lam = array(lam)
211         nlam = len(lam)
212         g = zeros(nlam, 'd')
213         mn = shape(self.u)[0]-shape(self.u)[1]
214         for i in range(nlam):
215             f = lam[i]**2/(self.s**2+lam[i]**2)
216             g[i] = (norm(f*self.zbeta)**2 + self.min_residue**2)/(mn
                        + sum(f)**2)
217         if nlam == 1: return g[0]
218         else: return g
219
220     def gcvfunlog(self, loglam):
221         return self.gcvfun(exp(loglam))
222
223     def minGcv(self):
224         " minGcv Locate the minimum of gcv curve. Reg_param is in an
                increasing order"
225         if self.use_GLOBAL:
226             if self.verbose: print 'Use GLOBAL'
227             [gmin, logreg_c, nf] = Gmin(self.gcvfunlog, log(1e-12),
```

```
                log(max(self.lams)));
228             reg_c = exp(logreg_c)
229             if reg_c - 1e-12 < 1e-16: raise tikhonov_error, "global
                    minimum is at the edge"
230         else:
231             if self.verbose: print 'Use fmin'
232             g = self.gcvfun()
233             while (1):
234                 [gmin, gi] = xmin(g)
235                 if gi != 0: break
236                 g = g[1:]
237                 if len(g) == 1:
238                     raise tikhonov_error, "minGcv failed"
239             reg_c = fmin(self.gcvfun, self.lams[max([0,gi-1])], self
                    .lams[min([gi+1, len(g)-1])], 1e-10)
240         self.reg_c = reg_c
241         return self.reg_c
242
243     def plotgcv(self):
244         g = self.gcvfun()
245         # the GCV curve
246         c1 = Curve(y=g, x=self.lams, type='line')
247         c2 = Curve(y=g, x=self.lams, type='none', marks=1, marker=
                '\5')
248         g1 = Graph2d(c1, axis_scales='loglog')
249         g1.add(c2)
250
251         if self.reg_c:
252             # the position of min
253             c3 = Curve(y=arange(min(g), max(g), (max(g)-min(g
                    ))/10), x=[self.reg_c]*10, type='dash')
254             g1.add(c3)
255         g1.plot()
256         paws()
257
258
259 class reginv:
260     def __init__(self, a, y, verbose=0):
261         self.a = a
262         self.y = y
263         self.verbose = verbose
264
265     def applyrowmask(self, mask):
266         newa = zeros((len(mask), self.a.shape[1]), self.a.typecode
                ())
267         newy = zeros(len(mask), self.y.typecode())
268         for i in range(len(mask)):
269             newa[i, :] = self.a[mask[i], :]
270             newy[i] = self.y[mask[i]]
271         self.a = newa
272         self.y = newy
273         return self
274
```

```
275     def applycolumnmask(self, mask):
276         newa = zeros((self.a.shape[0], len(mask)), self.a.typecode
                ())
277         for i in range(len(mask)):
278             newa[:, i] = self.a[:, mask[i]]
279         self.a = newa
280         return self
281
282     def applyweight(self, w):
283         """ Ax = y under weight w --> ((WA)'(WA) + \lam^2)x = W*W*y
284         where W is a diagonal matrix """
285         if w == None: return self
286         W = zeros((len(w), len(w)), 'd')
287         for i in range(len(w)):
288             W[i, i] = w[i]
289         self.a = mult(W, self.a)
290         self.y = mult(W*W, self.y)
291         return self
292
293     def applyfactor(self, f):
294         " factor f is a 1d array with size of y"
295         if f == None: return self
296         self.y = self.y/f
297         self.a = self.a/trans([f]*self.a.shape[1])
298         return self
299
300     def cond(self):
301         " return condition number of self.a "
302         lam = svd(self.a)[1]
303         return lam[0]/lam[-1]
304
305     def params(self):
306         " return reg_c and eta "
307         l = lc(self.a, self.y)
308         reg_c = l.l_corner()[0]
309         return reg_c
310
311     def inv(self, lam=None):
312         " solve ax = y by Tikhonov regularization with a factor
                vector f"
313         # note it is a = u*s*v, and they are all real
314         # gcv criterion fails for multiplitive noise
315         if not self.a.iscontiguous():
316             self.a = array(self.a, copy=1)
317         if not self.y.iscontiguous():
318             self.y = array(self.y, copy=1)
319
320         if self.verbose: print '*** Condition number ***', self.cond
                ()
321         l = lc(self.a, self.y)
322         l.use_GLOBAL = 0
323         if lam != None:
324             return l.solu(lam)
```

```
325         else:
326             [reg_c, kappa] = l.l_corner()
327             if self.verbose: l.plotlc()
328             print 'reg_c=', reg_c, 'kappa=', kappa
329             return l.solu(reg_c)
330
331
332 class reginv2(reginv):
333     def __init__(self, a1, a2, y, verbose=0):
334         " solve a1*x1 + a2*x2 = y "
335         # a1 is mxn, a2 is mxn, y is m and return x is n
336         self._n = a1.shape[1]
337         a = concat((a1, a2), 1)
338         reginv.__init__(self, a, y, verbose)
339
340     def inv(self, lam=None):
341         x = reginv.inv(self, lam)
342         return (x[:self._n], x[self._n:])
343
344
345 def shaw(n):
346     " [A, b, x]=shaw(n) setup a nth order shaw's problem "
347     if n%2 != 0: return
348     h = pi/n; A = zeros((n,n), 'd');
349
350     # Compute the matrix A.
351     co = cos(-pi/2 + arange(.5,n)*h);
352     psi = pi*sin(-pi/2 + arange(.5,n)*h);
353     for i in range(n/2):
354         for j in range(i,n-i):
355             ss = psi[i] + psi[j];
356             if ss == 0: A[i,j] = (co[i] + co[j])**2;
357             else: A[i,j] = ((co[i] + co[j])*sin(ss)/ss)**2;
358             A[n-j-1,n-i-1] = A[i,j];
359         A[i,n-i-1] = (2*co[i])**2;
360     A = A + trans(triu(A,1)); A = A*h;
361
362     # Compute the vectors x and b.
363     a1 = 2; c1 = 6; t1 = .8
364     a2 = 1; c2 = 2; t2 = -.5
365     x = a1*exp(-c1*(-pi/2 + trans(arange(.5,n))*h - t1)**2) + a2*exp
        (-c2*(-pi/2 + trans(arange(.5,n))*h - t2)**2)
366     b = mult(A,x);
367     return [A, b, x]
368
369 def test1(n):
370     [a, b, x] = shaw(2*n)
371     b = b*(1+1e-1*rand(2*n))
372     print 'Consistent for L-Curve'
373     l = lc(a, b)
374     l.use_GLOBAL = 0
375     reg_c = l.l_corner()[0]
376     x = l.solu(reg_c)
```

```
377         [rho_c, eta_c] = l.rho_eta(reg_c)
378         rho_true = norm(mult(a, x) - b)
379         print 'rho_c =', rho_c
380         print 'while the true rho is:', rho_true
381         print 'eta_c =', eta_c
382         print 'while the true eta is:', norm(x)
383
384     def test2(n):
385         [a, b, x] = shaw(2*n)
386         b = b*(1+1e-1*rand(2*n))
387         g = gcv(a, b)
388
389         print '==========GCV+GLOBAL=========='
390         reg_c = g.minGcv()
391         print 'reg_c=', reg_c
392         g.plotgcv()
393         print 'error=', norm(x-g.solu(reg_c))/norm(x)
394
395         print '==========GCV+fmin=========='
396         g.use_GLOBAL = 0
397         reg_c = g.minGcv()
398         print 'reg_c=', reg_c
399         g.plotgcv()
400         print 'error=', norm(x-g.solu(reg_c))/norm(x)
401
402         print '==========LC+GLOBAL=========='
403         l = lc(a, b)
404         reg_c = l.l_corner()[0]
405         print 'reg_c=', reg_c
406         l.plotlc()
407         print 'error=', norm(x-l.solu(reg_c))/norm(x)
408
409         print '==========LC+fmin=========='
410         l.use_GLOBAL = 0
411         reg_c = l.l_corner()[0]
412         print 'reg_c=', reg_c
413         l.plotlc()
414         print 'error=', norm(x-l.solu(reg_c))/norm(x)
415
416
417     def test3():
418         # test reginv
419         from Math import *
420         a = rand(10, 10)
421         x = array([0, 0, 0, 1, 3, 0, 0, 0, 0, 0])
422         y = mult(a, x)
423         inv = reginv(a, y, verbose=1)
424         print inv.inv()
425
426
427     def test4():
428         # test reginv2
```

```
429         from Math import *
430         a1 = rand(20, 10)
431         a2 = rand(20, 10)**2
432         x1 = array([0, 0, 0, 1, 3, 0, 0, 0, 0, 0])
433         x2 = array([0, 0, 0, 0, 1, 0, 0, 0, 0, 0])
434         y = mult(a1, x1) + mult(a2, x2)
435         inv = reginv2(a1, a2, y, verbose=1)
436         print inv.inv()
437
438
439     if __name__ == "__main__":
440         #test1(20)
441         #test2(20)
442         test3()
443         test4()
```

Appendix F

Relevant Publications

[1] M. Xu, W. Cai, M. Lax, and R. R. Alfano. Stochastic photon migration in turbid media. *TBA*, 2001. (to submit).

[2] M. Xu, W. Cai, M. Lax, and R. R. Alfano. Locating an absorptive layer using optical diffusion tomography: analytically solvable one-dimensional transmission and backscattering models. *TBA*, 2001. (to submit).

[3] M. Xu, W. Cai, M. Lax, and R. R. Alfano. Photon migration in turbid media using a cumulant approximation to radiative transfer. *Phys. Rev. E*, 2001. (under review).

[4] M. Xu, M. Lax, and R. R. Alfano. Time-resolved Fourier optical diffuse tomography. *J. Opt. Soc. Am. A*, 18(7):1535–1542, 2001.

[5] M. Xu, W. Cai, M. Lax, and R. R. Alfano. A transport model for optical tomography in turbid media. In *Signal Recovery and Synthesis*. OSA, 2001.

[6] M. Xu, W. Cai, M. Lax, and R. R. Alfano. A photon transport forward model for imaging in turbid media. *Opt. Lett.*, 26(14):1066–1068, 2001.

[7] M. Xu. LyX: another scientific word processor. *Optics & Photonics News*, 11(11):42–43, 2000.

[8] M. Xu, M. Lax, and R. R. Alfano. Time-resolved fourier diffuse optical tomography. In *Advances in Optical Imaging and Photon Migration*, volume 38 of *OSA TOPS Biomedical Topical Meetings*, pages 345–347, 2000.

[9] M. Xu, M. Lax, and R. R. Alfano. Time resolved optical diffuse tomography. In *CCAPP Annual Poster Presentation*. The City College of New York, Nov. 2000.

[10] M. Xu, S. K. Gayen, W. Cai, M. E. Zevallos, M. Lax, and R. R. Alfano. Time sliced three dimensional inverse image reconstruction of objects in highly scattering media. In *Optical tomography and spectroscopy of tissue III*, volume 3597, pages 2–4. SPIE, 1999.

[11] W. Cai, S. K. Gayen, M. Xu, M. Zevallos, M. Alrubaiee, M. Lax, and R. R. Alfano. Optical tomographic image reconstruction from ultrafast time-sliced transmission measurements. *Appl. Opt.*, 38(19):1–10, 1999.

[12] W. Cai, S. K. Gayen, M. Xu, M. Lax, and R. R. Alfano. Inverse reconstruction of three-dimensional tomographic images of objects in turbid media from time-sliced two-dimensional transmission measurements. In James G. Fujimoto and Michael S. Patterson, editors, *Advances in optical and photon migration*, volume 21 of *OSA TOPS*, pages 138–141, 1998.

Bibliography

[1] L. Wang, P. P. Ho, C. Liu, G. Zhang, and R. R. Alfano, "Ballistic 2-D imaging through scattering walls using an ultrafast optical Kerr gate," Science **253,** 769–771 (1991).

[2] R. R. Alfano *et al.*, "Time-resolved and nonlinear optical imaging for medical applications," Ann. N. Y. Acad. Sci. 838 (1998).

[3] R. R. Alfano, S. G. Demos, and S. K. Gayen, "Advances in optical imaging of biomedical media," Ann. N. Y. Acad. Sci. **820,** 248–271 (1997).

[4] A. Ishimaru, *Single scattering and transfer theory*, Vol. I of *Wave propagation and scattering in random media* (Academic, New York, 1978).

[5] in *Optical tomography, photon migration, and spectroscopy of tissue and model media: theory, human studies, and instrumentation*, Vol. 2389 of *Proc. SPIE*, B. Chance and R. R. Alfano, eds., (1995).

[6] in *Diffusing photons in turbid media*, A. G. Yodh, B. Tromberg, E. Sevick-Muraca, and D. Pine, eds., (OSA, 1997), pp. 136–342, a special issue of J. Opt. Soc. Am. A, Vol. 14.

[7] in *Proceedings of Inter-Institute Workshop on in vivo Optical Imaging at the NIH*, A. H. Gandjbakhche, ed., (Optical Soceity of America, 1999).

[8] J. C. Hebden, S. R. Arridge, and D. T. Delpy, "Optical imaging in medicine: I. experimental techniques," Phys. Med. Biol. **42,** 825–840 (1997).

[9] S. R. Arridge and J. C. Hebden, "Optical imaging in medicine: II. Modelling and reconstruction," Phys. Med. Biol. **42,** 841–853 (1997).

[10] S. B. Colak, D. G. Papaioannou, G. W. t Hooft, M. B. van der Mark, H. Schomberg, J. C. J. Paasschens, J. B. M. Melissen, and N. A. A. J. van Asten, "Tomographic image reconstruction from optical projections in light-diffusing media," Appl. Opt. **36,** 180–213 (1997).

[11] S. A. Walker, S. Fantini, and E. Gratton, "Image reconstruction by backprojection from frequency-domain optical measurements in highly scattering media," Appl. Opt. **36,** 170–174 (1997).

[12] C. L. Matson, N. Clark, L. McMackin, and J. S. Fender, "Three-dimensional localization in thick tissue with the use of diffuse photon-density waves," Appl. Opt. **36,** 214–220 (1997).

[13] X. D. Li, T. Durduran, and A. G. Yodh, "Diffraction tomography for biomedical imaging with diffuse-photon density waves," Opt. Lett. **22,** 573–575 (1997).

[14] X. Cheng and D. A. Boas, "Diffuse optical reflection tomography with continuous-wave illumination," Opt. Express **4,** 118–123 (1998).

[15] T. Durduran, J. P. Culver, M. J. Holboke, X. D. Li, and L. Zubkov, "Algorithms for 3D localization and imaging using near-field diffraction tomography with diffuse light," Opt. Express **4,** 247–262 (1999).

[16] S. Fantini, S. A. Walker, M. A. Franceschini, M. Kaschke, P. M. Schlag, and K. T. Moesta, "Assessment of the Size, Position, and Optical Properties of Breast Tumors in Vivo by Noninvasive Optical Methods," Appl. Opt. **37,** 1982–1989 (1998).

[17] D. Grosenick, H. Wabnitz, H. H. Rinneberg, K. T. Moesta, and P. M. Schlag, "Development of a Time-Domain Optical Mammograph and First in vivo Applications," Appl. Opt. **38,** 2927–2943 (1999).

[18] A. H. Gandjbakhche, V. Chernomordik, J. C. Hebden, and R. Nossal, "Time-Dependent Contrast Functions for Quantitative Imaging in Time-Resolved Transillumination Experiments," Appl. Opt. **37,** 1973–1981 (1998).

[19] V. Chernomordik, D. Hattery, A. H. Gandjbakhche, A. Pifferi, P. Taroni, A. Torricelli, G. Valentini, and R. Cubeddu, "Quantification by random walk of the optical parameters of nonlocalized abnormalities embedded within tissuelike phantoms," Opt. Lett. **25,** 951–953 (2000).

[20] S. R. Arridge, M. Schweiger, M. Hiraoka, and D. T. Delpy, "A finite-element approach for modelling photon transport in tissue," Med. Phys. **20,** 299–309 (1993).

[21] S. R. Arridge, "Photon-measurement density functions. Part I: Analytic forms," Appl. Opt. **34,** 7395–7409 (1995).

[22] H. Jiang, K. D. Paulsen, U. L. Osterberg, B. W. Pogue, and M. S. Patterson, "Optical image reconstruction using frequency-domain data: simulations and experiments," J. Opt. Soc. Am. A **13,** 253–266 (1996).

[23] B. W. Pogue, T. O. McBride, J. Prewitt, U. L. Österberg, and K. D. Paulsen, "Spatially variant regularization improves diffuse optical tomography," Appl. Opt. **38**, 2950–2961 (1999).

[24] M. S. Patterson, B. Chance, and B. C. Wilson, "Time-resolved reflectance and transmittance for the non-invasive measurement of tissue optical properties." Appl. Opt. **28**, 2331–2336 (1989).

[25] D. A. Boas, M. A. O'Leary, B. Chance, and A. G. Yodh, "Detection and characterization of optical inhomogeneties with diffuse photon density waves: a signal-to-nose analysis," Appl. Opt. **36**, 75–92 (1997).

[26] W. Cai, S. K. Gayen, M. Xu, M. Zevallos, M. Alrubaiee, M. Lax, and R. R. Alfano, "Optical tomographic image reconstruction from ultrafast time-sliced transmission measurements," Appl. Opt. **38**, 1–10 (1999).

[27] M. Xu, M. Lax, and R. R. Alfano, "Time-resolved Fourier optical diffuse tomography," J. Opt. Soc. Am. A **18**, 1535–1542 (2001).

[28] M. H. Pirenne, *The diffraction of X-rays and electrons by free molecules* (Cambridge Univ. Press, London, 1946).

[29] J. H. Hubbell and S. M. Seltzer, "Tables of X-ray Mass attenuation coefficients and mass energy-absorption coefficients from 1 keV to 20 MeV for elements Z = 1 to 92 and 48 additional substances of dosimetric interest.". `http://physics.nist.gov/PhysRefData/XrayMassCoef/cover.html`, 1996.

[30] B. Chance, Q. Luo, S. Nioka, D. C. Alsop, and J. A. Detre. "Optical investigation of physiology: a study of instrinsic and extrinsic biomedical contrast." Phil. Trans. R. Soc. Lond. **B352**, 707–716 (1997).

[31] F. F. Jöbsis, "Noninvasive, infrared monitoring of cerebral and myocardial oxygen sufficiency and circulatory parameters." Science **198**, 1264–1267 (1977).

[32] L. W. Lo, W. T. Jenkins, S. A. Vinogradov, S. M. Evans, and D. F. Wilson, "Oxygen distribution in the vasculature of mouse tissue *in vivo* measured using a near-infrared phosphor." Adv. Exp. Med. Biol. **411**, 577–583 (1997).

[33] M. Cutler, "Transillumination as an aid in the diagnosis of breast lesions: with special reference to its value in cases of bleeding nipples." Surg. Gyncol. Obstet. **48**, 721–729 (1929).

[34] C. M. Gros, Y. Quenneville, and Y. Hummel, "Diaphanologie mammaire." J. Radiol. Electrol. Med. Nucl. **53**, 297–306 (1972).

[35] E. Carlsen, "Transillumination light scanning," Diagn. Imaging **4,** 28–34 (1982).

[36] A. Alveryd, I. Andersson, K. Aspegren, G. Balldin, N. Bjurstam, G. Edstrom, G. Fagerberg, U. Glas, O. Jarlman, and S. A. L. and, "Lightscanning versus mammography for the detection of breast cancer in screening and clinical practice. A Swedish multicenter study.," Cancer **65,** 1671–7 (1990).

[37] K. M. Yoo and R. R. Alfano, "Time-resolved coherent and inhorent components of forward light scattering in random media," Opt. Lett. **15,** 320–322 (1990).

[38] K. M. Yoo, F. Liu, and R. R. Alfano, "When does the diffusion approximation fail to describe photon transport in random media," Phys. Rev. Lett. **64,** 2647–2650 (1990).

[39] A. C. Kak, "Compuerized tomography with x-ray emission and ultrasound sources," Proc. IEEE **67,** 1245–1272 (1979).

[40] A. J. Devaney, "A filtered backpropagation algorithm for diffraction tomography," Ultrsonic Imaging **4,** 336–350 (1982).

[41] X. Pan, "Unified reconstruction theory for diffraction tomography, with consideration of noise control." J. Opt. Soc. Am. A **15,** 2312–2326 (1998).

[42] C. Matson and H. Liu, "Resolved object imaging and localization with the use of a backpropagation algorithm." Opt. Exp. **6,** 168–174 (2000).

[43] S. R. Deans, *The Radon transform and some of its applications* (Wiley, New York, 1983).

[44] D. A. Boas, M. A. O. Leary, B. Chance, and A. G. Yodh, "Scattering of diffuse photon density waves by spherical inhomogeneities within turbid media: analytic solution and applications." Proc. Natl. Acad. Sci. USA **91,** 4887–4891 (1994).

[45] S. A. Walker, D. A. Boas, and E. Gratton, "Photon Density Waves Scattered from Cylindrical Inhomogeneities: Theory and Experiments." Appl. Opt. **37,** 1935–1944 (1998).

[46] M. Schweiger and S. R. Arridge, "Comparison of Two- and Three-Dimensional Reconstruction Methods in Optical Tomography." Appl. Opt. **37,** 7419–7428 (1998).

[47] J. B. Keller, "Accuracy and validity of the Born and Rytov approximation." J. Opt. Soc. Am. **59,** 1003–4 (1969).

[48] S. K. Gayen, M. E. Zevallos, M. Alrubaiee, J. M. Evans, and R. R. Alfano, "Two-dimensional near-infrared transillumination imaging of biomedical media with a chromium forsterite laser," Appl. Opt. **37,** 5327–5336 (1998).

[49] W. Cai, M. Lax, and R. R. Alfano, "Cumulant solution of the elastic Boltzmann transport equation in an infinite uniform medium," Phys. Rev. E **61,** 3871–3876 (2000).

[50] M. Xu, W. Cai, M. Lax, and R. R. Alfano, "A photon transport forward model for imaging in turbid media," Opt. Lett. **26,** 1066–1068 (2001).

[51] W. Cai, M. Lax, and R. R. Alfano, "Analytical solution of the elastic Boltzmann transport equation in an infinite uniform medium using cumulant expansion," J. Phys. Chem. B **104,** 3996–4000 (2000).

[52] A. N. Tikhonov, "On the solution of incorrectly stated problems and a method of regularization," Dokl. Akad. Nauk SSSR **151,** 501–504 (1963).

[53] P. C. Hansen and D. P. O'Leary, "The use of the L-curve in the regularization of discrete ill-posed problems," SIAM J. Sci. Comput. **14,** 1487–1053 (1993).

[54] C. F. Bohren and D. R. Huffman, *Absorption and scattering of light by small particles* (John Wiley & Sons, 1983).

[55] H. C. van de Hulst, *Light scattering by small particles* (Dover Publications, Inc., 1981).

[56] G. Mie, "Beitrage zur optik trüber medien speziell kolloidaler metallösungen," Ann. Phys. pp. 377–445 (1908).

[57] Y. Yamada, "Diffusion coefficient in the photon diffusion equation," In *Optical tomography, photon migration, and spectroscopy of tissue and model media: theory, human studies, and instrumentation,* B. Chance and R. R. Alfano, eds., Proc. SPIE 2389 (1995). See Ref. [5].

[58] K. Furutsu, "Diffusion equation derived from space-time transport equation," J. Opt. Soc. Am. **70,** 360–366 (1980).

[59] K. Furutsu and Y. Yamada, "Diffusion approximation for a dissipative random medium and the application," Phys. Rev. E **50,** 3634–3640 (1994).

[60] C. Cercignani, *The Boltzmann equation and its applications,* Vol. 67 of *Applied Mathematical Sciences* (Springer-Verlag, 1988).

[61] G. D. Mahan, "Diffusion through a slab," J. Math. Phys. **36,** 6758–6773 (1995).

[62] A. Y. Polishchuk and R. R. Alfano, "Photon diffusion on the velocity sphere," Opt. Lett. **21**, 916–918 (1996).

[63] A. Y. Polishchuk, M. Zevallos, F. Liu, and R. R. Alfano, "Generalization of Fermat's principle for photon diffusion on the velocity sphere," Phys. Rev. E **53**, 5523–5526 (1996).

[64] A. Y. Polishchuk and R. R. Alfano, "Fermat photons in turbid media: an exact analytic solution for most favorable paths–a step toward optical tomography," Opt. Lett. **20**, 1937–1939 (1995).

[65] D. J. Durian, "The diffusion coefficient depends on absorption," Opt. Lett. **23**, 1502–1504 (1998).

[66] R. Aronson and N. Corngold, "Photon diffusion coefficient in an absorbing medium," J. Opt. Soc. Am. A **16**, 1066–1071 (1999).

[67] M. Gershenson, "Time-dependent equation for the intensity in the diffusion limit using a higher-order angular expansion," Phys. Rev. E **59**, 7178–7184 (1999).

[68] L. G. Henyey and J. L. Greenstein, "Diffuse radiation in the galaxy," Astrophys. J. **93**, 70–83 (1941).

[69] P. K. MacKeown, *Stochastic simulation in Physics* (Springer, 1997).

[70] M. Born and E. Wolf, *Principles of optics: electromagnetic theory of propagation, interference and diffraction of light* (Pergamon Press, 1986).

[71] P. D. Coddington, "Random number generators for parallel computers," NHSE Review 1996 (1996), version 1.1 (2 May, 1997). See also `http://www.crpc.rice.edu/NHSEreview/RNG`.

[72] S. Chandrasekhar, *Radiation transfer* (Oxford, 1950).

[73] J. J. Duderstadt and W. R. Martin, *Transport theory* (Wiley, 1979).

[74] A. Ishimaru, *Wave propagation and scattering in random media* (Academic, New York, 1978).

[75] S. H. Ma, *Statistical Mechanics* (World Scientific, Philadelphia, 1985).

[76] M. G. Kendall, *Kendall's advanced theory of statistics* (Oxford University Press, 1999).

[77] S. Chandrasekhar, "Stochastic problems in physics and astronomy," Re. Mod. Phys. **15,** 1–89 (1943).

[78] J. X. Zhu, D. J. Pine, and D. A. Weitz, "Internal reflection of diffusive light in random media," Phys. Rev. A **44,** 3948–3959 (1991).

[79] G. Popescu, C. Mujat, and A. Dogariu, "Evidence of scattering anisotropy effects on boundary conditions of the diffuse equation," Phys. Rev. E **61,** 4523–4529 (2000).

[80] R. C. Haskell, L. O. Svaasand, T.-T. Tsay, T.-C. Feng, M. S. McAdams, and B. J. Tromber, "Boundary conditions for the diffusion equation in radiative transfer," J. Opt. Soc. Am. A **11,** 2727–2741 (1994).

[81] J. C. J. Paasschens and G. W. t. Hooft, "Influence of boundaries on the imaging of objects in turbid media," J. Opt. Soc. Am. A **15,** 1797–1812 (1998).

[82] S. A. Prahl, M. Keijzer, S. L. Jacques, and A. J. Welch, "A Monte Carlo model of loght propagation in tissue," In *Dosimetry of laser radiation in medicine and biology,* SPIE Institute Series **IS-5,** 102–111 (1989).

[83] L. H. Wang, S. L. Jacques, and L. Q. Zheng, "MCML - Monte Carlo modeling of photon transport in multi-layered tissues," Computer Methods and Programs in Biomedicine **47,** 131–146 (1995), `http://omlc.ogi.edu/software/mc/index.html`.

[84] R. Y. Rubinstein, *Simulation and the Monte Carlo method* (John Wiley & Sons, 1981).

[85] J. Berntsen, T. O. Espelid, and A. Genz, "Algorithm 698: DCUHRE: An Adaptive Multidimensional Integration Routine for a Vector of Integrals," ACM Transactions on Mathematical Software **17,** 452–456 (1991).

[86] in *Photon migration and imaging in random media and tissues,* Vol. 1888 of *Proc. SPIE,* B. Chance and R. R. Alfano, eds., (1993).

[87] Y. Tsuchiya, K. Ohta, and T. Urakami, "Isotropic photon injection for noninvasive tissue spectroscopy," Jpn. J. Appl. Phys. **34, Part 1,** 2495–2501 (1995).

[88] C. W. Groetsch, *The theory of Tikhonov regularization for Fredholm equations of the first kind* (Pitman, London, 1984).

[89] V. A. Morozov, *Methods for solving incorrectly posed problems* (Springer-Verlag, New York, 1984).

[90] M. Hanke and P. C. Hansen, "Regularization methods for large-scale problems." Surveys Math. Indust. 3 (1993).

[91] A. Neumaier, "Solving Ill-Conditioned and Singular Linear Systems: A Tutorial on Regularization," SIAM Review **40,** 636–666 (1998).

[92] L. Tenorio, "Statistical regularization of inverse problem." SIAM Review **43,** 347–366 (2001), introduction level.

[93] P. C. Hansen, "The discrete Picard condition for discrete ill-posed problems." BIT **30,** 658–672 (1990).

[94] P. C. Hansen, "Analysis of discrete ill-posed problems by means of the L-curve." SIAM Rev. **34,** 561–580 (1992).

[95] G. H. Golub and M. Heath, "Generalized cross-validation as a method for choosing a good ridge parameter," Technometrics **21,** 215–223 (1979).

[96] S. R. Arridge and M. Schweiger, "Photon-measurement density functions. Part 2: Finite-element-method calculations." Appl. Opt. **34,** 8026- (1995).

[97] R. Cubeddu, A. Pifferi, P. Taroni, A. Torricelli, and G. Valentini, "Noninvasive absorption and scattering spectroscopy of bulk diffusive media: An application to the optical characterization of human breast." Appl. Phys. Lett. **74,** 874–876 (1999).

[98] I. S. Gradshteyn and I. M. Ryzhik. *Table of integrals, series, and products* (Academic Press, New York, 1980).

[99] W. Cai, S. K. Gayen, M. Xu, M. Lax, and R. R. Alfano, "Inverse reconstruction of three-dimensional tomographic images of objects in turbid media from time-sliced two-dimensional transmission measurements." In *Advances in optical and photon migration,* J. G. Fujimoto and M. S. Patterson, eds., OSA TOPS **21,** 138–141 (1998).

[100] H. J. van Staveren, C. J. M. Moes, J. van Marle, S. A. Prahl, and M. J. C. van GemertJ, "Light scattering in intralipid-10% in the wavelength range of 400-1100nm." App. Opt. **30,** 4507–4514 (1991).

[101] W. Cai, B. B. Das, F. Liu, M. Zevallos, M. Lax, and R. R. Alfano, "Time-resolved optical diffusion tomographic image reconstruction in highly scattering turbid media," Proc. Natl. Acad. Sci. USA **93,** 13561–13564 (1996).